

AD-A221 292

THIS IS A COPY

AFOSR-TR-90-0383

2

A Final Report
Contract No. AFOSR-87-0082-A

January 1, 1987 - December 31, 1989

PROCESSING AND PROPERTIES OF
ADVANCED ALUMINUM ALLOYS

Submitted to:

Air Force Office of Scientific Research/NE
Building 410
Bolling Air Force Base
Washington, DC 20332-6448

Attention: Dr. Alan H. Rosenstein

Submitted by:

J. A. Wert
Associate Professor

E. A. Starke, Jr.
Earnest Oglesby Professor of
Materials Science and Dean

Report No. UVA/525672/MS90/101
March 1990

DEPARTMENT OF MATERIALS SCIENCE

SCHOOL OF
ENGINEERING 
& APPLIED SCIENCE

University of Virginia
Thornton Hall
Charlottesville, VA 22903

DTIC
ELECTE
MAY 03 1990
S B D

DISTRIBUTION STATEMENT A

Approved for public release
Distribution Unlimited

90 05 03 180

UNIVERSITY OF VIRGINIA
School of Engineering and Applied Science

The University of Virginia's School of Engineering and Applied Science has an undergraduate enrollment of approximately 1,500 students with a graduate enrollment of approximately 600. There are 160 faculty members, a majority of whom conduct research in addition to teaching.

Research is a vital part of the educational program and interests parallel academic specialties. These range from the classical engineering disciplines of Chemical, Civil, Electrical, and Mechanical and Aerospace to newer, more specialized fields of Applied Mechanics, Biomedical Engineering, Systems Engineering, Materials Science, Nuclear Engineering and Engineering Physics, Applied Mathematics and Computer Science. Within these disciplines there are well equipped laboratories for conducting highly specialized research. All departments offer the doctorate; Biomedical and Materials Science grant only graduate degrees. In addition, courses in the humanities are offered within the School.

The University of Virginia (which includes approximately 2,000 faculty and a total of full-time student enrollment of about 17,000), also offers professional degrees under the schools of Architecture, Law, Medicine, Nursing, Commerce, Business Administration, and Education. In addition, the College of Arts and Sciences houses departments of Mathematics, Physics, Chemistry and others relevant to the engineering research program. The School of Engineering and Applied Science is an integral part of this University community which provides opportunities for interdisciplinary work in pursuit of the basic goals of education, research, and public service.

A Final Report
Contract No. AFOSR-87-0082-A

January 1, 1987 - December 31, 1989

PROCESSING AND PROPERTIES OF
ADVANCED ALUMINUM ALLOYS

Submitted to:

Air Force Office of Scientific Research/NE
Building 410
Bolling Air Force Base
Washington, DC 20332-6448

Attention: Dr. Alan H. Rosenstein

Submitted by:

J. A. Wert
Associate Professor

E. A. Starke, Jr.
Earnest Oglesby Professor of
Materials Science and Dean

Department of Materials Science
SCHOOL OF ENGINEERING AND APPLIED SCIENCE
UNIVERSITY OF VIRGINIA
CHARLOTTESVILLE, VIRGINIA

**BEST
AVAILABLE COPY**

Report No. UVA/525672/MS90/101
March 1990

Copy No. 3

REPORT DOCUMENTATION PAGE			Form Approved OMB No. 0704-0188	
<small>Public reporting burden for this collection of information is estimated to average 1 hour per response, including the time for reviewing instructions, searching existing data sources, gathering and maintaining the data needed, and completing and reviewing the collection of information. Send comments regarding this burden estimate or any other aspect of this collection of information, including suggestions for reducing this burden, to Washington Headquarters Services, Directorate for Information Operations and Reports, 1215 Jefferson Davis Highway, Suite 1204, Arlington, VA 22202-4302, and to the Office of Management and Budget, Paperwork Reduction Project (0704-0188), Washington, DC 20503.</small>				
1. AGENCY USE ONLY (Leave blank)		2. REPORT DATE March 1990		3. REPORT TYPE AND DATES COVERED Final Report/1-1-87 - 12-31-89
4. TITLE AND SUBTITLE Processing and Properties of Advanced Aluminum Alloys			5. FUNDING NUMBERS AFOSR-87-0082-A	
6. AUTHOR(S) J. A. Wert, Associate Professor E. A. Starke, Earnest Oglesby Professor and Dean			AFOSR-TR. 90-0383	
7. PERFORMING ORGANIZATION NAME(S) AND ADDRESS(ES) Dept. of Materials Science, School of Engineering and Applied Science, University of Virginia, Thornton Hall, Charlottesville, VA 22903-2442			8. PERFORMING ORGANIZATION REPORT NUMBER UVA/525672/MS90/101	
9. SPONSORING/MONITORING AGENCY NAME(S) AND ADDRESS(ES) Air Force Office of Scientific Research /Rosenstein Building 410 Bolling Air Force Base Washington, DC 20332			10. SPONSORING/MONITORING AGENCY REPORT NUMBER 2806/A2	
11. SUPPLEMENTARY NOTES				
12a. DISTRIBUTION/AVAILABILITY STATEMENT Unlimited Distribution			12b. DISTRIBUTION CODE	
13. ABSTRACT (Maximum 200 words) <p>This research has been concerned with the use of processing to optimize the microstructure of advanced aluminum alloys for property improvement. The report was concerned with microstructure control and fracture. The focus was on the effect of shearable and non-shearable precipitates on slip behavior, void nucleation and fracture; the effect of composition on quench sensitivity and fracture; the effect of nonequilibrium eutectic melting during solution heat treatment on intergranular fracture; and the effect of slip behavior on fatigue crack propagation. Task II is covered in Part II of this report and was concerned with processing of advanced aluminum alloys for microstructure control for improvement of superplastic forming properties. The detailed studies of this task have allowed identification of the material and processing parameters that control development of the microstructural features required for superplasticity.</p>				
14. SUBJECT TERMS			15. NUMBER OF PAGES 144	
			16. PRICE CODE	
17. SECURITY CLASSIFICATION OF REPORT Unclassified	18. SECURITY CLASSIFICATION OF THIS PAGE Unclassified	19. SECURITY CLASSIFICATION OF ABSTRACT Unclassified	20. LIMITATION OF ABSTRACT Unlimited	

TABLE OF CONTENTS

PART I.	Microstructure Control and Fracture of Advanced Aluminum Alloys	
A.	Objective	1
B.	Accomplishments	
1.	The Effect of Particle Size on the Slip Behavior of Particle Reinforced Alloys. J.M. Duva, M.A. Daeubler, E.A. Starke, Jr., and G. Luetjering	1
2.	The Influence of Mn Dispersoid Content and Stress State on Ductile Fracture of 2134-Type Aluminum Alloys. J.A. Walsh, K.V. Jata and E.A. Starke, Jr.	2
3.	Quench Sensitivity of the Al-Li-Cu-Mg Alloy 8090. G.N. Colvin and E.A. Starke, Jr.	4
4.	Intergranular Fracture of an Al-Li-Cu-Mg Alloy as a Result of Nonequilibrium Eutectic Melting During Solution Treatment. P. Bourgasser, J.A. Wert, and E.A. Starke, Jr.	5
5.	The Fatigue Crack Growth Behavior of the Al-Cu-Li Alloy Weldalite 049. C.P. Blankenship, Jr., and E.A. Starke, Jr.	6
PART II.	Processing of Advanced Aluminum Alloys for Microstructure Control	
A.	Objective	8
B.	Accomplishments	8
C.	Significance	12
APPENDIX	14

QUALITY INSPECTED 1	By _____	
	Distribution/ _____	
	Availability Codes _____	
	Dist	Avail and/or Special
<div style="font-size: 2em; font-weight: bold; margin-left: 10px;">A-1</div>		

Part I. MICROSTRUCTURE CONTROL AND FRACTURE OF ADVANCED ALUMINUM ALLOYS.

A. Objective

This project is concerned with the control of microstructure for improving fracture resistance of advanced aluminum alloys. Part I was concerned with the effect of shearable and non-shearable precipitates on slip behavior, void nucleation and fracture; the effect of composition on quench sensitivity and fracture; the effect of nonequilibrium eutectic melting during solution heat treatment on intergranular fracture; and the effect of slip behavior on fatigue crack propagation.

B. Accomplishments

1. **The Effect of Particle Size on the Slip Behavior of Particle Reinforced Alloys. J.M. Duva, M.A. Daeubler, E.A. Starke, Jr., and G. Luetjering**

Age hardenable aluminum alloys may undergo relatively brittle intergranular fracture at strains from 2 to 10 times smaller than the strain to fracture for pure aluminum. This phenomenon can be explained in broad terms as follows: Within a grain, an advancing dislocation either bypasses the coherent particles it encounters or cuts through them; cutting reduces the effective size of the obstacle, while bypassing the obstacle effectively enlarges it. If the obstacles are cut, the weakened

plane will continue to slip and deformation will be localized. As a result, dislocations pile up at the grain boundaries at isolated points; the large associated tension across the grain boundaries open intergranular cracks which propagate without absorbing much energy. We have developed a microscopic model of slip in particle reinforced alloys that predicts coarser slip for larger particles for a fixed particle volume fraction and grain size. Simple kinematic arguments also have been proposed that yield estimates of the slip band spacing in such alloys and their dependence on particle size, particle volume fraction and grain size. Our model is consistent with the experimental results obtained earlier by Jata and Starke. This model predicts decreasing strains to fracture with increasing particle size which correlates very well with experimental measurements. The results of this aspect of our research have been published in Acta Metallurgica, Volume 36, 1988, pp. 585-589, a copy of which is attached in the Appendix.

2. The Influence of Mn Dispersoid Content and Stress State on Ductile Fracture of 2134-Type Aluminum Alloys. J.A. Walsh, K.V. Jata and E.A. Starke, Jr.

Elements such as Cr, Mn and Zr are added to aluminum alloys to form dispersoids during the ingot preheat which subsequently control the grain structure and degree of recrystallization during primary processing. The dispersoids formed with Cr and Mn are incoherent with the matrix and are looped and bypassed by

dislocations during deformation. However, the Zr-rich dispersoids, which are very effective in inhibiting recrystallization, are coherent and are usually sheared by dislocations. Consequently, Zr-rich dispersoids do not aid in dispersing slip. Incoherent Mn-rich dispersoids may disperse slip but also may be the sites for microvoid nucleation and therefore may have an adverse effect on ductility and fracture toughness. Ductile fracture studies were conducted on four high purity Al-Cu-Mg-Zr (2134 type) alloys containing 0, 0.31, 0.61 and 1.02 wt.% Mn in the under and overaged conditions having similar yield strengths. The second phase particle content, i.e. Mg-rich dispersoids and Mn-containing large particles, increased with increasing Mn content. In both aging conditions maximum ductility and toughness were observed for the 0.31% Mn alloys and minimum values were observed for the 1.02% Mg alloy. The largest void content or damage accumulation due to void nucleation and growth at any strain level occurred in the 1.02% Mg alloy, consistent with ductility values. The 0.31 Mn alloys showed the highest ductility in both aging conditions. Although the void volume fractions for the 0.31% Mn alloy were similar to those of the 1.02% Mn alloy, accumulation occurred at higher strains. The void nucleation and growth data and microstructural analysis suggest that the 0.31% Mn additions provide sufficient submicrometer Mn-dispersoids to homogenize slip without producing large Mn-rich primary particles which decrease ductility. The results of this aspect of our research

have been published in Acta Metallurgica, Volume 37, 1989, pp. 2861-2871, a copy of which is attached in the Appendix.

3. Quench Sensitivity of the Al-Li-Cu-Mg Alloy 8090. G.N. Colvin and E.A. Starke, Jr.

The primary purpose of quenching age-hardened aluminum alloys is to maintain a large degree of supersaturation of solute atoms homogeneously distributed in solid solution. This permits precipitation of an optimum concentration and distribution of hardening particles during the aging treatment. As quench rates decrease, more time is allowed for solute atoms to migrate to grain boundaries or precipitate as matrix phases. Grain boundaries act as heterogeneous nucleation sites by reducing the free energy barrier to nucleation. When thermodynamic and kinetic demands are satisfied, precipitation can occur along the grain boundary and subsequently enhance intergranular cracking, grain boundary decohesion and premature material failure. Since Al-Li-X alloys have an above normal incidence of intergranular fracture, we studied the quench sensitivity of this class of materials. Time-temperature-transformation diagrams were developed for precipitation of the equilibrium T_2 (Al_6CuLi_3) and S (Al_2CuMg) phases in two compositional variations of the Al-Li-Cu-Mg alloy 8090. The start of T_2 nucleation proved to be relatively rapid in both alloy variants with T_2 nucleating in under five seconds at 400-450C in the more heavily alloyed material. Nucleation of the T_2 phase was not evident in the lean

alloy until after 20 seconds at these temperatures. The S phase nucleation appeared to be less sensitive to the composition range studied, with its earliest appearance being after ten seconds at 300C. The volume fraction of T_2 correlated well with Charpy energy absorption values, with increasing amounts of T_2 leading to decreasing toughness. 8090, like many other Al-Li-X alloys, is quench sensitive, requiring fairly rapid cooling rates from the solutionizing temperature for mechanical property optimization. The results of this aspect of our program have been published in SAMPE Quarterly, Volume 19, No. 4, 1988, pp. 10-21, a copy of which is attached in the Appendix.

4. Intergranular Fracture of an Al-Li-Cu-Mg Alloy as a Result of Nonequilibrium Eutectic Melting During Solution Treatment. P. Bourgasser, J.A. Wert and E.A. Starke, Jr.

As mentioned previously, intergranular fracture occurs in Al-Li-X alloys to a greater extent than in other precipitation-hardened aluminum alloys. This research examined the role of nonequilibrium eutectic melting on the intergranular fracture process of Al-Li-Cu-Mg and Al-Li-Cu alloys. When solution treatment of the Al-Li-Cu-Mg alloy is begun by rapid heating to temperatures of 545C or above, nonequilibrium eutectic melting of a grain boundary precipitate phase occurs and the liquid spreads along grain boundaries as a thin film. Upon quenching, intergranular cracks are found at grain boundaries where a liquid film penetrated during solution treatment. For slower heating

rates, nonequilibrium eutectic melting does not occur and no intergranular cracks are observed after quenching. No evidence of nonequilibrium eutectic melting was found in the Al-Li-Cu alloy, irrespective of heating rate to 550C. During tensile testing of as-quenched and quenched-and-aged specimens of the two alloys, intergranular fracture occurred in most cases, irrespective of whether nonequilibrium eutectic melting had taken place during solution treatment, indicating that at least one additional mechanism of intergranular fracture is invoked by deformation. The results of this aspect of our program are covered in a paper accepted for publication by Materials Science and Technology. A preprint of the paper is included in the Appendix.

5. The Fatigue Crack Growth Behavior of the Al-Cu-Li Alloy Weldalite 049. C.P. Blankenship, Jr. and E.A. Starke, Jr.

A high strength, weldable Al-Cu-Li alloy, Weldalite 049, has recently been developed for use in aerospace launch vehicles and cryogenic tankage. Economic considerations suggest that future launch vehicles must be reusable, and this requires that materials used for structural components have adequate damage tolerance. Our earlier studies on Al-Li-X alloys have shown that they have very excellent fatigue properties when they deform by planar slip. Since the deformation behavior of Weldalite 049 had not been determined, we examined the microstructure, deformation

behavior, and crack growth relationships of this new alloy. TEM of deformed samples revealed that the T3 temper deformed via highly localized planar slip due to the presence of small, coherent precipitates (GP zones and δ'), while the T8 temper deformed homogeneously with T_1 as the strengthening phase. Both constant K_{max} and constant R (0.1) fatigue curves were generated for the T3 and T8 tempers in both the T-L and L-T orientations. The T3 temper exhibited high closure levels and an apparent intrinsic threshold of 2 MPa $m^{1/2}$. The T8 temper did not exhibit high closure levels, and the intrinsic threshold was determined to be 1.3 MPa $m^{1/2}$. Weldalite-T3 has a strength comparable to 2024-T3 but has a higher resistance to fatigue crack growth, whereas Weldalite-T8 has a much higher strength and a comparable fatigue crack growth resistance to 2024-T8. A paper resulting from this aspect of our program has been submitted for publication to the Journal of Fatigue & Fracture of Engineering Materials & Structures. A copy of the manuscript is included in the Appendix.

Part II. PROCESSING OF ADVANCED ALUMINUM ALLOYS FOR MICROSTRUCTURE CONTROL.

SUMMARY

A. Objective

The broad objective of this research project has been to discover methods for processing advanced aluminum alloys to improve their superplastic forming properties. This has required detailed study of the effects of thermomechanical processing and superplastic deformation on subgrain and grain boundary characteristics. These detailed studies have allowed identification of the material and processing parameters that control development of the microstructural features required for superplasticity.

B. Accomplishments

Measurement of individual microstructural characteristics on a local scale, rather than average or global characteristics on a macroscopic scale, can provide new insight into processes which have previously been poorly understood. The initial accomplishments of this research project were associated with development of the experimental techniques required to analyze the characteristics of individual subgrain and grain boundaries. The new techniques were then applied to the problem of understanding evolution of boundaries in an Al-Zr-Si alloy as a function of deformation processing conditions and superplastic

forming conditions. The accomplishments are presented in summary form in the paragraphs and detailed descriptions of a paper submitted to Acta Metallurgica. A copy of the manuscript is included in the Appendix (item F).

Analysis Technique:

To understand the effect of processing and superplastic deformation on subgrain and grain boundaries, it is first necessary to identify the boundary characteristics. If the lattice orientations of the two crystals that meet at a boundary are known, then the misorientation associated with the boundary can be determined. The transmission electron microscopy techniques needed to find the lattice orientation of regions smaller than 1 μm in diameter have been known for 30 years, but application of these methods to gain insight into the boundary characteristics of materials have been limited because of the tedious nature of the analyses. Within the scope of the present research project, computer programs have been written to perform the grain orientation analyses. The electron diffraction information is entered into the computer using semiautomatic digitizing equipment. The crystal lattice orientation of each grain or subgrain is then calculated automatically from the diffraction information. Knowledge of the crystal orientations allows the boundary misorientations to be determined. The boundary misorientation information can then be represented in various ways, either directly on photographs of the

microstructure or indirectly using statistical distribution plots. Computerization of this analysis procedure has allowed us to collect boundary misorientation data for many different processing conditions.

Knowledge of the lattice orientation within each grain can also be used directly in the form of pole figures or crystal orientation distribution plots. These local pole figures can then be compared with bulk pole figures determined using x-ray analyses to gain an understanding of the orientation relationships between grains on a local scale. The analyses described in the attached paper show how the local crystal orientation data provide information about boundary migration that cannot be obtained from bulk measurements like x-ray texture analysis.

Results:

The methods described above have been used to analyze microstructural evolution in an Al-Zr-Si alloy, which was selected as a model material for studying microstructural evolution in superplastic aluminum alloys. The objective of the study was to answer long-standing questions about the mechanisms which allow commercial alloys to develop superplastic properties by continuous, recovery-type processes. The results of this investigation may be summarized as follows.

1. Heavy cold rolling of the Al-Zr-Si alloy containing Al₃Zr

dispersoid particles produces a microstructure that consists of layers that lie parallel to the rolling plane. Within each layer, all of the boundaries have low misorientation angles. Adjacent layers are separated by high misorientation angle boundaries. The layer thickness ranges from 2 to more than 10 μm in the cold-rolled Al-Zr-Si alloy.

2. Annealing of the cold-rolled Al-Zr-Si alloy causes low-angle (subgrain) boundaries to migrate, leading to growth of the subgrains. However, the high-angle boundaries are relatively immobile during annealing. Thus, the layered character of the cold-rolled microstructure is preserved during annealing.

3. Concurrently straining and annealing, as occurs during the superplastic forming operation, causes a rapid increase in the subgrain size and also causes the misorientation of the low-angle boundaries to increase, ultimately converting them into high-angle boundaries. By comparing annealed and concurrently strained and annealed materials, it has been shown that the change of boundary character is associated with rotation of the crystal lattice of the subgrains during superplastic deformation. The conversion of low-angle boundaries into high-angle boundaries during the initial part of the superplastic forming operation is critical because commercial alloys would not be superplastic without this conversion.

4. Development of high boundary misorientation angles by simple migration of the low-angle boundaries has been previously proposed. This mechanism is inconsistent with the microstructural observations made in present study.

5. The presence of high-angle boundaries which separate the cold-rolled microstructure into layers is significant. Previous studies of microstructural evolution during superplastic forming have used specimen orientations which did not allow observation of these boundaries. It is thought that the preexisting high angle boundaries play a critical role in subgrain rotation, which is the primary mechanism that allows a microstructure suitable for superplastic forming to develop.

C. Significance

By gaining a better understanding of how subgrain boundaries introduced by deformation processing evolve into grain boundaries during the initial part of the superplastic forming operation, it is possible to tailor the deformation processing conditions to improve superplastic forming characteristics. This understanding will be useful for developing new processing methods for imparting superplastic characteristics to advanced alloys which are difficult to form by conventional methods. The basic understanding developed within the scope of the present project is now being applied to processing of advanced materials on a DARPA-sponsored research program at the University of Virginia.

In addition, the analysis methods for identifying boundary characteristics on a local microstructural scale that have been developed within the scope of the present research project have already been applied to several other alloys. Boundary characteristics have been determined for extruded, mechanically-alloyed Al-Ti alloys being investigated for potential elevated temperature applications on an AFWAL-sponsored research program. These results have aided interpretation of the elevated-temperature properties of the mechanically-alloyed materials. The techniques have also been applied to extruded Al-Li-Mg alloys in a effort to understand microstructural evolution during processing. It is anticipated that the newly-developed techniques will continue to be applied to a broad variety of research materials to improve our understanding of processing effects on microstructure.

APPENDIX

Papers in Refereed Journals

	Page No.
A. "Large Shearable Particles Lead to Coarse Slip in Particle Reinforced Alloys," J.M. Duva, M.A. Daeubler, E.A. Starke, Jr., and G. Luetjering, <u>Acta Met.</u> 36, 1988, pp. 585-589.	15
B. "The Influence of Mn Dispersoid Content and Stress State on Ductile Fracture of 2134 Type Al Alloys," J.A. Walsh, K.V. Jata, and E.A. Starke, Jr., <u>Acta Met.</u> 37, 1989, pp. 2861-2871.	20
C. "Quench Sensitivity of the Al-Li-Cu-Mg Alloy 8090," G.N. Colvin and E.A. Starke, Jr., <u>SAMPE Quarterly</u> 19, 1988, pp. 10-21.	31
D. "Intergranular Fracture of an Al-Li-Cu-Mg Alloy as a Result of Nonequilibrium Eutectic Melting During Solution Treatment," P. Bourgasser, J.A. Wert and E.A. Starke, Jr., <u>Materials Science and Technology</u> , in press.	44
E. "The Fatigue Crack Growth Behavior of the Al-Cu-Li Alloy Werdalite 049," C.P. Blankenship, Jr., and E.A. Starke, Jr., submitted to <u>Journal of Fatigue and Fracture of Engineering Materials and Structures</u> .	78
F. "Mechanisms of Continuous Recrystallization in an Al-Zr-Si Alloy," Halldor Gudmundsson, Douglas Brooks, and John A. Wert, submitted to <u>Acta Met.</u>	104

LARGE SHEARABLE PARTICLES LEAD TO COARSE SLIP IN PARTICLE REINFORCED ALLOYS

J. M. DUVA,¹ M. A. DAEUBLER,² E. A. STARKE Jr³ and G. LUETJERING²

¹Department of Applied Mathematics, University of Virginia, Charlottesville, VA 22901, U.S.A.,

²Technische Universität Hamburg-Harburg, Hamburg, F.R.G. and

³Department of Materials Science, University of Virginia, Charlottesville, VA 22901, U.S.A.

(Received 9 February 1987; in revised form 18 May 1987)

Abstract—A microscopic model of slip in particle reinforced alloys is proposed that predicts coarser slip for larger particles for a fixed volume fraction. Coarse slip leads to intergranular fracture in such alloys.

Résumé—Nous proposons un modèle microscopique du glissement dans les alliages renforcés par des particules, modèle qui prédit un glissement plus grossier pour les particules les plus grosses, pour une fraction volumique donnée. Dans de tels alliages, ce glissement grossier conduit à une rupture intergranulaire.

Zusammenfassung—Es wird ein mikroskopisches Modell für die Gleitung in Teilchen-verstärkten Legierungen vorgeschlagen, welches gröbere Gleitung bei größeren Teilchen, für einen festen Volumanteil, voraussagt. Grobe Gleitung führt in solchen Legierungen zu intergranularem Bruch.

1. INTRODUCTION

Many alloys derive their strength in part from the homogeneous distribution of coherent second-phase particles throughout. Accurate predictions of the yield strengths of precipitate hardened alloys are based on the well understood interaction of a dislocation with a particle at the microscopic level. However, precipitate hardened alloys also exhibit low ductility and low fracture toughness; features that also must depend on the presence of the second-phase particles. This problem is less well understood.

Age hardenable Al alloys in particular may undergo relatively brittle intergranular fracture at strains from 2 to 10 times smaller than the strain to fracture for pure Al. This phenomenon can be explained in broad terms as follows. Within a grain, an advancing dislocation either bypasses the coherent particles it encounters or cuts through them; cutting reduces the effective size of the obstacle, while bypassing the obstacle effectively enlarges it. If the obstacles are cut, the weakened plane will continue to slip and deformation will be localized. As a result, dislocations pile up at the grain boundaries at isolated points; the large associated tensions across the grain boundaries open intergranular cracks that propagate without absorbing much energy. Slip becomes more localized as the size of the included particles increases and as the grain size increases. To highlight this idea we briefly review alternative treatments of slip localization in particle hardened alloys.

The resistance stress or strength due to particles in reinforced alloys is given in general by an expression of the form

$$\tau_p = C_p \rho^{1/2} r_p^{\beta} \quad (1)$$

where ρ is the particle volume fraction, r_p is the radius of the particles (assumed to be spherical, equal in size and small enough to be cut instead of bypassed) and C_p , α and β are constants that depend on the type of strengthening under consideration and the particular model of the strengthening mechanism used. Sanders and Starke [1] argue that order hardening is the dominant strengthening mechanism in Al-Li alloys, thus we henceforth restrict our attention to order hardening. Martin [2] estimates the resistance stress due to the particles in this case to be

$$\tau_p = C_p \rho^{1/2} r_p^{1/2}. \quad (2)$$

Here C_p is a function of the energy associated with the creation of an antiphase boundary as the particles are cut, the magnitude of the Burgers vector b associated with the dislocation and the dislocation line tension. Martin models the softening due to the cutting of the particles by using an effective particle radius $r_{\text{eff}} = r_p - nb/2$ in the above equation, where n is the number of dislocations that have passed on a given plane. A more precise characterization of the effective size of a cut particle can be used, but the simple expression given above is suitable for the models described herein. When $n = 2r_p/b$ the particle is effectively destroyed. To connect this model of slip softening to localization, Martin reasons that an indicator of the tendency toward coarse slip is the degradation rate of the strength with slip

$$-\frac{\partial \tau_p}{\partial n} = \frac{C_p b \rho^{1/2}}{2(r_p - nb/2)^{1/2}}. \quad (3)$$

This indicator predicts increasingly coarse slip as r_p decreases, a conclusion that is untenable in the limit of vanishingly small particles and that is contradicted

by the experimental evidence of Sanders and Starke [1] and Jata and Starke [3]. These investigators suggest that τ_p itself is an indicator, arguing that if little softening is possible localization cannot result even if the softening occurs rapidly. This indicator predicts coarser slip with increasing particle size. Hornbogen and Zum Gahr [4] combine these ideas in a third alternative

$$\frac{\tau_p}{\tau_p + \tau_0} |\partial\tau_p/\partial n| \quad (4)$$

where $\tau_p + \tau_0$ is the yield stress of the material. This indicator is monotonically decreasing in r_p and thus predicts coarser slip for smaller particles, again contrary to observation.

In summary, the indicators proposed are based on a microscopic model of softening and on the intuitive notion that localized slip occurs because a given slip plane is weaker than its neighbors. But the indicators do not give a quantitative connection between slip localization and alloy properties. The task of constructing a quantitative microscopic model of slip is taken up in the following section.

2. A MODEL OF SLIP LOCALIZATION

The indicators discussed above are all based on a simple and accurate model of the strength due to the presence of second-phase particles and the degradation of that strength with slip. We augment this basic model by also considering the strengthening effect of dislocation pile-ups. Whether or not a particular slip plane undergoes a net weakening with slip will depend on the relative intensities of these two competing mechanisms, which in turn depend on material parameters and the current distribution of slip in the material.

The model we propose does not account for many subtle factors, including interaction between slip planes, the nature of dislocation sources present and the full variety of possible hardening and softening mechanisms. In the following we introduce an indicator of slip localization that agrees qualitatively with observations and, through rudimentary kinematic arguments, we derive an expression for the slip band spacing.

2.1. The slip intensity indicator

We assume that if slip weakens a particular plane then slip will continue on that plane until it regains the strength it had when softening commenced. During this process hardening does not begin until the strength due to the particles has been completely exhausted, thus a large amount of local slip can occur in this instance.

We take the number of dislocations N that pass on a typical slip plane from the time deformation begins until local slip ends to be an indicator of slip localization. The larger the slip intensity as measured by N , the coarser the deformation expected. The direct

connection between N and the simple intergranular fracture mechanism discussed above makes N a convenient indicator. The stress concentration at the grain boundary associated with the pile-up of N dislocations is $\tau^* = N\tau_p$, where τ_p is the resolved shear stress. If τ^* exceeds the crack nucleation stress at the grain boundary, intergranular fracture starts.

By considering the strengthening effects of both the second-phase particles and the dislocation pile-ups at the grain boundaries, the strength of a particular slip plane can be written as

$$\tau = \tau_0 + C_p \rho^{1/2} (r_p - nb/2)^{1/2} + C_b nb/r_G \quad (5)$$

where r_G is the grain radius and C_b is a constant that depends on the elastic properties of the bulk material. The third term on the right can be regarded as the backstress at the grain center due to a superdislocation (with Burgers' vector nb) at the grain boundary or as the backstress at the tail end of a pileup of length r_G containing n dislocations. With either interpretation it is an approximate measure of the inhibiting effect of the pile-up on subsequent slip. An additional term representing the strength due to pile-ups on other slip planes is not included. Although the contribution from this term is of the order of the last term on the right, it is not a function of n and does not affect the calculation of N . It may be thought of as contributing to τ_0 , which represents the background strength of the material.

We have assumed that if slip weakens a particular plane that slip will continue on that plane until it regains the strength it had when the softening commenced. Softening, that is the degradation of strength with increasing n , is indicated by the derivative of τ with respect to n being less than or equal to zero. Note that softening must occur for some value of n according to equation (5) because the contribution to $\partial\tau/\partial n$ from the particle strengthening term is negative and grows infinitely large as n approaches $2r_p/b$. The slip intensity N is calculated below for the two possible regimes: (I) if $\partial\tau/\partial n \leq 0$ prior to deformation then softening occurs immediately; (II) if $\partial\tau/\partial n > 0$ prior to deformation then hardening will occur initially and softening will occur only after some slip has taken place.

(I) *Softening occurs initially.* Softening occurs initially if $\partial\tau/\partial n \leq 0$ and continues as long as this inequality holds. Written explicitly and solved for r_p the inequality is

$$r_p \leq \frac{nb}{2} + \rho r_G^2 \left(\frac{C_p}{4C_b} \right)^2 \quad (6)$$

Given the grain size, the particle volume fraction and the material properties, equation (6) is satisfied only for sufficiently small particle radius. In this instance slip will continue until τ again reaches its initial value, thus

$$N = \rho^{1/2} r_p^{1/2} r_G \frac{C_p}{C_b b} \quad (7)$$

Although we are primarily interested in the dependence of N on r_p , equation (7) also gives the dependence of N on r_G and ρ in the case that softening occurs initially. The slip intensity N increases with the square root of both the particle volume fraction and the particle radius and increases linearly with the grain radius.

(II) *Hardening occurs initially.* Hardening occurs initially if $\partial\tau/\partial n > 0$ and continues as long as

$$r_p > \frac{nb}{2} + \rho r_G^2 \left(\frac{C_p}{4C_B} \right)^2 \quad (8)$$

holds. Those planes initially more susceptible to slip than others, because they contain dislocation sources or other stress concentrators for instance, will share the deformation until the first one begins to soften. This occurs when the maximum strength has been reached after

$$n_1 = \frac{2}{b} r_p - \frac{2}{b} \rho r_G^2 \left(\frac{C_p}{4C_B} \right)^2 \quad (9)$$

dislocations have passed. The calculation of the value of the maximum strength on a particular plane is complicated by the presence of pile-ups on neighboring planes. However, once weakening has started, slip will continue until the strength returns to this maximum value, thus

$$N = \frac{2}{b} r_p + \frac{2}{b} \rho r_G^2 \left(\frac{C_p}{4C_B} \right)^2. \quad (10)$$

Again, equation (10) gives the dependence of N on ρ and r_G as well as the dependence of N on r_p in the case that hardening occurs initially. The slip intensity N increases linearly with r_p and ρ and increases as the square of r_G .

2.2. Slip band spacing

Consider a cubic grain with edge length $2r_G$ and suppose the grain is subjected to a shear strain γ . We assume that γ , although small, is much larger than r_p/r_G . (In Al-Li alloys this latter ratio is typically 10^{-4} .) This assumption insures that enough slip occurs so that the particles are completely sheared on

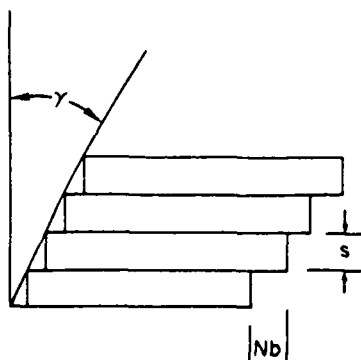


Fig. 1. A kinematic model relating the slip intensity N to the imposed strain γ and the slip band spacing s .

many different planes. We also neglect elastic strains. Then

$$s = Nb/\gamma \quad (11)$$

where s is the band spacing from center to center (see Fig. 1). Terlinde and Luetjering [5] present a more carefully derived relation that gives the same proportionality between s and N under the assumptions stated above.

3. DISCUSSION OF THE PRESENT MODEL

It has been shown that for a given strain γ the slip band spacing is directly proportional to the slip intensity N . The influence of the variable parameters r_p , r_G and ρ on N , as expected in equations (7) and (10), will be discussed for each of the variables separately.

3.1. Influence of particle radius

For constant values of ρ and r_G and sufficiently small values of r_p initial softening occurs (regime I), as illustrated in Fig. 2. Alternatively, if r_p is sufficiently large, again for constant values of ρ and r_G , initial hardening occurs (regime II), as illustrated in Fig. 3. The dependence of slip intensity N on particle

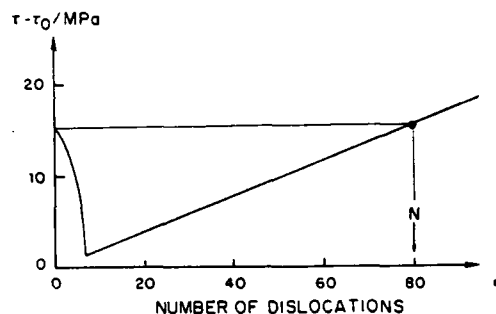


Fig. 2. Initial softening (regime I). Strength vs slip for Ti-6Al-4V $r_p = 1$ nm, $\rho = 0.01$ and $r_G = 30 \mu\text{m}$.

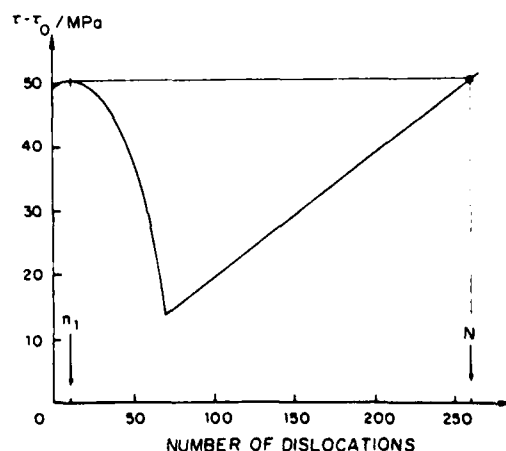
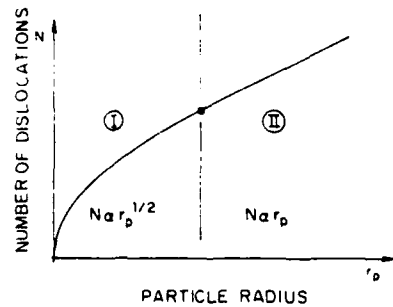
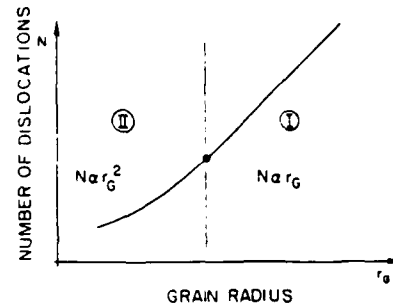


Fig. 3. Initial hardening (regime II). Strength vs slip for Ti-6Al-V $r_p = 10$ nm, $\rho = 0.01$ and $r_G = 30 \mu\text{m}$.

Fig. 4. Slip intensity N vs particle radius r_p .Fig. 6. Slip intensity N vs grain radius r_G .

radius is depicted schematically in Fig. 4, and the separation of regimes I and II is indicated there. For sufficiently small particle radius (regime I), N is proportional to $r_p^{1/2}$, whereas for sufficiently large particle radius (regime II) N increases linearly with r_p . We emphasize that in either case slip localization is enhanced as the particle radius increases. Increasing N also means increasing the slip-band spacing, according to equation (11).

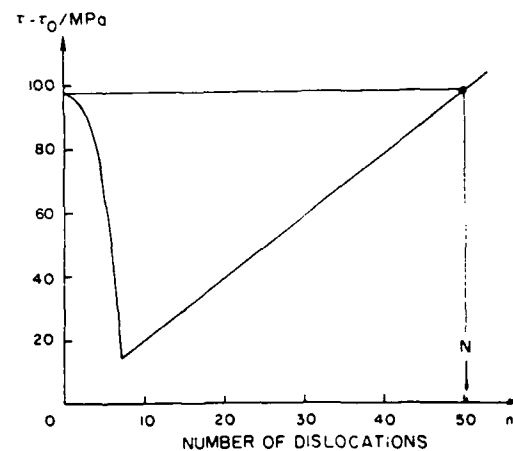
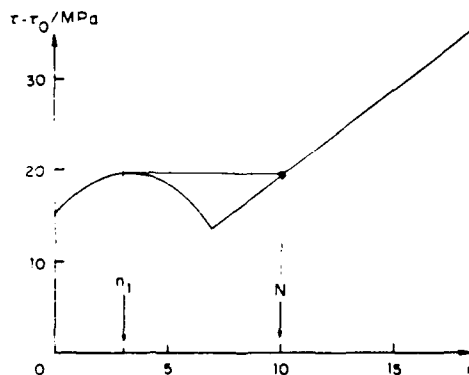
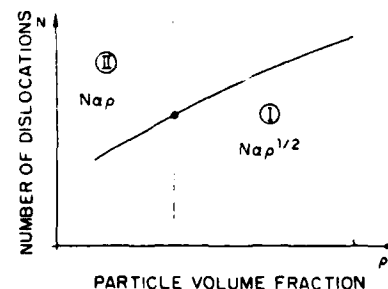
3.2. Influence of grain size

For constant values of ρ and r_p and sufficiently small values of r_G initial hardening takes place (regime II), as illustrated in Fig. 5. If r_G is sufficiently large, again for constant values of ρ and r_p , initial softening (regime I) takes place, as illustrated in Fig. 2. The slip intensity N increases as the square of the grain radius for sufficiently small grains (regime II) and increases linearly with grain size for sufficiently large grains (regime I). The dependence of slip intensity N on grain radius is depicted schematically in Fig. 6, and the separation of regimes I and II is indicated there.

3.3. Influence of particle volume fraction

For practical applications the variation in particle volume fraction is only of subordinate importance but shall be discussed for completeness. For suffi-

ciently small values of ρ and constant values of r_G and r_p initial hardening occurs (regime II), as depicted in Fig. 5. For sufficiently large values of ρ and constant values of r_G and r_p initial softening occurs (regime I), as shown in Fig. 7. The dependence of the slip intensity N on particle volume fraction is depicted schematically in Fig. 8, and the particle volume fraction separating regimes I and II is indicated. The slip intensity N is proportional to $\rho^{1/2}$ for sufficiently large particle volume fractions (regime I) and is proportional to ρ for sufficiently small particle volume fractions (regime II).

Fig. 7. Initial softening (regime I). Strength vs slip for Ti-6Al-4V $r_p = 1$ nm, $\rho = 0.4$ and $r_G = 3$ μ m.Fig. 5. Initial hardening (regime II). Strength vs slip for Ti-6Al-4V $r_p = 1$ nm, $\rho = 0.01$ and $r_G = 3$ μ m.Fig. 8. Slip intensity N vs particle volume fraction ρ .

4. CONCLUSIONS

A microscopic model of slip in particle reinforced alloys has been proposed that predicts coarser slip for larger particles for a fixed particle volume fraction and grain size. Simple kinematic arguments also have been proposed that yield estimates of the slip band spacing in such alloys and their dependence on particle size, particle volume fraction and grain size. Data presented by Jata and Starke [3] support the contentions above in as much as the trends in the data for band spacing and band width are consistent with expectations based on the above analysis. This model predicts decreasing strains to fracture with increasing particle size. Terlinde and Luetjering [5] have produced a model of tensile fracture for a Ti-Al alloy based on the localization of slip within grains and the associated stress concentrations at the grain

boundaries due to pile-ups. Their results too are consistent with the above analysis.

Acknowledgements—Two of the authors, J. M. Duva and E. A. Starke, wish to acknowledge support by the Air Force Office of Scientific Research, U.S. Air Force Systems Command, under Grant AFOSR-83-0061, Dr Alan H. Rosenstein, Program Manager.

REFERENCES

1. T. H. Sanders Jr and E. A. Starke Jr, *Acta metall.* **30**, 927 (1982).
2. J. W. Martin, *Micromechanisms in Particle-Hardened Alloys*, Cambridge University Press (1980).
3. K. V. Jata and E. A. Starke Jr, *Metall. Trans. A*, **17A**, 1011 (1986).
4. E. Hornbogen and K. H. Zum Gahr, *Metallography* **8**, 181 (1975).
5. G. Terlinde and G. Luetjering, *Metall. Trans. A* **13A**, 1283 (1982).

THE INFLUENCE OF Mn DISPERSOID CONTENT AND STRESS STATE ON DUCTILE FRACTURE OF 2134 TYPE Al ALLOYS

J. A. WALSH¹, K. V. JATA² and E. A. STARKE JR³

¹Northrop Aircraft Corporation, Hawthorne, CA 90250, ²University of Dayton Research Institute, Dayton, OH 45469 and ³Department of Materials Science, University of Virginia, Charlottesville, VA 22901, U.S.A.

(Received 15 February 1989; in revised form 17 May 1989)

Abstract—Ductile fracture studies have been conducted on four high purity Al-Cu-Mg-Zr (2134 type) alloys containing 0, 0.31, 0.61 and 1.02 wt% Mn in the under and overaged conditions having similar yield strengths. The second phase particle content, i.e. Mn rich dispersoids and Mn containing large particles, increased with increasing Mn content. In both aging conditions maximum ductility and toughness were observed for the 0.31% Mn alloy and minimum values were observed for the 1.02% Mn alloy. The largest void content or damage accumulation due to void nucleation and growth at any strain level occurred in the 1.02% Mn alloy, consistent with ductility values. The 0.31% Mn alloy showed the highest ductility in both aging conditions. Although the void volume fractions for the 0.31% Mn alloy were similar to those of the 1.02% Mn alloy, accumulation occurred at higher strains. The void nucleation and growth data and microstructural analysis suggest that the 0.31% Mn additions provide sufficient submicrometer Mn-dispersoids to homogenize slip without producing large Mn-rich primary particles which decrease ductility. Ductility was observed to decrease with increasing triaxial constraint which increased void volume fraction and void growth rates. However, the degree of triaxiality had little or no effect on the nucleation rate of voids.

Résumé—Des études de rupture ductile ont été effectuées sur quatre alliages Al-Cu-Mg-Zr (type 2134) de haute pureté contenant 0, 0.31, 0.61 et 1.02% en poids de Mn et ayant des limites élastiques identiques dans des conditions de sous- et de survieillessement. La teneur en particules de seconde phase, c'est à dire la phase dispersée riche en manganèse et les grandes particules contenant du Mn, augmente lorsque la teneur en Mn croît. Dans les deux conditions de vieillissement, la ductilité et la dureté maximales sont observées pour un alliage à 0.31% de Mn et les valeurs minimales, pour un alliage à 1.02% de Mn. La plus grande teneur en cavités ou l'accumulation maximale de dégâts due à la germination et à la croissance de cavités à tous les niveaux de déformation se produit pour l'alliage à 1.02% de Mn, en accord avec les valeurs de la ductilité. L'alliage à 0.31% de Mn révèle la plus forte ductilité dans les deux conditions de vieillissement. Quoique la fraction volumique de cavités pour l'alliage à 0.31% de Mn soit similaire à celle de l'alliage à 1.02% de Mn, une accumulation se produit aux fortes déformations. Les données sur la germination et la croissance des cavités, ainsi que l'analyse microstructurale suggèrent que l'addition de 0.31% de Mn fournit suffisamment de dispersoïdes submicrométriques de Mn pour homogénéiser les glissements sans produire de grandes particules primaires riches en Mn qui abaissent la ductilité. On observe que la ductilité diminue lorsque la contrainte triaxiale croît, ce qui augmente la fraction volumique de cavités et leur vitesse de croissance. Cependant, le degré de triaxialité a peu ou pas d'effet sur la vitesse de germination des cavités.

Zusammenfassung—Der duktile Bruch wurde an vier hochreinen Al-Cu-Mg-Legierungen (Typ 2134), die 0, 0.31, 0.61 und 1.02 Gewichtsprozent Mn enthielten, im unter- und überlagerten Zustand bei vergleichbaren Fließfestigkeiten untersucht. Der Gehalt an zweiten Phasen, d.h. Mn-reiche Dispersoide und große Mn-haltige Teilchen, nahm mit steigendem Mn-Gehalt zu. In beiden Auslagerungszuständen waren Duktilität und Zähigkeit in der Legierung mit 0.31% Mn am höchsten, kleinste Werte fanden sich in der Legierung mit 1.02% Mn. Der größte Gehalt an Poren oder die größte Schadensanhäufung durch Porenbildung und -wachstum trat bei jedem Dehnungsgrad in der Legierung mit 1.02% Mn auf, übereinstimmend mit den Werten für die Duktilität. Die Legierung mit 0.31% Mn hatte die höchste Duktilität bei beiden Auslagerungszuständen. Wenn auch in dieser Legierung der Volumanteil der Poren dem der Legierung mit 1.02% Mn ähnelte, so trat die Schadensanhäufung erst bei höheren Dehnungen auf. Die Ergebnisse zu den Poren und die Analyse der Mikrostruktur legen die Auffassung nahe, daß Zugabe von 0.31% Mn genügend Mn-Dispersoide im Submikrometer-bereich bilden, um die Gleitung zu homogenisieren, ohne daß sich große Mn-haltige Teilchen bilden, die die Duktilität verringern. Die Duktilität nahm ab mit zunehmender dreiachsiger Einschränkung, wodurch der Volumanteil der Poren und die Wachstumsraten der Poren zunehmen. Jedoch beeinflusste der Grad der Dreiachsigkeit die Keimbildungsrate der Poren kaum oder garnicht.

INTRODUCTION

Ductile fracture involving void nucleation, growth and coalescence is commonly observed in alloys

containing second phase particles. Microstructure and state of stress generally have large effects on the ductile fracture process, and thus this area of research has received a great deal of attention [1-10]. Alu-

Table 1. Actual chemical compositions (wt%)

Alloy	Cu	Mg	Mn	Si	Fe	Ti	Zr	Al
1	3.96	1.48	—	0.04	0.06	0.01	0.14	Balance
2	3.96	1.46	0.31	0.04	0.06	0.01	0.12	Balance
3	4.18	1.46	0.60	0.04	0.06	0.01	0.11	Balance
4	4.51	1.47	1.02	0.04	0.06	0.02	0.12	Balance

minum alloys fall into this group and generally display ductile fracture under monotonic loading in both notched and unnotched conditions. Aluminum alloys normally contain three classes of particles: coarse constituents, dispersoids, and strengthening precipitates [11]. The coarse constituent particles are detrimental to fracture toughness and result from the presence of Fe and Si impurities or excessive amounts of major alloying elements such as Mg, Zn and Cu. The final size of the constituents depends upon the fabrication procedure and may range in size from 5 to 30 μm . Dispersoids range in size from 0.02 to 0.5 μm , in the largest dimension, and normally precipitate during the ingot pre-heat and homogenization treatment. These particles form from elements added to control grain size and or suppress recrystallization. Dispersoids may also play a major role in controlling the fracture toughness since voids formed at large constituents may join up through void sheet formation at dispersoids. Strengthening precipitates are in the nanometer-size range and form in grain interiors. They largely control the strength and slip behavior of the alloy and indirectly influence fracture toughness. In addition, heterogeneous precipitation occurs at grain boundaries, and, although these precipitates have little or no effect on strength, they may have significant effect on fracture behavior. Usually Fe and Si-rich particles or any large undissolved strengthening phase are void initiation sites in aluminum alloys. In alloy 2024 void initiation has been found to occur at $\text{Al}_2\text{Cu}_2(\text{Fe, Mn})_3$, Mg_2Si and Al_2Cu particles followed by void sheet formation at submicrometer-sized particles such as Mn-rich dispersoids [12]. Even in high purity aluminum alloys containing low levels of Fe and Si, void initiation associated with particle cracking and particle-matrix decohesion has been reported to occur at $\text{Al}_{20}\text{Cu}_2(\text{Fe, Mn})_3$ and Al_2CuFe constituents [13, 14]. Much of the previous work on Al alloys has focused on fracture toughness studies and correlation of fracture in the process zone ahead of the crack tip with microstructural features and deformation behavior [15–17]. Correlations between volume fraction and size of the second phase particles, strain hardening exponent, and fracture toughness have shown that improvements in ductility toughness of Al alloys may be obtained if the volume fraction of large second phase particles is minimized. However, studies pertaining to the details of void initiation, growth and coalescence stages have not been conducted. The present work was undertaken to study these stages in

2134-type Al alloys containing various volume fractions of Mn-rich particles. These alloys are attractive from a commercial point of view since Mn additions result in a desirable combination of strength, ductility and corrosion resistance [18]. The effects of aging, deformation mode, Mn content and state of stress on void nucleation, growth and coalescence have been examined.

EXPERIMENTAL

The materials used for this study were four 2134-type Al–Cu–Mg–Zr alloys with traces of Si, Fe, Ti and varying amounts of Mn. The actual chemical compositions are given in Table 1. The alloys were obtained from the Reynolds Metal Company in the form of 20.32 mm. thick plates. These were hot rolled between 371–471°C, solutionized at 493°C for 1.5 h, water quenched and stretched 2.5% to obtain the T351 temper. The alloys were aged at 190°C between 2–4 h to obtain an underaged condition and for 24 h to obtain an overaged condition. Details of grain size measurement, quantitative analysis of particle distribution and spacing are described elsewhere [19]. Tensile testing of both smooth and notched tensile specimens was performed at $1 \times 10^{-3} \text{ s}^{-1}$. Void volume fractions, voids/area and void sizes in deformed tensile specimens were measured, and the procedures are described in detail in Ref. [19]. In brief, (i) volume fraction of voids was obtained through a picnometer by measuring densities of the deformed gage section or neck and the grip part. V_f was then calculated as

$$V_f = (d_{\text{grip}} - d_{\text{neck}})/d_{\text{grip}}$$

(ii) voids/area was obtained at $1000\times$ at the center line of the deformed specimen and (iii) average maximum void size was determined at $9000\times$ in the same region. The effect of stress state (triaxiality) was studied only in the 0.61% Mn alloy. The triaxiality was approximated using Bridgmann's equation (20)

$$\sigma_t/Y = 1.3 + \ln[(a/2R_0) + 1]$$

where

σ_t = triaxial or mean stress

R_0 = radius of curvature of neck

a = minimum radius

Y = flow stress.

This equation was used to determine the starting and final triaxialities. The starting triaxialities may not be exact since the neck is machined and not natural. However, during deformation of the hourglass specimens, the requirements for a natural neck are asymptotically reached [21]. The notched specimens were strained and void growth studies were conducted in a manner similar to the smooth samples described above.

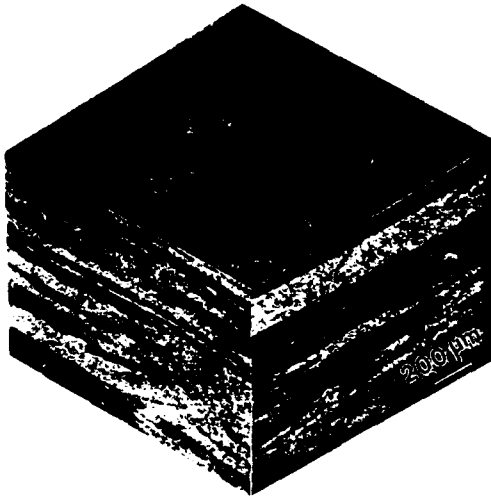


Fig. 1. Optical micrograph illustrating the typical pancake shaped grains for 2134-type Al alloys.

EXPERIMENTAL RESULTS

Microstructure and mechanical properties

The grain size values for the four alloys ranged between 185 to 211 μm , and a typical grain structure is shown in Fig. 1. All of the alloys are in the unrecrystallized condition, and the subgrain structure is shown in the TEM micrographs of Fig. 2(a)–(d). In the same micrographs the increase in the volume fraction of Mn dispersoids with increasing Mn addition can be noted. The major strengthening phases, Al_2CuMg and Al_2Cu in the 2134-type alloys, are similar to those in 2124. The deformation mode of similar age hardenable Al alloys is normally localized (heterogeneous) in the underaged condition and homogeneous (dispersed) in the overaged condition. Mn dispersoids are looped in both under and overaged conditions due to their incoherent nature. Thus increasing the Mn content is expected to enhance homogeneity of slip [22–24].

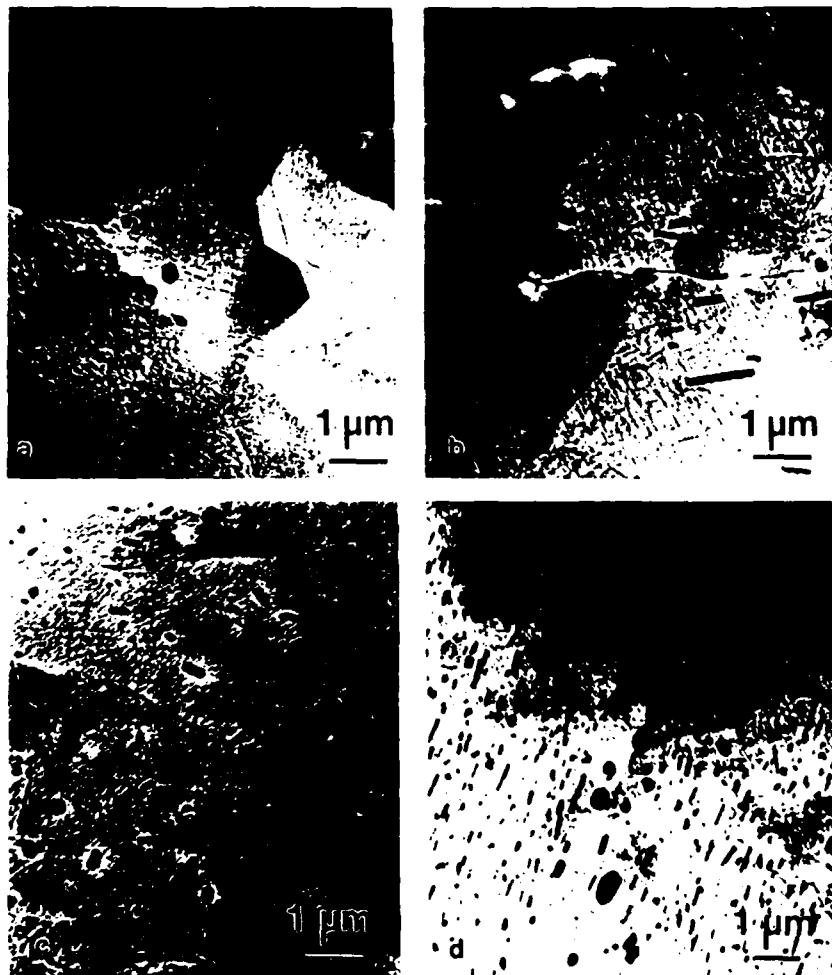


Fig. 2. Bright field transmission electron micrographs showing the effect of Mn composition on the volume fraction of dispersoids (a) 0% Mn, (b) 0.3% Mn, (c) 0.6% Mn, and (d) 1.02% Mn alloys.

Table 2. Large particle distribution and spacing parameters

Alloy	V_v	N_v (mm ⁻²)	N_l (mm ⁻¹)	λ (mm)	σ (mm)
1	0.0175	589	5.2	0.19	0.19
2	0.0196	686	5.5	0.18	0.18
3	0.0220	722	6.63	0.15	0.15
4	0.0407	1129	10.6	0.091	0.095

Large constituent particles which are potential nucleation sites for void initiation were observed both at the grain boundaries and grain interior. Their size and spacing are given in Table 2. Large undissolved primary Al_2CuMg was observed in all the alloys. In the 0.31% Mn, 0.61% Mn and 1.02% Mn alloys, $\text{Al}_{20}\text{Cu}_2\text{Mn}_3$ and $\text{Al}_{20}\text{Cu}_2(\text{Mn, Fe})_3$ were also identified. Al_2CuMg and $\text{Al}_{20}\text{Cu}_2\text{Mn}_3$ were typically more spherical than the $\text{Al}_{20}\text{Cu}_2(\text{Mn, Fe})_3$. The $\text{Al}_{20}\text{Cu}_2(\text{Mn, Fe})_3$ particles had a higher aspect ratio than the Al_2CuMg particles and had a greater tendency to appear as stringers [19]. During straining this gave rise to multiple void nucleation sites along the length of the $\text{Al}_{20}\text{Cu}_2(\text{Mn, Fe})_3$ particles, whereas the more equiaxed primary Al_2CuMg and large Mn-rich dispersoids failed by decohesion along the particle/matrix interface, Fig. 3. Because the majority of the constituent and dispersoid particles lie in the grain interior, both the under and overaged Mn-containing alloys failed by a transgranular fracture. In the 0% Mn overaged alloy, shallow ductile void growth along the precipitate free zone is observed, while in the underaged case deeper voids and slip band fracture occurred. Fractographs illustrating these features are shown in Fig. 4(a)–(d).

The mechanical properties in the under and overaged conditions are shown in Table 3. In all the alloys overaging resulted in a higher fracture strain compared to the underaged condition, but the fracture toughness was lower for the overaged alloys. In the notched samples, the overaged alloys showed lower fracture strains than the underaged ones. In both aging conditions the fracture strain and fracture toughness are highest in the 0.31% Mn alloy and lowest in the 1.02% Mn alloy.

Damage from void nucleation and growth in smooth tensile specimens

Measurements of void volume fractions, V_v , in deformed specimens reflect the combined damage due to void nucleation and growth that occur during straining. V_v for the four Mn levels are shown in Fig. 5 (a)–(d), and a comparison between under and overaged conditions can be made from this figure. In the early stages of deformation, the void volume fractions of under and overaged specimens are equivalent, but as deformation proceeds the overaged alloys continue to exhibit a higher resistance to damage consistent with the observed higher ductility levels in the smooth overaged samples. This data also indicates that the final or critical void volume fractions V_{vc} (marked as X in the figure) needed to

fracture the underaged samples is lower than required for the overaged samples. In both aging conditions Mn additions, or an increase in the volume fraction of second phase particles, result in an increase in the void volume fraction. However, the critical void volume fraction does not decrease with decrease in ductility, Fig. 6(a) and (b). The rate of damage accumulation with respect to strain increases with increasing Mn content and is substantially higher for the 1.02% Mn alloy which contains the largest volume fraction of closely spaced incoherent particles when compared to the other three alloys.

Damage from nucleation of voids in smooth tensile specimens

The number of voids per mm² (areal void density) was obtained as a function of strain on deformed specimens at 1000 \times , using the scanning electron microscope. Data was taken until the standard deviation remained constant within 5% to assure statistical confidence. The results for the under and overaged conditions and for different levels of Mn are shown in Fig. 7. These results indicate that the

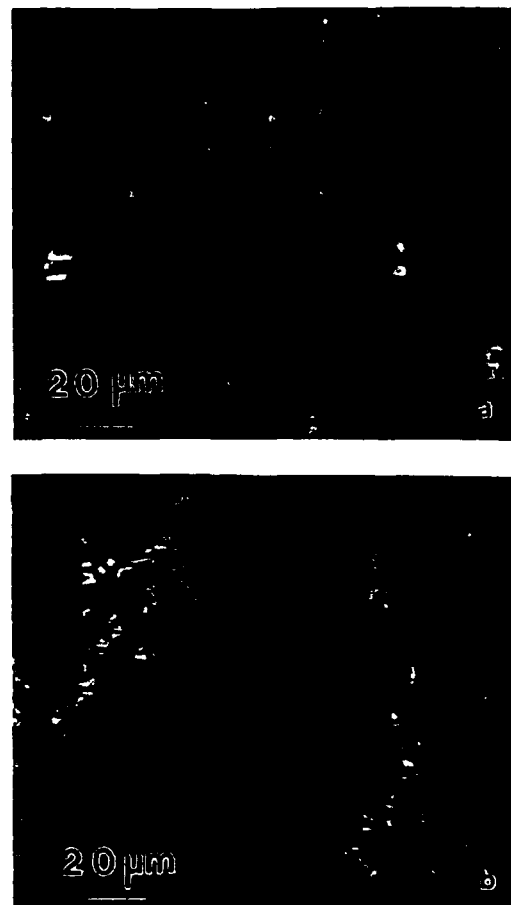


Fig. 3. Optical micrographs showing the voids associated with large constituent particles in (a) 0% Mn and (b) 1.02% Mn alloys.

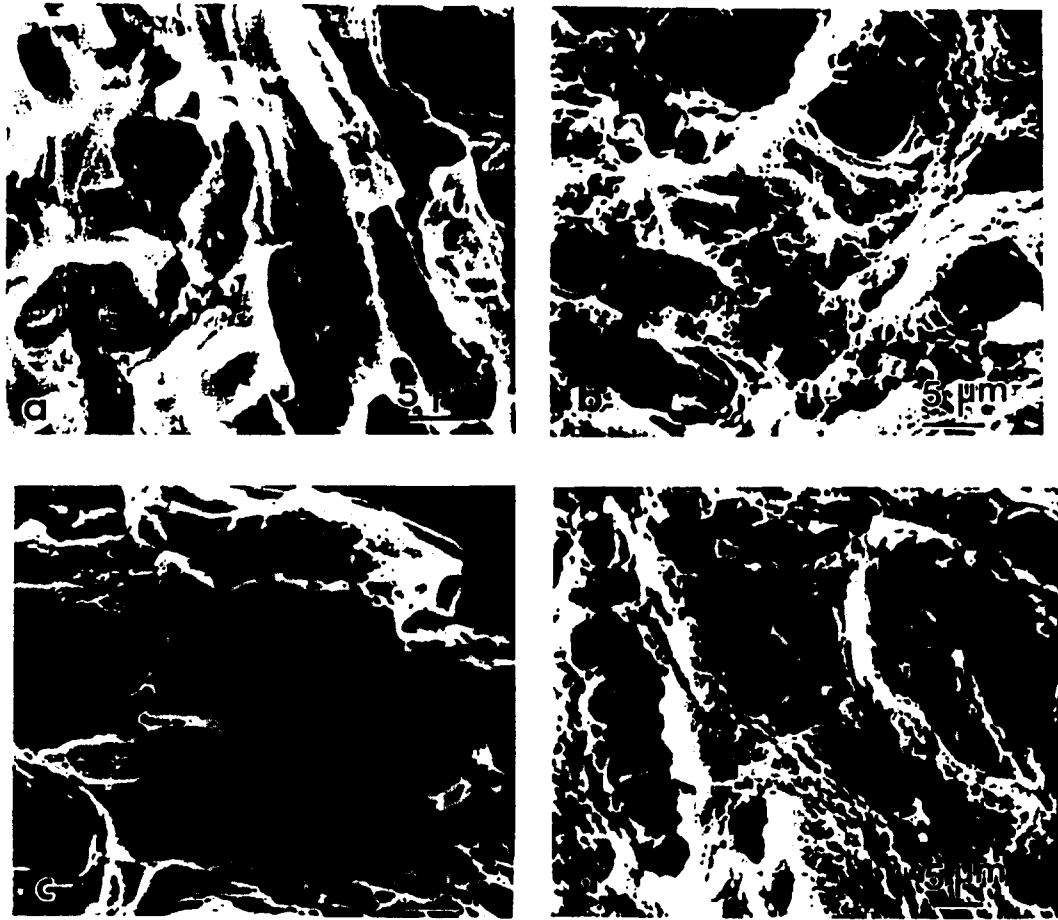


Fig. 4. Comparison of fracture surfaces in (a) 0% Mn and (b) 1.02% Mn underaged alloys; (c) 0% Mn and (d) 1.02% Mn overaged alloys.

increase in the areal void density is linear with deformation and furthermore that voids are being continually nucleated as deformation proceeds. The slopes of the lines suggest that the void nucleation rate is much higher in the 1.02% Mn alloy in both aging conditions. The high nucleation rate of voids in the 1.02% Mn alloy is due to a greater volume fraction and closer spacing of large stringer type particles which provide multiple nucleation sites. Argon *et al.* [6] have suggested that when large particles are closely spaced their stress/strain fields may interact, giving rise to higher local stress/strain

than otherwise anticipated thus enabling critical stress/strain for void nucleation/growth to be attained at lower applied strains.

In the overaged condition the 1.02% Mn alloy exhibits two nucleation rates: a lower nucleation rate at low strain levels and an accelerated nucleation rate at higher strains. Argon *et al.* [6] observed a dependence of interfacial stress on the local volume fraction of second phase particles after moderate amounts of strain, in situations where the local volume fractions exceeded the average volume fraction of large particles. The particle stress field interaction is initially

Table 3. Room temperature mechanical properties

Alloy	σ_y (MPa)	σ_{UTS} (MPa)	n	$\ln A_0/A_f$	%RA	K_{IS} (MPa m)
1 UA	376	431	0.052	0.409	33.7	52
OA	447	481	0.036	0.573	43.2	39
2 UA	403	443	0.065	0.444	37.4	53
OA	448	478	0.037	0.644	48.8	45
3 UA	414	498	0.060	0.377	37.7	52
OA	467	512	0.053	0.421	42.1	44
4 UA	425	491	0.057	0.217	17.8	32
OA	451	493	0.041	0.305	26.2	27

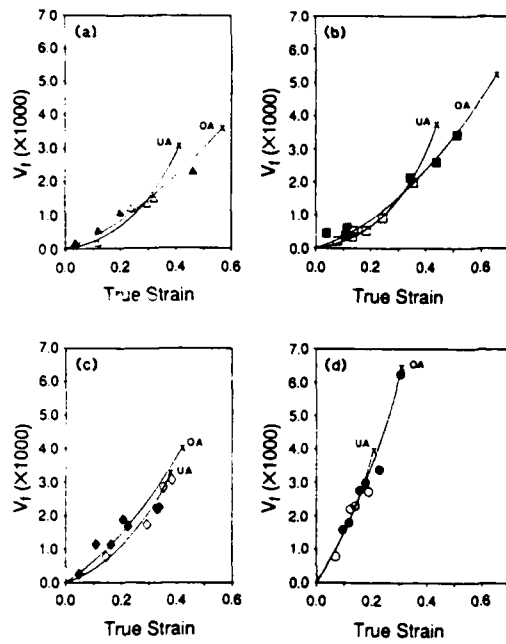


Fig. 5. Comparison of void volume fractions vs true strain for under and overaged conditions in (a) 0% Mn, (b) 0.3% Mn, (c) 0.6% Mn, and (d) 1.02% Mn.

insignificant but once necking occurs the stress field could build up to an extent whereby large numbers of particles could nucleate voids. The same phenomenon is not observed in the underaged case since particle interaction can occur locally for smaller strains due to localized slip. The difference in the nucleation rate between under and overaged 0.61% Mn and 1.02% Mn alloys is not significant, but the 0% Mn and 0.31% Mn underaged alloys display greater nucleation rates than the overaged alloys. Thus a change in the deformation mode from localized slip in the

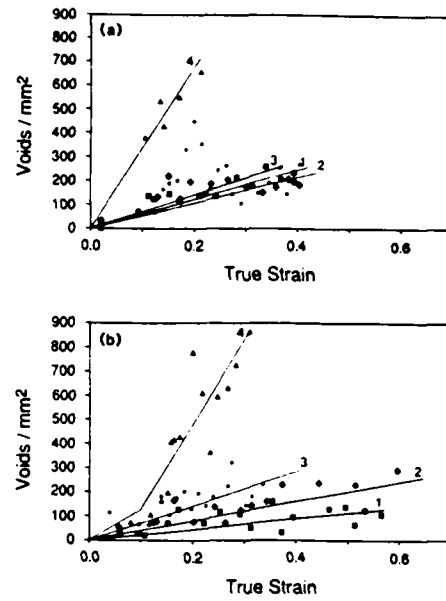


Fig. 7. Areal void density vs true strain for 0-1.02% Mn content in (a) underaged and (b) overaged.

underaged to dispersed slip in the overaged, affects the 0.0% Mn and 0.31% Mn alloys more than the higher Mn-containing alloys.

The higher degree of homogeneous slip in the overaged alloys reduces the local critical stress/strain concentration to cause particle fracture or decohesion in the 0.0% Mn and 0.31% Mn alloys. The underaged condition, on the other hand, provides local increases in stress/strain due to localized slip. The increase in nucleation rate and the number of voids/mm² is in fact observed to be greatest for the 0.0% Mn underaged alloy which exhibits the highest degree of localized slip. The higher levels of Mn in the

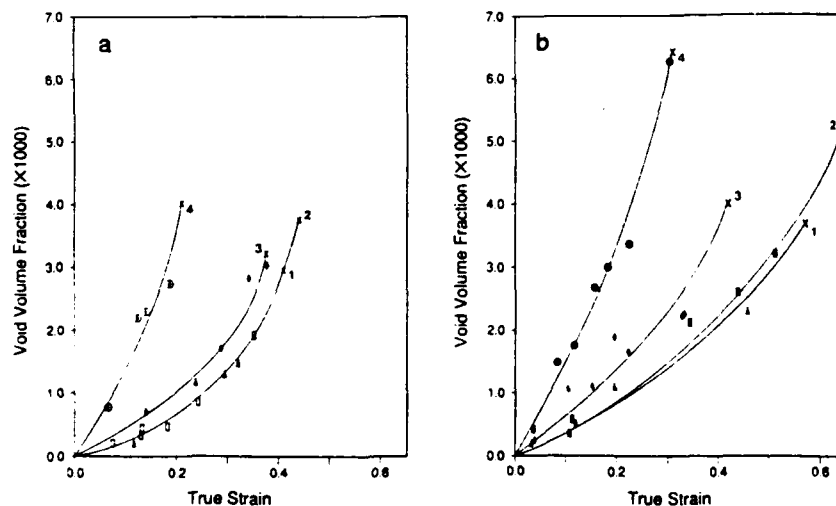


Fig. 6. Comparison of void volume fractions vs true strain for 0 to 1.02% Mn content in (a) underaged; (b) overaged.

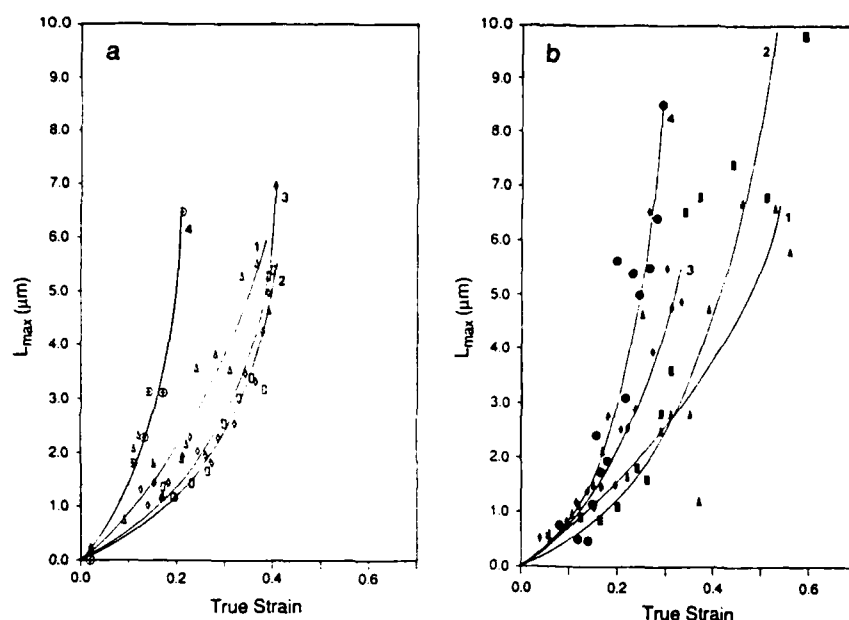


Fig. 8. Average maximum void size vs true strain for 0-1.02% Mn content in (a) underaged and (b) overaged.

0.61% Mn and 1.02% Mn alloys not only increase the dispersoid population but also homogenize slip in the underaged condition. Hence, the under and overaged alloys show similar nucleation behavior. However, due to a larger volume fraction of large particles the 0.61% Mn and 1.02% Mn alloys have larger areal void density than either the 0.0% Mn or 0.31% Mn alloys.

Damage from void growth

The average maximum void size, L_{max} , measured as a function of strain, along the stress axis where void growth is maximized, is shown in Fig. 8 (a) and (b). In the transverse direction void growth was not noticeable until very high triaxialities were reached, almost near fracture in the smooth specimens. Therefore, L_{max} was measured as a function of strain only along the stress axis. In both aging conditions, the 1.02% Mn alloy shows a much larger void size than the other alloys at comparable strain levels. The largest void size is attained at a lower strain level in this alloy and, therefore, the void growth rate is also the highest. Additions of Mn in the overaged alloys result in an increase in the average maximum void size with deformation. In the underaged alloys this trend is obeyed by the 0.31, 0.61 and 1.02% Mn alloys. The 0.0% Mn alloy shows a larger void size than either the 0.31 or 0.61% Mn alloys.

A comparison of void size in the under to the overaged alloys suggests that the underaged alloys not only exhibit a larger void size but also that the final void size just prior to fracture is reached at smaller macroscopic strains than in the overaged condition. Therefore, homogeneous deformation or

slip dispersal due to overaging reduces local deformation and thus reduces void growth. These results suggest that void sheet formation, which occurs prior to final fracture, takes place at lower strains in the underaged alloys which deform by localized slip. The differences in the void growth rates between the 0.0, 0.31 and 0.61% Mn overaged alloys do not appear to be significant.

Triaxiality effects

The effect of triaxiality on ductile fracture was examined in the 0.61% Mn alloy in the under and overaged conditions. The effects of triaxial stress state on fracture strain for the under and overaged alloys are shown in Fig. 9. σ_1/Y was determined from Bridgman's equation and was used as a measure of triaxiality. As the triaxiality increases, the strain to fracture drops more rapidly in the overaged alloy than in the underaged alloy. In fact, at the largest triaxial constraint ($T_3 = 2.04$), the overaged alloy has less than half of the fracture ductility of the underaged alloy: 0.053 as compared to 0.115.

The void volume fraction or damage accumulation was determined on samples with triaxialities ranging from T_0 to T_4 . In the T_3 condition, experimental determination of V_f was difficult due to an extremely small deformed volume (as expected in a near plane strain condition). As shown in Fig. 10, increasing the triaxial constraint results in a large increase in damage at any strain. However, the critical void volume fractions remain unaffected until the T_3 (0.556) condition is approached. At T_4 (1.02) there is a large decrease in the critical void volume fraction together with a large reduction in ductility. A similar result is

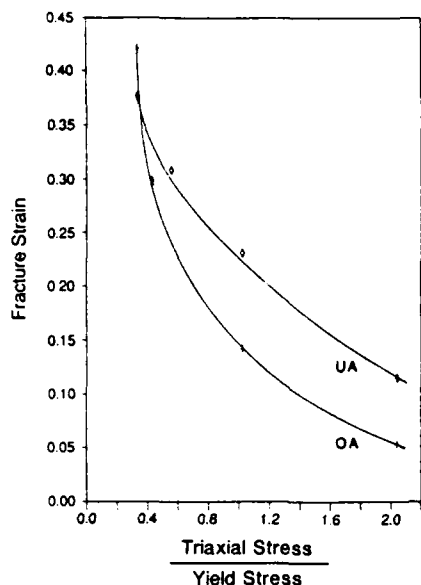


Fig. 9. Fracture strain vs triaxiality for the 0.6% Mn alloy in the underaged and overaged conditions.

also observed for the overaged alloy. Additionally, the overaged alloy exhibits greater damage than the underaged alloy for the T_4 condition. The higher damage accumulation in the overaged alloy gives rise to a lower fracture strain. The effect of triaxiality on the areal void density, Fig. 11(a) and (b), does not appear to be significant, except at the fracture strain (or just prior to fracture). The aging condition and the degree of triaxiality have no pronounced effect on the nucleation rate of voids. The maximum void size with strain is shown in Fig. 12(a) and (b), for the T_0 (0.333) and T_4 conditions. Since the voids/area parameter did not change sufficiently with triaxiality,

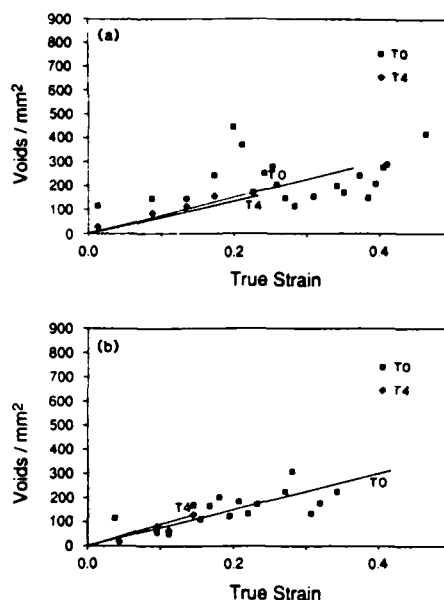


Fig. 11. Comparison of areal void density vs true strain for smooth and notched specimen of 0.6% Mn alloy. (a) Underaged condition and (b) overaged condition.

it is the void growth that contributes to the increased void volume fractions or damage associated with triaxiality. Fractographic results of 0.61% Mn overaged specimens in the T_2 (0.427) and T_4 conditions are shown in Fig. 13 and demonstrate the void size increase with increasing triaxiality.

DISCUSSION

The ductile fracture process of the 2134-type alloys is one of void nucleation, growth and coalescence. Void formation is observed to occur either through

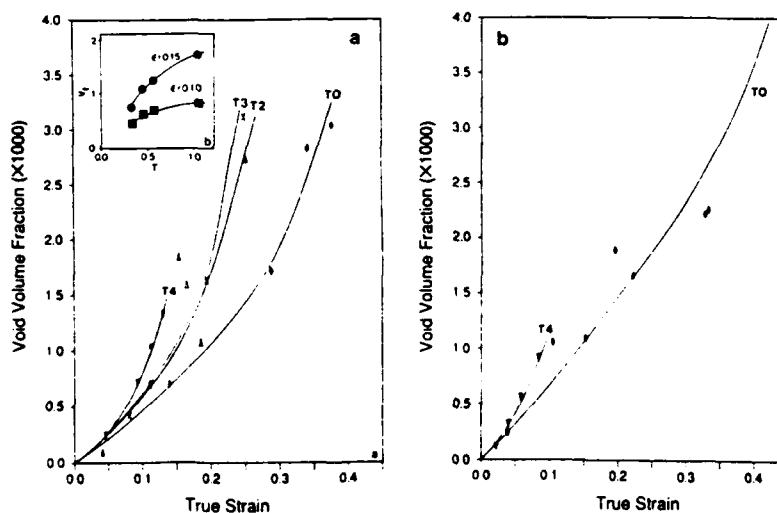


Fig. 10. Void volume fraction vs true strain for notched specimens of 0.6% Mn alloy in (a) underaged (b) overaged conditions. Inset: V_f vs triaxiality at 0.1 and 0.15 strain.

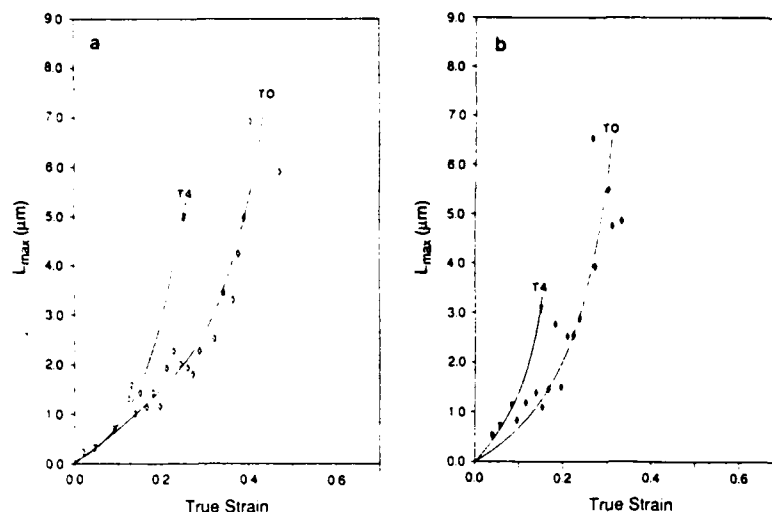


Fig. 12. Comparison of average maximum void size vs strain for smooth and notched specimen of 0.6% Mn alloy. (a) Underaged condition and (b) overaged condition.

the separation of the equiaxed $Al_{20}Cu_2Mn_3$ and Al_2CuMg constituents from the matrix or the brittle cracking of nonequiaxed $Al_{20}Cu_2(Mn, Fe_2)$ constituents. Although not common to most Al alloys, the 2134-type alloys exhibit higher ductilities for the

overaged condition than for the underaged condition in smooth samples where the triaxiality is low, 0.33. Corresponding to this high fracture strain, higher critical void volume fractions are also observed for the overaged alloys. Since the volume fraction and spacing of large void nucleating particles should not change with aging, it is the change in the deformation mode and the increase in the size and volume fraction of grain boundary particles that must produce this increase in the critical void volume fraction in the overaged alloys. The grain boundary particles contribute to the void volume fraction but do not seem to offer an easy path for linkage of the major voids that is sufficient to produce fracture in the overaged Mn-containing alloys. This conclusion can be derived from the fractographs of Fig. 4 which show only stable ductile void growth for both the under and overaged Mn-containing alloys. Smooth or shallow-dimple grain boundary rupture representative of low energy fracture is not observed in the Mn-containing alloys (compare the fractograph of the 1.02% Mn alloy with the 0.0% Mn alloy). Only the 0.0% Mn overaged alloy exhibits this behavior, but it does not result in a curtailment in ductility in the overaged case. Thus the results suggest that the homogeneous deformation observed for the overaged condition is an important factor that needs to be considered in order to explain the higher ductility.

The effects of deformation mode in these alloys are also reflected in other experimental results. Firstly, the number of voids/mm² is higher in the underaged alloys where localized deformation results in local stresses exceeding either the interfacial stress or the particle cracking stress. In the overaged alloys, homogeneous deformation relaxes the local stress levels resulting in fewer voids/mm². Secondly, the overaged alloys exhibit a lower void growth rate due to reduced local deformation. Although void growth rates are

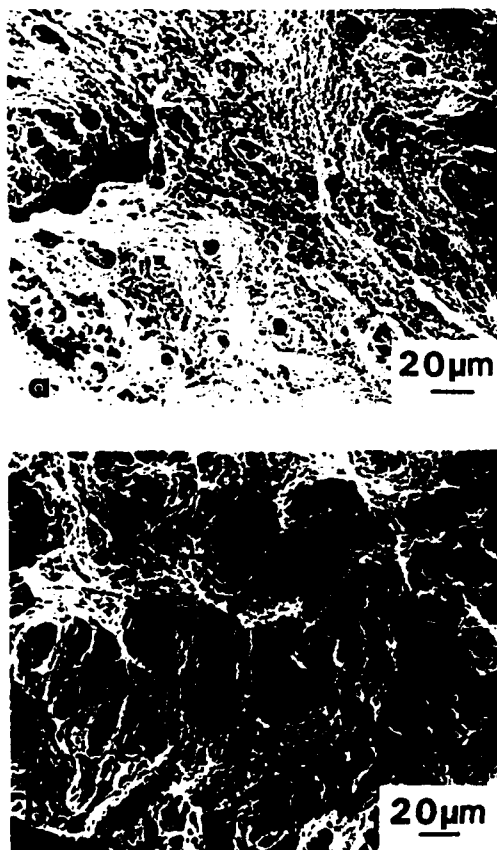


Fig. 13. Comparison of void size at fracture at (a) T_2 and (b) T_4 triaxialities for the 0.6% Mn alloy.

reduced in the overaged alloys, the general observation is that the terminal or final void size prior to fracture is larger than observed for the underaged alloys. Thus it appears that the final link-up of voids is an important factor that curtails ductility in underaged alloys. The curtailment in ductility usually occurs through shear localization or void sheet formation in between large voids. Some evidence of shear localization, i.e. brittle regions in addition to dimpled rupture can be observed in the underaged condition of the 0% Mn alloy. The brittle regions correspond to shear fracture that occurs in between voids when slip localization becomes extensive at high strain levels.

In the overaged condition, fracture due to strain localization in the precipitate free zone is evident and ductile shallow void growth is observed, which results in a higher critical void volume fraction in the overaged case. Such clear evidence of link-up of voids through shear localization in the underaged higher Mn-containing alloys could not be observed, partly due to the presence of submicrometer-sized dispersoids promoting void sheet formation. The ductile shallow voids were also not observed in the overaged alloys since the majority of the dispersoids and large constituent particles were present in the grain interiors. Thus these results suggest localized slip in the underaged condition, the degree of which varies the Mn content, curtails ductility due to an earlier link-up of voids. In the overaged condition, homogeneous slip in the grain interior enhances ductility; grain boundary particles and precipitate free zones do not play a major role in these 2134-type alloys.

The effect of increasing Mn content on ductility can be understood by recalling that Mn additions not only homogenize the deformation but also increase the volume fraction of large void nucleating particles and decrease their interparticle spacing. Thus there is a competition between the delaying of void link-up due to homogeneous deformation and the enhancement of void link-up due to a decrease in the interparticle spacing. The 1.02% Mn alloy has the lowest ductility despite a higher critical void volume fraction. The high volume fraction and small interparticle spacing of large particles results in rapid damage accumulation (as observed from the slope of the V_f vs strain curves) even though homogeneous deformation delays void link-up. The voids/mm² and void growth rate data also support this conclusion. The 0.31% Mn alloy, which exhibits the highest ductility, also shows a higher V_{fc} than either the 0.61 or 1.02% Mn alloys. The volume fraction and spacing of the large particles in the 0.31% Mn alloy are comparable to those of the 0.0% Mn alloy, but the Mn-dispersoids homogenize the strain enabling a delayed link-up of voids. Unlike the 1.02% Mn alloy, the 0.31% Mn alloy does not exhibit a high damage accumulation rate due to the difference in volume fraction and spacing of particles. This results in an increase in ductility compared with the other alloys. The 0.61%

Mn alloy shows a slightly lower V_{fc} than the 0.31% Mn alloy because of the smaller interparticle spacing, although there is no discernible difference in slip homogenization.

The results on smooth tensile specimens suggest that overaging increases the ductility. An opposite effect is observed in the presence of a notch. This result is consistent with the lower fracture toughness observed for the overaged alloys. As discussed before, a significant result of the present investigation is that the nucleation rate of voids remains unaltered with increasing triaxiality suggesting that the nucleation event in the present alloys is controlled by a strain criterion rather than a stress criterion. Thus the reduction in ductility with increasing triaxiality is attributed to an increased void growth rate and earlier link-up of voids through void sheet formation.

CONCLUSIONS

Ductile fracture in 2134-type aluminum alloys has been studied in under and overaged conditions for alloys containing 0, 0.31, 0.61 and 1.02% Mn. The ductility of smooth specimens in the overaged conditions was observed to be higher than for the underaged conditions. However, notched specimens exhibit lower ductility in the overaged condition consistent with fracture toughness results. In smooth specimens the critical void volume fraction, i.e. volume fraction of voids beneath the fracture surface, was always higher in the overaged case. The void volume fraction results, together with areal void density and void growth rate results, suggest that the curtailment in ductility in the underaged alloys is due to easier link-up of voids due to localized slip between voids. The enhancement in ductility in overaged alloys is due to a delay in link-up of the voids. The effect of Mn additions is to increase the void volume fraction, areal density of voids and also void growth rates. However, the critical void volume fraction, the critical number density of voids and the critical void size are larger for the highest Mn-containing alloy. These parameters are not always lowest for the lowest Mn alloy. The ability of Mn to homogenize deformation and raise the volume fraction of void nucleating particles produces competing effects which dictate the link-up process. It is clear from this investigation that triaxiality does not increase the void nucleation rate. However, the void growth rate and void link-up are substantially accelerated at high triaxiality levels resulting in low fracture strains.

Acknowledgements—This work was supported by AFOSR, under contract number AFOSR-83-0061. Dr. Alan Rosenstein, Program Manager.

REFERENCES

1. H. G. F. Wilsdorf, *Mater. Sci. Engng.* **59**, 1 (1983).
2. R. H. Van Stone, T. B. Cox, J. R. Low and J. A. Psioda, *Int. Metals Rev.* **30**, 157 (1985).

3. G. Le Roy, J. D. Embury, G. Edwards and M. F. Ashby, *Acta metall.* **29**, 1509 (1981).
4. S. H. Goods and L. M. Brown, *Acta metall.* **27**, 1 (1979).
5. J. W. Hancock and A. C. Mackenzie, *J. Mech. Phys. Solids* **24**, 147 (1976).
6. A. S. Argon, J. Im and R. Safoglu, *Metall. Trans.* **6A**, 825 (1975).
7. F. Yunchang and D. A. Koss, *Metall. Trans.* **16A**, 675 (1985).
8. M. A. Greenfield and H. Margolin, *Metall. Trans.* **3A**, 2649 (1972).
9. R. O. Ritchie, W. L. Server and R. A. Wullaert, *Metall. Trans.* **10A**, 1557 (1979).
10. M. G. Stout and W. W. Gerberich, *Metall. Trans.* **9A**, 649 (1978).
11. J. T. Staley, in *Properties Related to Fracture Toughness* (edited by W. R. Warke, V. Weiss and G. T. Hahn), ASTM STP 605, pp. 71-103 (1975).
12. R. H. Van Stone, R. H. Merchant and J. R. Low, in *Fatigue and Fracture Toughness Behavior—Cryogenic Behavior* (edited by C. F. Hickey and R. G. Broadwell, ASTM STP 556, pp. 93-179 (1973).
13. E. P. Butler, N. J. Owen and D. J. Field, *Mater. Sci. Technol.* **1**, 531 (1985).
14. W. X. Feng, F. S. Lin and E. A. Starke, *Metall. Trans.* **15A**, 1209 (1984).
15. C. Garrett and J. F. Knott, *Metall. Trans.* **9A**, 1187 (1978).
16. G. T. Hahn and A. R. Rosenfield, *Metall. Trans.* **6A**, 653 (1975).
17. K. V. Jata and E. A. Starke Jr, *Metall. Trans.* **17A**, 1011 (1986).
18. D. S. Thompson and S. A. Levy, in *Thermomechanical Processing of Aluminum Alloys* (edited by J. G. Morris), pp. 74-83. Am. Inst. Min. Engrs. New York (1979).
19. J. A. Walsh, M.S. thesis, University of Virginia, Va (1988).
20. P. W. Bridgeman, *Trans. Am. Soc. Metals* **32**, 553 (1944).
21. F. A. McClintok, in *Fracture* (edited by H. Liebowitz), Vol. 3, p. 106. Academic Press, New York (1971).
22. K. C. Prince and J. W. Martin, *Acta metall.* **27**, 1401 (1979).
23. J. M. Dowling and J. W. Martin, *Acta metall.* **24**, 1147 (1979).
24. A. K. Busby, L. Edwards and J. W. Martin, *Mater. Sci. Technol.* **2**, 363 (1986).

QUENCH SENSITIVITY OF THE Al-Li-Cu-Mg ALLOY 8090

G. N. Colvin and E. A. Starke, Jr.
*Department of Materials Science
University of Virginia
Charlottesville, Virginia 22901*



REPRINTED FROM THE SAMPE QUARTERLY, VOL. 19, NO. 4, JULY 1988
The Society For The Advancement of Material & Process Engineering
P. O. Box 2459, Covina, California 91722

QUENCH SENSITIVITY OF THE Al-Li-Cu-Mg ALLOY 8090

G. N. Colvin and E. A. Starke, Jr.
Department of Materials Science
University of Virginia
Charlottesville, Virginia 22901

ABSTRACT

Time-temperature-transformations diagrams were developed for precipitation of the equilibrium $T_2(Al_6CuLi_3)$ and $S(Al_2CuMg)$ phases in two compositional variations of the Al-Li-Cu-Mg alloy 8090. The start of T_2 nucleation proved to be relatively rapid in both alloy variants with T_2 nucleating in under five seconds at 400°C-450°C in the more heavily alloyed material. Nucleation of the T_2 phase was not evident in the lean alloy until after 20 seconds at these temperatures. The S phase nucleation appeared to be less sensitive to the composition range studied, with its earliest appearance being after ten seconds at 300°C. The volume fraction of T_2 correlated well with Charpy energy absorption values, with increasing amounts of T_2 leading to decreasing toughness. 8090, like many other Al-Li-X alloys, is quench sensitive, requiring fairly rapid cooling rates from the solutionizing temperature for mechanical property optimization.

1. INTRODUCTION

The primary purpose of quenching age-hardened aluminum alloys is to maintain a large degree of supersaturation of solute atoms homogeneously distributed in solid solution. This permits precipitation of an optimum concentration and distribution of hardening particles during the aging treatment. As quench rates decrease, more time is allowed for solute atoms to migrate to grain boundaries or precipitate as matrix phases. Grain boundaries act as heterogeneous nucleation sites by reducing the free energy barrier to nucleation.¹ When thermodynamic and kinetic demands are satisfied, precipitation can occur along the grain boundary and subsequently enhance intergranular cracking, grain boundary decohesion and premature material failure.²

It has been well established that deformation of Al-Li-X alloys occurs by planar slip due to the coherent nature of the primary strengthener: delta prime (Al_3Li).^{3,4} Planar slip concentrates stress at grain boundaries and may prematurely nucleate cracks and cause early failure. Failure may occur transgranularly along slip bands or intergranularly along grain boundaries. Grain boundary precipitates enhance void nucleation and accelerate intergranular fracture and are thus a very important contributor to the low resistance to fracture often

observed in Al-Li-X alloys.⁵ This paper describes the influence of quench rates on precipitation of the grain boundary phase $T_2(Al_6CuLi_3)$ and the equilibrium phase $S(Al_2CuMg)$ that form in the Al-Li-Cu-Mg alloy 8090 and their subsequent effects on the alloy's fracture behavior.

2. PROCEDURES

Preliminary Experiments

The material used in this study was obtained from Alcan International Limited as two 2.54 cm thick plates in the T3 temper. One plate had a "rich" composition and one a "lean" composition but both were within the limits of alloy 8090, Table 1.

Blocks 7.6 cm x 7.6 cm x 2.54 cm were sectioned from each alloy with two holes drilled such that the temperatures of the outside surface and the interior could be measured. K-type thermocouples were inserted into each hole, assuring good thermal contact, and then were cemented into place using a high temperature ceramic. Each slab was solution heat treated at 550°C for one hour then cooled via one of three mediums: room temperature water, pure glycol polymer quenchant, or air. An oscilloscope was employed to measure and record the cooling response of each of the thermocouples. Samples of both compositions from the water quenched, polymer quenched, and still-air quenched materials were mounted

REFERENCE: Colvin, G. N. and Starke, E. A., Jr.,
Quench Sensitivity of the Al-Li-Cu-Mg Alloy 8090, *SAMPE Quarterly*, Volume 19, No. 4, July 1988, pp 10-21.

TABLE 1
COMPOSITION OF THE VARIANTS OF 8090

Alloy Des.	Li	Cu	Mg	Zr	Fe	Si	Al
Rich	2.58	1.36	0.89	0.13	0.17	0.04	bal
Lean	2.28	0.86	0.90	0.13	0.13	0.06	bal

using a hardener/resin epoxy system. They were hand-ground flat to 600 grit paper and polished through colloidal silica using conventional techniques. The specimens were etched with water-0.25HF for 5 seconds to darken the secondary phases and examined using an oil immersion lens at a magnification of 1250X.

Eight round tensile specimens with 2.8 cm gauge lengths and 0.6 cm gauge diameters were machined from each quenched block with the gauge length of the bars machined parallel to the rolling direction of the plate. Four of the eight tensile specimens were tested in the as-quenched condition. The remaining tensile specimens were stretched and aged with one of two treatments which were reported to produce peak strenghts in 8090⁶: 2% stretch + 190°C/16 hours or 4% stretch + 170°C/24 hours. Two tensile specimens from each composition/quench and aged condition were tested.

Two standard size Charpy specimens were machined from each quench condition with a V-notch in the rolling direction of the plate. These were tested by the three-point bend method employing a slow strain rate to minimize variability in the data. Energy values measured on charpy specimens are expressed as W/A values where W=energy absorbed and A=net (unnotched) section area. The energy absorbed was approximated by the area under the load/displacement curve. W/A values can be used to obtain a relative ranking of fracture resistance for a given set of specimens provided that parameters remain constant through the experiments.⁷

Determination of TTT Diagrams

Specimens 7.6 cm x 2.54 cm x 0.4 cm were sectioned from each plate such that the plate's rolling direction was perpendicular to the plane of the sample. The samples were ground to a thickness of 0.3 cm in order to minimize the time required for the specimen to come to temperature when immersed in a salt bath.⁸ The specimens were solutionized in a salt bath at 550°C for one hour, immersed into an adjacent salt bath for the appropriate isothermal hold temperature and time, then quenched into an ice-brine solution.

Optical microscopy was used as a rapid means of determining the effect of time at temperature on the microstructure of each composition. Sections were cut from each of the heat treated specimens then mounted and polished using the technique described previously. The Guinier x-ray diffraction method was used to precisely determine the phases present for each time/temperature

condition. Specimens were cut to 0.05 cm thick using a slow speed diamond saw and then ground to remove the deformation associated with sawing. The foils were irradiated in an evacuated Guinier camera for 100 hours using Cu K-Alpha radiation. Phase identifications were made by measuring the d-spacings of the diffraction lines and comparing these to powder diffraction card files. Transmission electron microscopy (TEM) was also utilized to confirm the presence of the various phases identified by x-ray diffraction.

Samples were prepared for scanning electron microscopy (SEM) examination by etching with boiling 9:1 methanol:bromine solution which selectively removes the aluminum matrix leaving the precipitated particles in relief. Optimum etching time varied from 30 seconds to 1 minute. The volume percent of secondary phases was measured using a quantitative analysis program in conjunction with an SEM. This analysis was typically performed between 1000-5000X magnification depending upon the precipitate size and distribution. In samples where both T₂ and S phases were present the separate volume fraction of each phase was obtained. The T₂ and S phases were identified through EDAX and their volume fractions were determined and separated by the quantitative metallography program which used their respective characteristic reflectivities.

The small sample size necessary for isothermal treatment prohibited K_{IC} determination as a function of time at temperature. Consequently, the fracture characteristics of the two alloys were evaluated using three-point slow bend Charpy tests. One primary difficulty with this technique is that the relatively blunt notch radius of the standard V-notch Charpy specimen can postpone the onset of crack extension to higher apparent toughness values. This permits general yielding to occur prior to fracture.⁷ To minimize this effect the V-notch radius was machined as sharp as possible using a specially ground carbide tool with a radius of less than 0.0025 cm.

Two Charpy specimens were machined from the isothermally heat treated specimens for the conditions listed in Table 2. Due to the necessary thinness of the plates (0.3 cm) the thickness of the Charpy specimens did not meet ASTM standards. A 0.05 cm deep V-notch was machined parallel to the rolling direction of the as-received plate material. A MTS servohydraulic tensile testing machine was used with a three point bend apparatus to obtain load versus strain curves. The bend apparatus was set up with frictionless rollers and alignment according to ASTM E812-81 requirements.⁹

3. RESULTS AND DISCUSSION

Preliminary Experiments

Cooling curves for each composition and quench method are shown in Figures 1 and 2. Water quenching resulted in cooling rates of approximately 150°C/sec, the polymer quench a cooling rate of approximately 9°C/second and the

TABLE 2
TENSILE DATA FOR AS-QUENCHED
AND AGED CONDITIONS

COMPOSITION	COOLING	AGING TREATMENT	UTS (MPa)	YS (MPa)	ELONG (%)
Al-2.28Li-0.86Cu -0.90Mg-0.13Zr	AIR COOL	no age	414	237	10
		2 $\frac{1}{2}$ 190°C/16h	449	401	8
		4 $\frac{1}{2}$ 170°C/24h	465	401	6
	POLYMER QUENCH	no age	393	229	17
		2 $\frac{1}{2}$ 190°C/16h	481	415	8
		4 $\frac{1}{2}$ 170°C/24h	481	415	7
Al-2.58Li-1.36Cu -0.89Mg-0.13Zr	WATER QUENCH	no age	374	208	18
		2 $\frac{1}{2}$ 190°C/16h	492	428	8
		4 $\frac{1}{2}$ 170°C/24h	483	417	8
	AIR COOL	no age	456	288	6
		2 $\frac{1}{2}$ 190°C/16h	485	417	6
		4 $\frac{1}{2}$ 170°C/24h	503	441	5
	POLYMER QUENCH	no age	450	284	11
		2 $\frac{1}{2}$ 190°C/16h	524	450	7
		4 $\frac{1}{2}$ 170°C/24h	519	451	5
	WATER QUENCH	no age	425	264	16
		2 $\frac{1}{2}$ 190°C/16h	535	464	8
		4 $\frac{1}{2}$ 170°C/24h	517	448	7

air quench a cooling rate of approximately 0.2°C/sec for the sample size used. Water quenching cooled the centerline of the blocks to below 200°C in under 3.5 seconds. The cooling response produced by water quenching resembles results determined by several researchers on water quenching of aluminum alloys, verifying the accuracy of the experimental setup employed in these investigations.^{10,11} Polymer quenching cooled the specimen to 250°C in 10 seconds; however, the cooling rate decreased in the region from 250°C to 200°C. This is a characteristic of polymer quenches which are designed to reduce the degree of distortion during quenching.¹¹

Large Fe and Si-rich phases, that form during solidification and thus are present in the as-received material, were the only precipitates observed optically in material that was water quenched; however, light gray, matrix and grain boundary precipitates were evident in the slower cooled material, illustrating the quench sensitivity of the 8090 alloy, Figure 1. Cooling at 150°C/sec (water quench) and 9°C/sec (polymer quench) appeared successful in minimizing precipitation in the lean composition, Figure 1; however, the slow cooling rate of the air quench (0.2°C/sec) permitted both grain boundary and matrix precipitation. In the rich alloy only 150°C/sec (water quench) was sufficient to prevent such precipitation, Figure 2. These results illustrate the significant influence that minor variations in composition have on the quench sensitivity of 8090.

Results of the tensile tests for the as-quenched specimens are listed in Table 2. As expected, the rich composition produced higher strengths than measured for the lean alloy. This difference is associated more with Al₃Li precipitation than with precipitation of T₂ and S. It

is difficult to suppress Al₃Li precipitation in any Al-Li alloy containing more than 1 wt% lithium. The higher lithium content of the rich composition promoted a greater volume fraction of the Al₃Li strengthening phase. Slower cooling rates produced greater as-quenched strengths in both materials since more time was available at intermediate temperatures for the precipitation of other hardening phases such as S'.

Results for the aged tensile specimens are also listed in Table 2. The rich composition consistently exhibited ultimate and yield strengths superior to those produced by the lean alloy. The rich alloy's higher lithium and copper contents promoted precipitation of higher volume fractions of hardening phases during aging. In contrast to the as-quenched results the fastest cooling rates (water quenching) promoted the greatest strengths for the aged specimens. The faster cooling rates quenched in more solute which was then available to form strengthening precipitates during aging.

Charpy energy absorption values are shown in Figure 3. As quench rates increased, the energy absorbed or resistance to crack propagation improved for both compositions. This is primarily due to the greater success in suppressing grain boundary precipitation by the faster quenching methods. For both alloys, cooling at 150°C/sec. (water quench) produced the greatest resistance to crack propagation, and 0.2°C/sec (air cool) promoted the least resistance to crack propagation. However, a quench rate of 9°C/sec (polymer quench) was more successful in maintaining fracture resistance in the lean alloy than occurred for the rich alloy. This is evidence that a critical cooling rate must be achieved to effectively suppress precipitation during the quench in order to optimize mechanical properties and illustrates that lean alloys

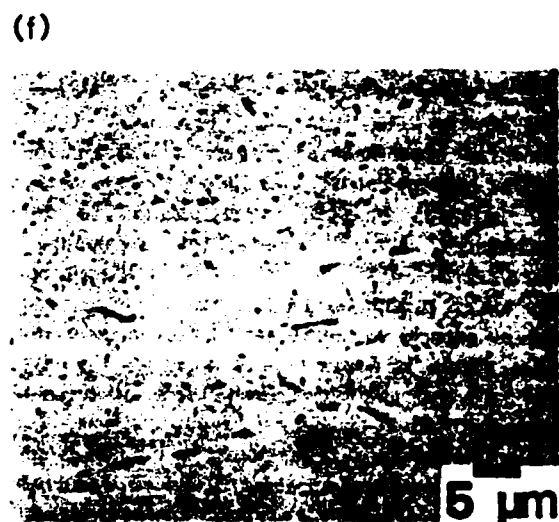
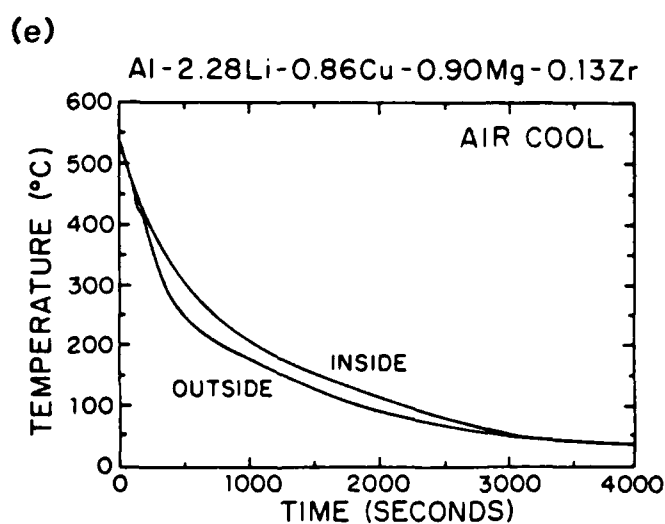
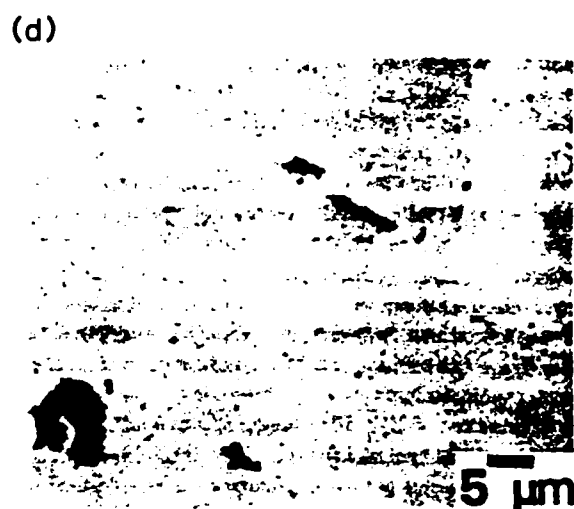
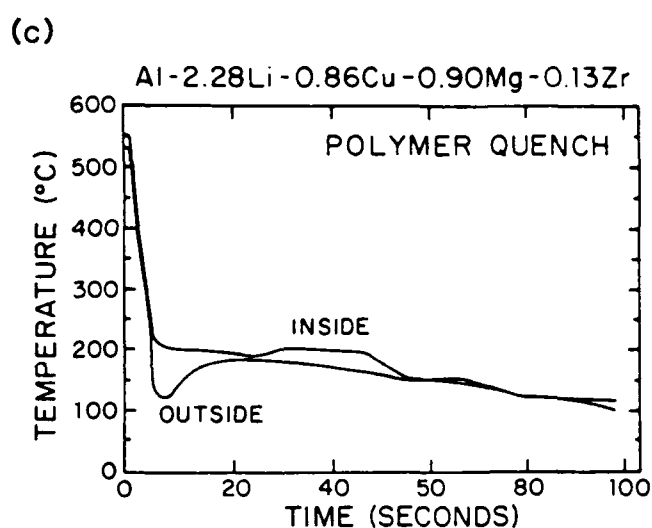
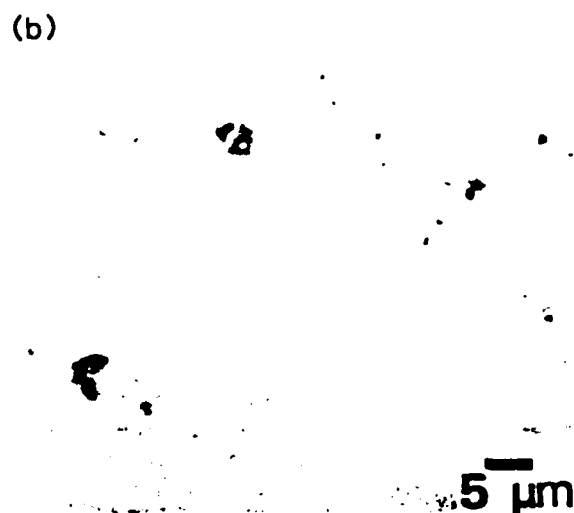
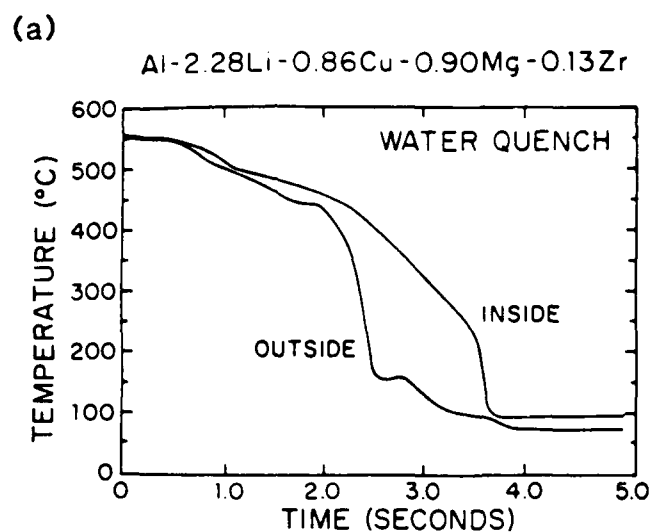


Figure 1. Cooling Curves and Associated RT Microstructures for the Lean 8090 Alloy. [a-b] 150°C/Sec; [c-d] 9°C/Sec; [e-f] 0.2°C/Sec.

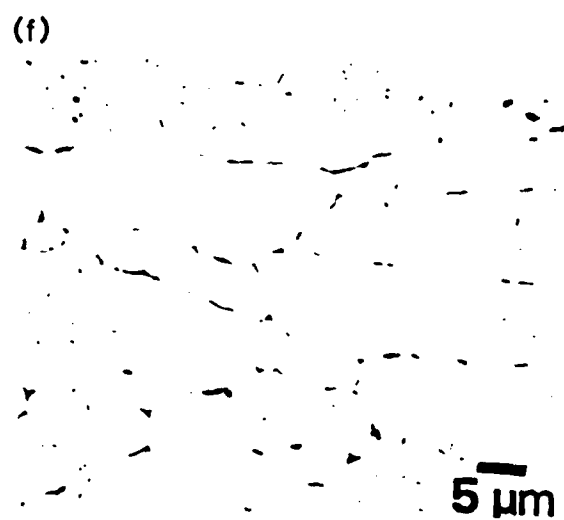
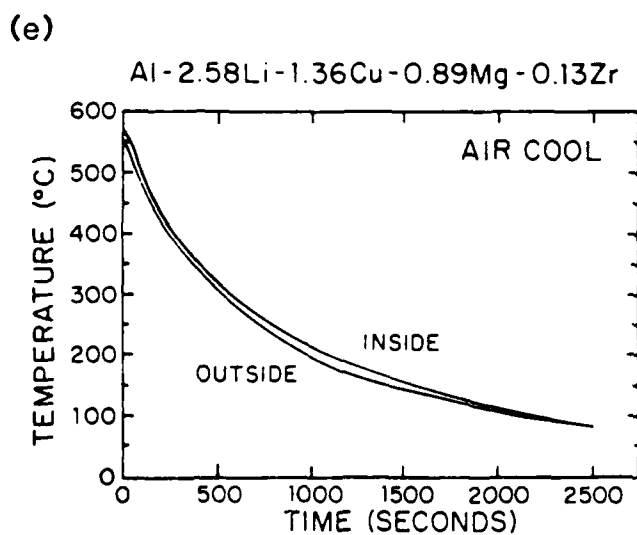
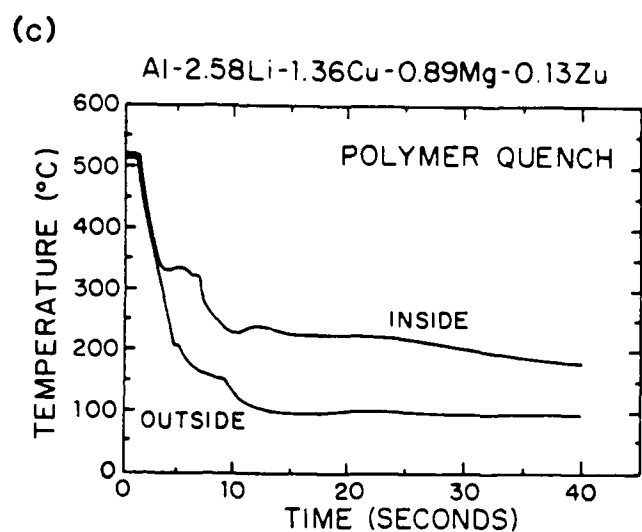
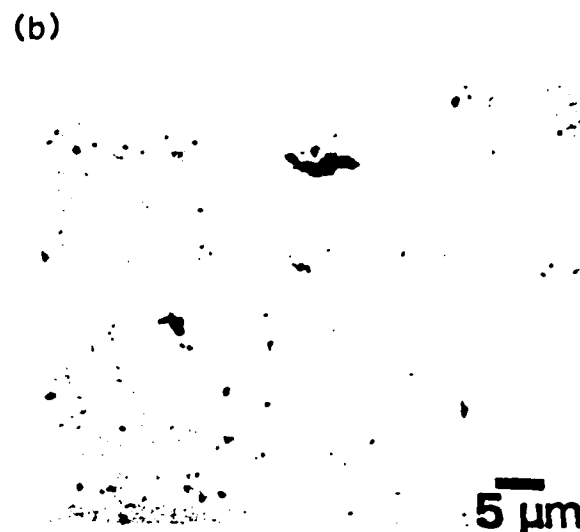
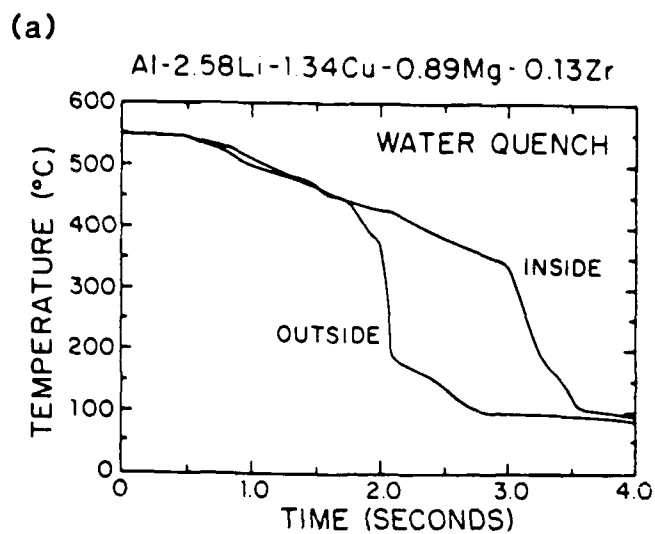


Figure 2. Cooling Curves and Associated RT Microstructures for the Rich 8090 Alloy. [a-b] 150°C/Sec; [c-d] 9°C/Sec; [e-f] 0.2°C/Sec.

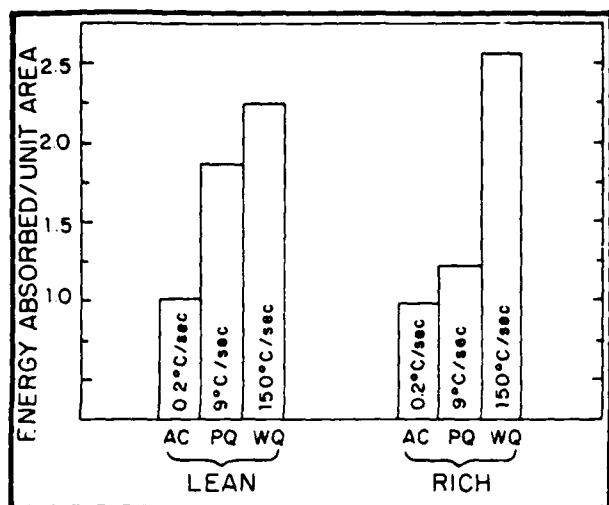


Figure 3. Normalized Charpy Energy Absorption Values Showing Drop in Fracture Resistance with Decreasing Quench Rates.

should be selected for thick plate or heavy sections.

Determination of TTT Diagrams

Optical microscopy was used in conjunction with x-ray diffraction and transmission electron microscopy to determine, quantitatively, the volume fraction of phases present after various thermal treatments. This data was used to plot time-temperature-transformation (TTT) diagrams. Representative optical micrographs of the rich and lean alloys showing both matrix and grain boundary precipitates are given in Figure 4. These precipitates were identified by x-ray analysis as T_2 and S. The T_2 phase heterogeneously nucleates at grain boundaries in Al-Li-Cu Alloys.¹² It is a member of a group of quasi-crystals which have been under intense study during the past several years¹³ and is believed to possess an icosahedral structure with 5-fold diffraction symmetry. The S phase is present in many commercial Al-Cu-Mg alloys.

The phase boundaries for the start of T_2 and S nucleation, as determined in this study, are shown in Figures 5 and 6. The T_2 phase precipitated at 400°C-450°C after only 5 seconds in the rich alloy. The relatively rapid precipitation of T_2 is an indication of a low free energy barrier ΔG^* to nucleation. T_2 heterogeneously nucleates on high angle grain boundaries—an imperfection which reduces ΔG^* by providing a portion of the interfacial energy needed to accomplish the nucleation process.¹

The TTT curve for T_2 for the lean composition alloy was shifted to longer hold times (nucleation of the T_2 phase was not apparent until approximately 20 seconds at 400°C-450°C); however, the curve exhibited the same general shape as that of the rich alloy. The lean alloy's lower

lithium and copper contents decrease ΔG_v the volume free energy change since ΔG_v is proportional to the concentration of solute.¹ Consequently, the driving force for nucleation is decreased, and precipitation is delayed.

It was more difficult to establish phase boundaries for S nucleation. Guinier diffraction identified S at longer hold times (300°C/1000 sec); however, at shorter times where optical metallography showed precipitation, Guinier diffraction analysis was inconclusive in identifying the presence of S. At these lower volume fractions TEM was used to positively identify S. Phase boundaries for S proved to be very similar for both compositions with Al_2CuMg nucleating within 10 seconds at 300°C-350°C. Apparently the increased copper content of the rich alloy did not significantly reduce the free energy barrier for nucleation of S. The magnesium content, which was the same for both alloys, most probably controls the nucleation rate for this precipitate for the compositional range studied.

A typical microstructure as revealed by etching with the bromine:methanol solution is shown in Figure 7. Quantitative analysis verified that T_2 volume fractions increased during the isothermal heat treatments. The T_2 volume fraction in the rich alloy was almost double that for the lean material after 450°C/1000 sec, Figure 8. The T_2 volume fractions were greatest for both alloys at temperatures higher than the nose of the TTT curve. This may be due to the competition in nucleation and growth between the S and T_2 phases at intermediate temperatures. If the growth of S ties up a significant fraction of the copper solute, then growth of T_2 may be decreased at these temperatures. The volume fraction of S increased during the isothermal hold with the greatest percentages of S occurring at 350°C for both compositions, Figure 8. The rich alloy had volume fractions of both T_2 and S substantially greater than those for the lean composition.

Results of the Charpy tests are listed in Table 3. A decrease in the Charpy energy absorbed (area under the load/deformation curve) was observed after only 5 seconds at 450°C-400°C for the rich alloy. This is an indication of a loss in resistance to crack propagation and correlates well with the optical microscopy and Guinier diffraction analysis which indicated T_2 precipitation within 5 seconds at these temperatures, Figure 9. Charpy values, after holding 2 seconds at 450°C-400°C, were the same as the water quenched results, indicating that significant nucleation/growth of T_2 occurred during the time interval of 2-5 seconds. Energy absorption values continued to decrease to hold times of 100 sec., after which an increase was observed for times up to 1000 sec. The T_2 phase controls the fracture behavior from 0 to 100 seconds by promoting cracks along grain boundaries and reducing fracture toughness. At longer hold times S co-precipitates in the matrix and along subgrain boundaries. The S precipitates homogenize slip in the matrix as dislocations bypass or loop around these particles. This reduces the stress at the grain boundaries, which in turn reduces the deleterious effect of T_2 precipitation. The result is an

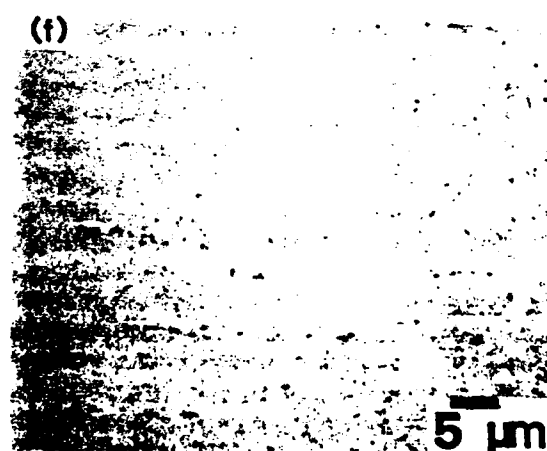
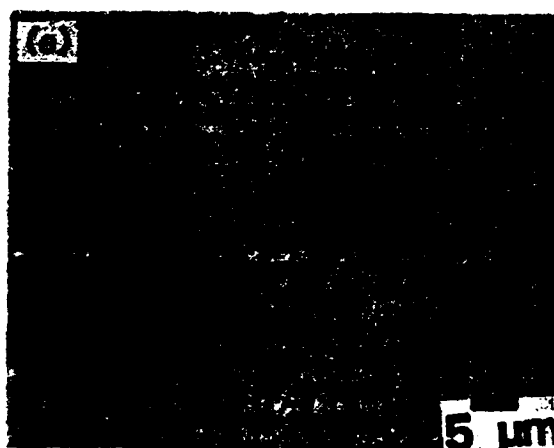
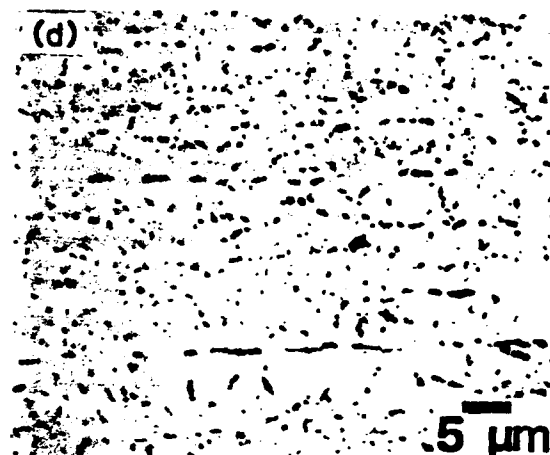
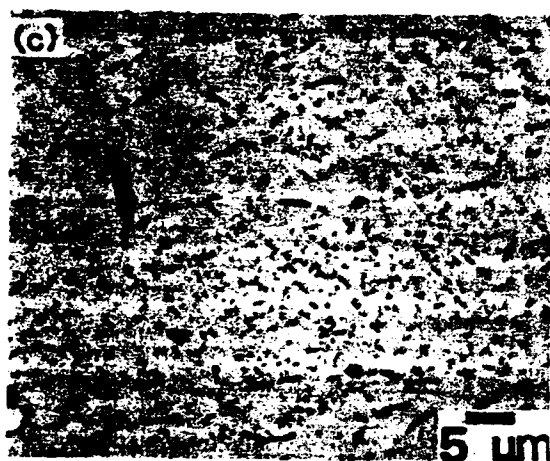
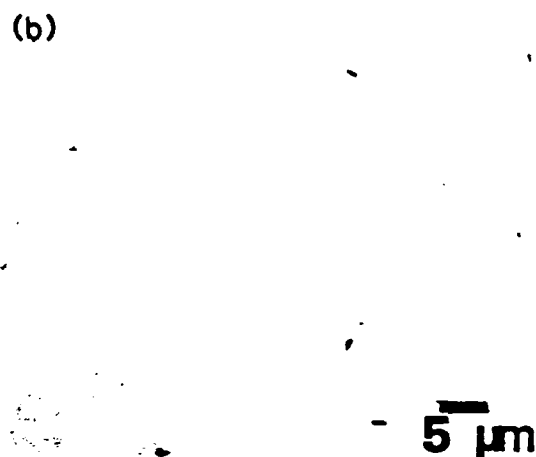
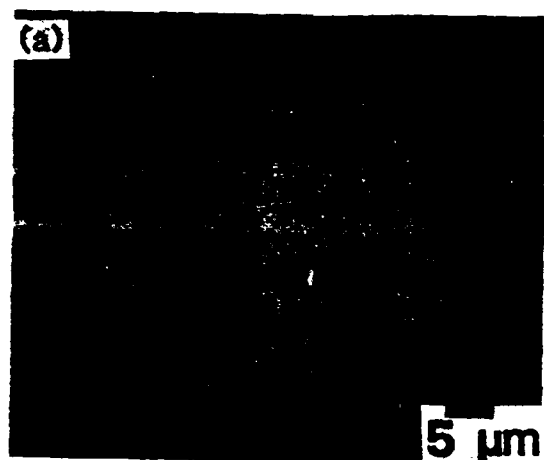


Figure 4. Optical Micrographs of the Rich and Lean 8090 Alloys After 1000 Sec at Various Temperatures; a, c, e, Rich Alloy at 500°, 400° and 300°C, and b, d, f, Lean Alloy at 500°, 400° and 300°C, Respectively.

TABLE 3
CHARPY ENERGY ABSORPTION DATA

COMPOSITION	ISOTHERMAL TEMP.	HOLD TIME(sec.)					
		2	5	10	20	100	1000
AL-2.58Li-1.36Cu -0.9Mg-0.13Zr	525°C	-	-	-	-	-	4.00
	500°C	-	-	4.65	-	4.05	2.33
	450°C	4.55	3.25	2.30	-	1.37	2.31
	400°C	4.25	3.13	1.60	-	1.35	2.30
	350°C	-	-	3.25	-	2.00	2.20
	300°C	-	-	4.45	-	0.91	1.63
	250°C	-	-	4.40	-	1.21	0.63
	200°C	-	-	-	-	-	0.33
	Water Quench	-	-	-	-	-	4.45
Al-2.28Li-0.86Cu -0.9Mg-0.13Zr	525°C	-	-	-	-	-	4.10
	500°C	-	-	4.58	-	3.51	3.42
	450°C	-	-	4.81	3.92	2.60	3.11
	400°C	-	-	4.84	2.50	2.74	4.31
	350°C	-	-	4.90	-	2.00	2.72
	300°C	-	-	4.77	-	1.93	1.86
	250°C	-	-	4.76	-	2.41	1.65
	200°C	-	-	-	-	-	1.01
	Water Quench	-	-	-	-	-	4.85

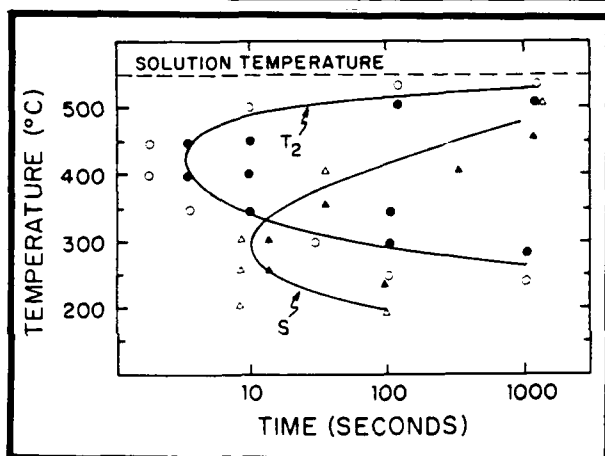


Figure 5. Nucleation Start Curves for T₂ [Al₆CuLi₃] and S [Al₂CuMg] for the Rich 8090 Alloy.

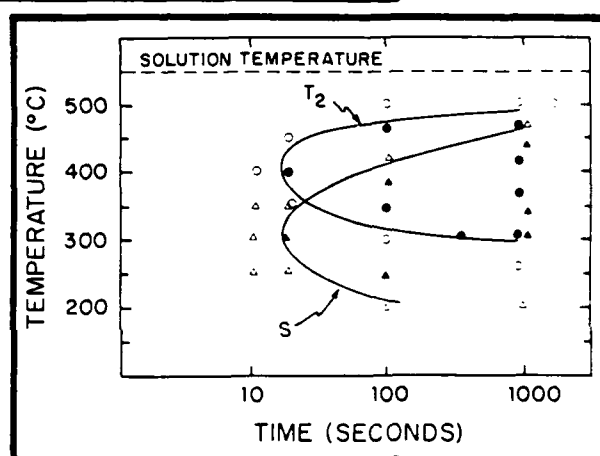


Figure 6. Nucleation Start Curves for T₂ [Al₆CuLi₃] and S [Al₂CuMg] for the Lean 8090 Alloy.



Figure 7. SEM of the 8090 Alloy After Etching With Boiling 1:9 Bromine: Methanol Solution Showing the T₂ and S Precipitates.

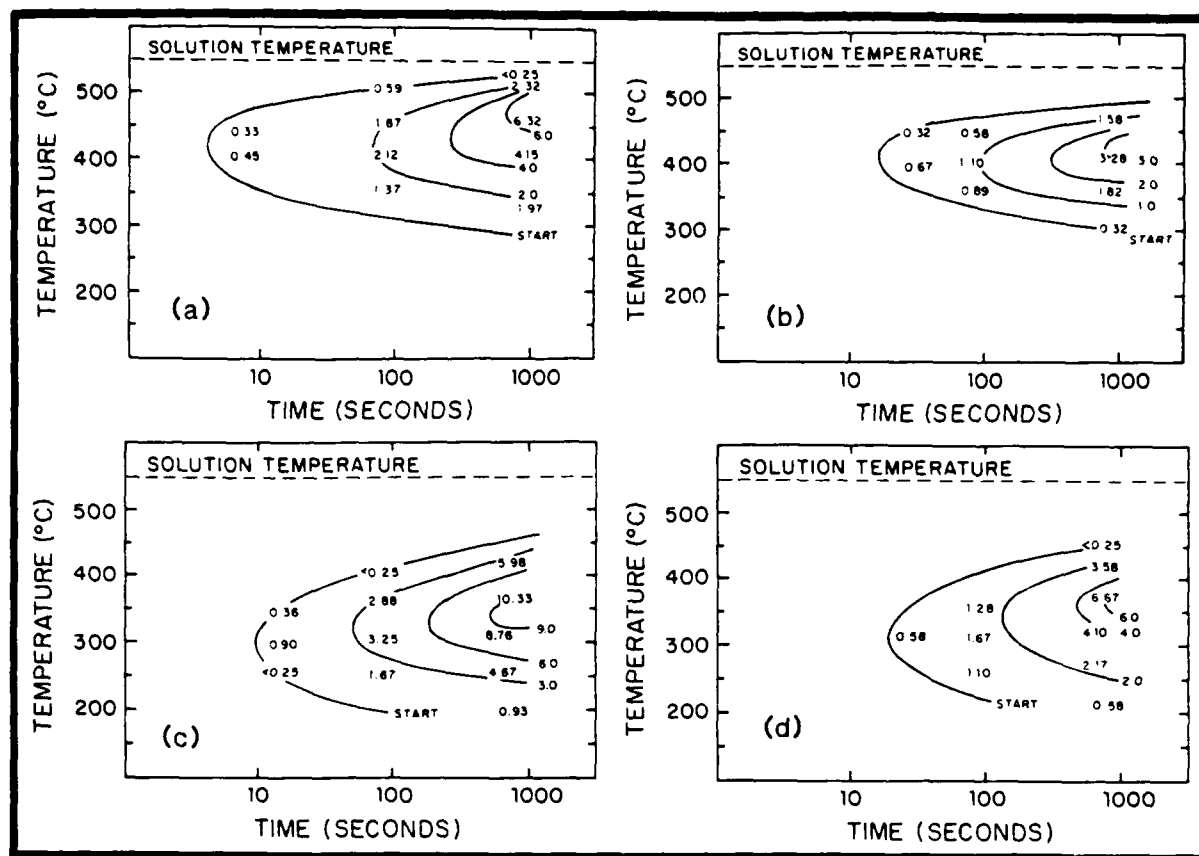


Figure 8. Time-Temperature-Transformation Curves Showing Volume Percents of the T_2 and S Phases. [a] T_2 for the Rich Alloy; [b] T_2 for the Lean Alloy; [c] S for the Rich Alloy and [d] S for the Lean Alloy.

increase in fracture resistance as isothermal hold times increase from 100 to 1000 seconds. The effect of slip homogenization on decreasing the deleterious effect of grain boundary precipitation in Al-Li alloys has been described by Cassada et al.¹⁴

After 10 seconds at isothermal hold temperatures of 450°C - 300°C, no significant decrease in Charpy energy absorption was observed for the lean alloy. This indicates that precipitation of secondary phases does not occur in this alloy until after 10 seconds, which is consistent with metallographic observations. The pattern of initial loss of fracture toughness (caused by growth of T_2) followed by increasing fracture toughness (promoted by S precipitation) was duplicated with the lean alloy.

The fracture mode of the Charpy specimens was predominantly intergranular following treatments at higher temperature (450°C - 400°C) and shorter hold times (<100 seconds). The percentage of intergranular fracture increased with increasing hold times up to 100 seconds, Figure 10. This evolution in fracture mode corresponds to growth of T_2 along high angle grain boundaries. Stable T_2 particles nucleated cracks along grain boundaries resulting in marked reductions in fracture resistance. Cross sections through the fracture surface show the crack path preferentially following high angle grain boundaries. The

jagged morphology of the primary crack is apparent as are secondary cracks at right angles to the primary crack which corresponds to delamination along the high angle boundaries.

As hold times at 400°C increased from 100 seconds to 1000 seconds, a change in fracture mode occurred. Dimpled transgranular fracture surfaces, evidence of microvoid growth and coalescence, were apparent in samples held for 1000 seconds at 400°C - 350°C for both compositions, Figure 10. Apparently the growth of S during this time interval resulted in increased homogenization of slip, reducing the stress concentrated at the grain boundaries but enhancing void nucleation and growth at the matrix/precipitate interface. The size of the dimples observed after 1000 seconds decreased as the temperatures decreased relating directly to the size of the S phase. This higher energy fracture mode improved the fracture toughness. These results illustrate the importance of minimizing strain localization as a method of improving the fracture toughness in alloys containing a significant amount of grain boundary precipitates.

The results of this study demonstrate a good correspondence between loss of fracture resistance and an increase in volume fraction and growth of T_2 and S. The most rapid loss in fracture resistance for both alloys

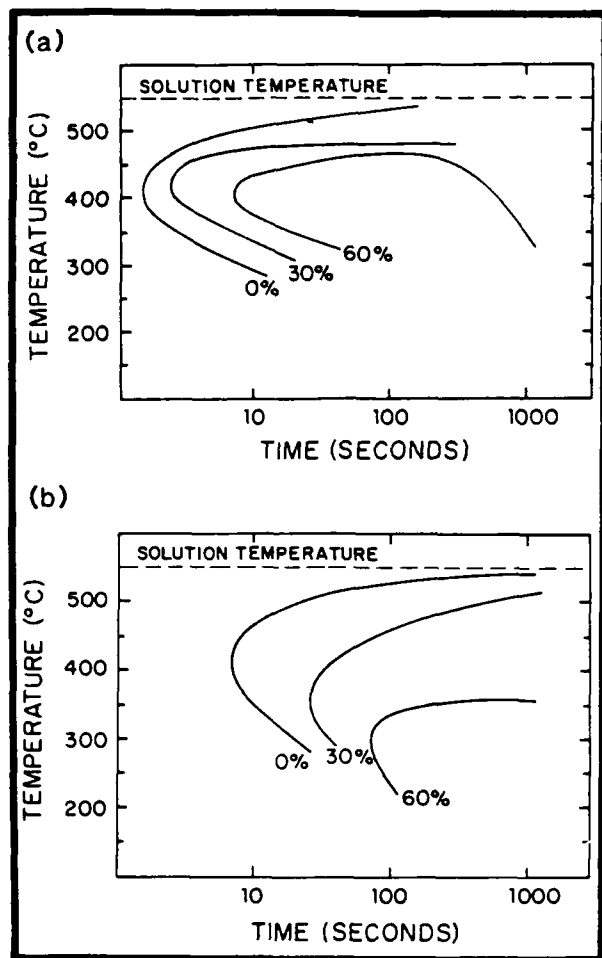


Figure 9. Iso Mechanical Lines Showing the Percent Loss of Charpy Energy Values as a Function of Time at Various Temperatures, [a] Rich 8090 Alloy and [b] Lean 8090 Alloy.

occurred at higher temperatures (400°C - 450°C) where T_2 was the dominant precipitate. However, large decreases in properties also occurred in the temperature range of 300°C - 250°C where the S phase dominated. Obviously, the S phase has both beneficial and deleterious effects. Depending on its size and spacing it can homogenize slip to reduce the adverse effect of large T_2 grain boundary precipitates. However, since the precipitate is not sheared by dislocations, voids can nucleate at the matrix/particle interface. As the spacing between particles decreases (which occurs as the temperature is reduced) void coalescence is enhanced and the fracture resistance decreases. The rapid precipitation of T_2 for the composition variations of 8090 is an indication of the relative quench sensitive nature of the alloy. Al-2.58Li-1.36Cu-0.86Mg-0.13Zr requires a cooling rate greater than 30°C/sec from 550°C - 250°C to bypass the nose of the T_2 and S C-curves and avoid nucleation of these equilibrium phases. Al-2.28Li-0.86Cu-0.90Mg-0.13Zr requires a quench rate 13°C/sec through the same temperature range to avoid T_2 and S precipitation and thereby optimize

mechanical properties. In an industrial environment where conditions are not ideal, a large 8090 plate could easily be subjected to quench rates slower than those required for suppressing formation of T_2 and S, resulting in lower mechanical properties. Consequently, post-quenching aging treatments must be designed to minimize the adverse effect of the grain boundary precipitates.

4. CONCLUSIONS

The rate of quenching after solution treatment does influence the mechanical properties of 8090. A cooling rate of $150^{\circ}\text{C/second}$ was sufficient to suppress deleterious nucleation of T_2 and S phases for the compositional variants studied. A cooling rate of 9°C/second was adequate to suppress precipitation in the lean alloy, but was not sufficient for the rich alloy. This was reflected by a lower resistance to fracture for the slower cooling rates.

The more heavily alloyed composition, Al-2.58Li-1.36Cu-0.9Mg-0.13Zr, exhibited a greater sensitivity to quenching rates than did Al-2.28Li-0.86Cu-0.9Mg-0.13Zr. This is due to the more rapid nucleation of T_2 in the rich alloy. The T_2 phase formed after 5 seconds at 400°C - 450°C in the rich alloy; however, T_2 was not evident until after 20 seconds in the less heavily alloyed composition. The S phase formed after 10 seconds at 300°C - 350°C in both alloys. Apparently S nucleation is insensitive to the lithium and copper difference between the alloy variants. The magnesium content, which is identical in both variants, may be the rate limiting solute addition.

A decrease of fracture resistance correlates well with the growth of T_2 precipitates indicating that T_2 is the principal cause of the loss of mechanical properties in 8090 following high temperature heat treatments. Increases in energy absorption values after longer hold times ($400^{\circ}\text{C}/1000\text{ sec}$) occurred due to precipitation of S. The S phase homogenized slip relieving some of the detrimental influence of T_2 on grain boundary fracture.

Al-2.58Li-1.36Cu-0.86Mg-0.13Zr requires a cooling rate greater than 30°C/sec from 550°C to 250°C to suppress nucleation of equilibrium T_2 and S phases. Al-2.28Li-0.86Cu-0.86Cu-0.90Mg-0.13Zr requires a cooling rate greater than 13°C/sec through the same temperature range for mechanical property optimization. The rapid precipitation of T_2 indicates that 8090 is relatively quench sensitive; however, T_2 can be suppressed if the above cooling rates are achieved.

Acknowledgements

One of us (GNC) would like to acknowledge financial support from a fellowship funded by Howmet Turbine Components Corporation. This research was sponsored by the Air Force Office of Scientific Research, United States Air Force Systems Command, under Grant AFOSR-87-0082, Dr. Alan Rosenstein, program manager. The authors

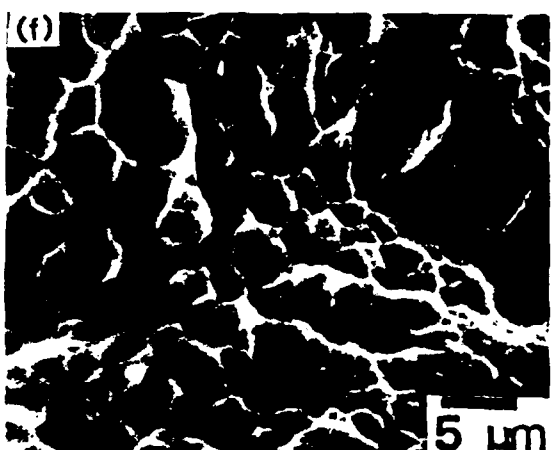
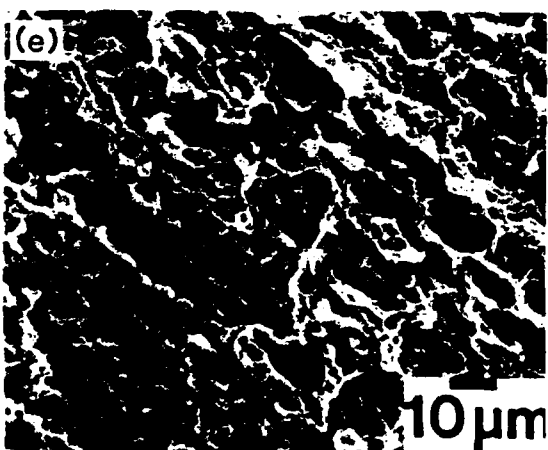
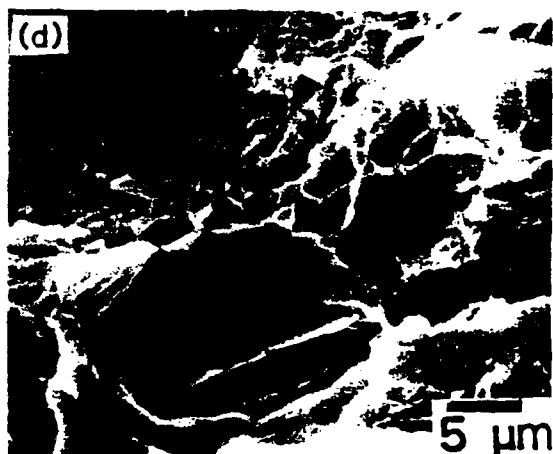
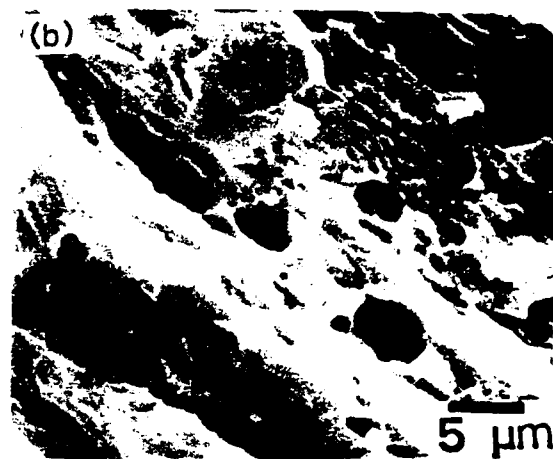
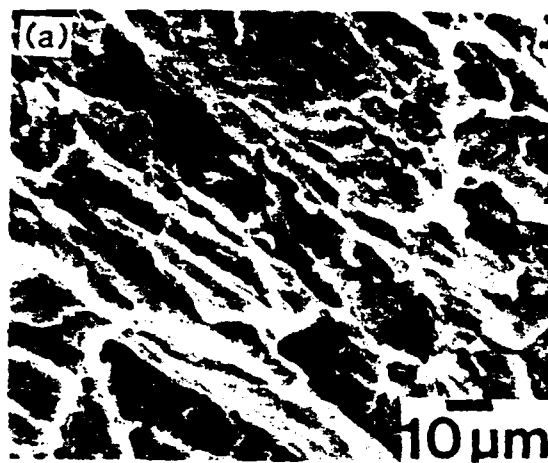


Figure 10. Representative SEM's of Fracture Surfaces of the Rich and Lean Alloys After Various Times at 400°C. [a-b] 10 sec, [c-d] 100 sec, and [e-f] 1000 sec.

would like to thank Drs. W. Ruch, K. Jata, T. Ahrens and J. T. Staley for helpful discussions during the course of this investigation.

REFERENCES

1. J. W. Christian, *The Theory of Transformations in Metals and Alloys*, First Edition, Pergamon Press, Oxford, England (1965).
2. R. F. Ashton, D. S. Thompson, E. A. Starke, Jr., and F. S. Lin, in *Aluminum-Lithium Alloys III*, eds. C. Baker, P. J. Gregson, S. J. Harris and C. J. Peel, The Institute of Metals, London (1986), p. 66.
3. T. H. Sanders, Jr. and E. A. Starke, Jr., *Acta Met.*, Vol. 30 (1982), p. 927.
4. K. V. Jata and E. A. Starke, Jr., *Met. Trans. A*, Vol. 17A (1986), p. 1011.
5. E. A. Starke, Jr. and F. S. Lin, *Met. Trans. A*, Vol. 13A (1982), p. 2259.
6. William Miller, Alcan Banbury Laboratory, United Kingdom, Private Communication, January, 1987.
7. Rapid Inexpensive Tests for Determining Fracture Toughness, National Materials Advisory Board, Washington, D. C. (1976).
8. J. T. Staley, Alcoa Technical Center, Alcoa Center, Pa, Private Communication, September, 1986.
9. *Slow-Bend Notched Bar Testing of Metallic Materials*, American Society for Testing Materials ASTM E812-81, Philadelphia, Pa. (1981).
10. C. E. Bates, T. Landig, G. Seitanakis, *Quench Factor Analysis: A Powerful Tool Comes of Age*, Park Chemical Company Technical Publication (June, 1986), p. 4.
11. T. Croucher and D. Butler, "Polymer Quenching of Aluminum Castings," in the Proceedings of the 26th National SAMPE Symposium (April, 1981), p. 530.
12. W. A. Cassada, G. J. Shiflet and E. A. Starke, Jr., *Scripta Met.*, Vol. 20 (1986), p. 751.
13. B. Dubost, M. Audier, P. Jeanmart, J. M. Lang, and P. Sainfort, in *Aluminum-Lithium IV*, eds. G. Champier, B. Dubost, M. Miannay, L. Sabetay, *Journal de Physique*, C3, (1987) p. 497.
14. W. A. Cassada, G. J. Shiflet, and E. A. Starke, Jr., *Acta Met.*, Vol. 34 (1986), p. 367.

INTERGRANULAR FRACTURE OF AN Al-Li-Cu-Mg ALLOY AS A RESULT OF
NONEQUILIBRIUM EUTECTIC MELTING DURING SOLUTION TREATMENT

P. Bourgasser⁺, J.A. Wert and E.A. Starke, Jr.

Department of Materials Science
Thornton Hall
University of Virginia
Charlottesville, VA 22901
USA

⁺ Present Address

Maubeuge Construction Automobile
Avenue Andre Chausson
59600 MAUBEUGE
France

ABSTRACT

This investigation has examined intergranular fracture during heat treatment and deformation of an Al-Li-Cu-Mg alloy and an Al-Li-Cu alloy. When solution treatment of the Al-Li-Cu-Mg alloy is begun by rapid heating to temperatures of 545°C or above, nonequilibrium eutectic melting of a grain boundary precipitate phase occurs and the liquid spreads along grain boundaries as a thin film. Upon quenching, intergranular cracks are found at grain boundaries where a liquid film penetrated during solution treatment. For slower heating rates, nonequilibrium eutectic melting does not occur and no intergranular cracks are observed after quenching. No evidence of nonequilibrium eutectic melting was found in the Al-Li-Cu alloy, irrespective of heating rate to 550°C. During tensile testing of as-quenched and quenched-and-aged specimens of the two alloys, intergranular fracture occurred in most cases, irrespective of whether nonequilibrium eutectic melting had taken place during solution treatment, indicating that at least one additional mechanism of intergranular fracture is invoked by deformation.

1. INTRODUCTION

Intergranular fracture occurs in Al-Li-Cu-(Mg) alloys to a greater extent than in other precipitation-hardening aluminum alloys. Since intergranular fracture may limit application of Al-Li alloys in some cases, it has been the focus of many investigations.¹⁻³¹ Most of the investigations have sought to identify the cause(s) of intergranular fracture in commercial-type alloys. However, as a result of the complex compositions of these alloys, it has been difficult to establish conclusively the importance of various factors that may contribute to intergranular fracture. A minority of the investigations have examined simpler alloy compositions specially prepared for investigation of the effects of specific factors on intergranular fracture.

The proposed explanations for intergranular fracture of Al-Li-base alloys fall into four broad categories: stress concentration due to planar slip in underaged alloys,^{1,4-6,9-11,16,18,20,28} strain localization in precipitate free zones (PFZs),^{1,3-6,8-11,17} fracture caused by grain boundary precipitate particles in peak-aged and overaged alloys,^{2,14-21,23,24,26,27} and segregation of Na and K impurities to grain boundaries.^{7,12,13,22,29-31} Of these explanations, segregation of Na and K to grain boundaries is the most clearly-established mechanism because it is possible to prepare alloys with low concentrations of these impurity elements, thus eliminating the effects. Of the remaining three explanations, the available

evidence now suggests that intergranular fracture is often controlled by grain boundary particles, either precipitate phases or constituent phases. Strain localization effects (planar slip or localized slip in PFZs) may be predominant in underaged alloys, and may also interact with the grain boundary particle mechanism by concentrating stress at grain boundaries.

The main purpose of the present paper is to show that nonequilibrium eutectic melting during solution treatment is an additional mechanism of intergranular fracture in an Al-Li-Cu-Mg alloy. Through this mechanism, grain boundary cracks can be introduced by heat-treatment prior to tensile deformation.

2. EXPERIMENTAL

Two alloys were used in this investigation; the analyzed compositions are listed in Table 1. The Al-Li-Cu-Mg alloy conforms to the AA8091 specification. With the exception of Zr, the Al-Li-Cu alloy conforms to the composition specification for AA2090; the 0.18 wt % Zr addition to this alloy exceeds the upper limit of 0.15 wt % for AA2090. The alloys were DC cast with 168 x 81 mm cross sections. After casting, they were homogenized for 24 hours at $543^{\circ}\text{C} \pm 5^{\circ}\text{C}$, hot rolled to a thickness of 12.7 mm, and air-cooled to ambient temperature. Solution treatment was performed in a salt bath, or in an air furnace in which the heating rate could be controlled. Except where noted, solution treatment was carried-out for 0.5 h, after which specimens were water-quenched. In cases where specimens were aged after

solution treatment, aging was conducted in a recirculating air furnace.

Optical metallography and transmission electron microscopy specimens were prepared using standard methods; Kellers reagent was used to reveal grain boundaries. Intergranular cracking caused by nonequilibrium eutectic melting was most easily detected using polished but unetched specimens. Round tensile specimens were prepared with the longitudinal axis parallel to the rolling direction of the plate. Tensile specimens had gauge sections 6.3 mm in diameter and 25.4 mm long, and were tested at room temperature with an initial strain rate of $2 \times 10^{-3} \text{ s}^{-1}$.

3. OBSERVATIONS

3.1 Grain Structure

The grain structure of both alloys after solution treatment at 530°C is shown in Figure 1. The Al-Li-Cu-Mg alloy has a larger grain size than the Al-Li-Cu alloy. Values of the grain intercept length in the short transverse direction are listed in Table 2, along with calculated values of grain boundary area per unit volume and other parameters described in a later section.

Grain size in the cast ingots was measured. Since the total reduction during hot working was known, the grain intercept length in the short transverse direction in the rolled plates could be calculated assuming that recrystallization did not take

place during hot rolling. This value was compared with the observed grain intercept length measured in the short transverse direction in the rolled plates. The calculated values of grain intercept length were close to the observed values, consistent with the idea that recrystallization did not occur during hot rolling. Previous investigators have suggested that many types of Al-Li alloys containing minor additions of Zr are unrecrystallized after hot rolling.^{32,33}

3.2 Intergranular Cracks in Solution-Treated and Quenched Specimens

3.2.1 Salt Bath Solution Treatment

Optical microscopy of the LS plane of specimens solution treated in a salt bath at 545° and 550°C revealed intergranular cracks in the Al-Li-Cu-Mg alloy; Figure 2 shows an example of such a crack. Many of the grain boundary cracks were longer than 1 mm. No cracks were found in samples of the Al-Li-Cu-Mg alloy solution treated in a salt bath at 540°C or lower temperatures, nor were any cracks found in the Al-Li-Cu alloy solution treated in a salt bath at 550°C or lower temperatures.

Transmission electron microscopy (TEM) specimens were prepared from quenched samples of the Al-Li-Cu-Mg alloy in an effort to further characterize the nature of the intergranular cracks. Figure 3 shows the morphology of the grain boundary in a location where an intergranular crack was found in the thin area of a TEM foil. The schematic diagram in Figure 3a shows the

overall geometry of this specimen, while the TEM micrograph shows the detailed morphology of the grain boundary just beyond the crack tip. It is evident from the dark field micrograph that a continuous grain boundary phase is interposed between the two matrix grains. Electron diffraction revealed that the grain boundary phase has an fcc crystal structure with a lattice parameter indistinguishable (by conventional electron diffraction) from that of the normal grains, but with a different lattice orientation than either of the neighboring grains.

Similar TEM observations of intergranular cracks were made in other thin foils taken from specimens of the Al-Li-Cu-Mg alloy solution treated in a salt bath at 550°C. In every case where an intergranular crack was observed in a TEM specimen, the continuous intergranular phase with the same crystal structure and lattice parameter as the matrix phase was present at the grain boundary which had fractured.

Optical metallography and TEM specimens were prepared from quenched samples of the Al-Li-Cu-Mg alloy solution treated in a salt bath at 500°C, 530°C and 540°C, and from the Al-Li-Cu alloy solution treated in a salt bath at 550°C. No grain boundary cracks were found in the metallographic specimens, and both grain boundary cracks and the intergranular phase were absent in TEM specimens.

Several TEM specimens of the Al-Li-Cu-Mg alloy were prepared after solution treatment in a salt bath at 550°C for 30 s, in an attempt to observe incompletely dissolved grain boundary

particles in conjunction with the grain boundary phase. In one case, an undissolved particle with a diameter of approximately 2 μm was found at a grain boundary where the grain boundary phase was present. Energy dispersive x-ray analysis of this particle showed that it contained Al and Cu in a ratio of approximately 2:1. Mg was not detected while analyzing this particle, but its Li content is uncertain because Li is not detectable by EDS methods. The grain boundary particle was too large to permit electron diffraction information to be obtained.

3.2.2 Air Furnace Solution Treatment

A set of experiments was performed to discover whether the incidence of intergranular cracking of the Al-Li-Cu-Mg alloys was affected by the heating rate to 550°C. An air furnace whose heating rate could be controlled was used for these experiments, the specimen was quenched immediately upon reaching 550°C to avoid complications associated with overshooting this temperature. Quenched specimens were observed using optical metallography to detect intergranular cracks formed during solution treatment.

Figure 4 shows the results obtained using various heating-rate and solution-treatment-temperature combinations for the Al-Li-Cu-Mg alloy. The heating rate for specimens immersed in a molten salt bath has been previously reported,³⁴ values near 2×10^5 K/h were found for specimens of the size used in the present investigation. These data suggest that the critical

heating rate required to produce intergranular cracks at 545°C or above is between 50 and 100 K/h for the Al-Li-Cu-Mg alloy.

Two additional experiments were performed to further evaluate the effect of heat treatment history on intergranular fracture.

S1: A specimen was heated to 550°C at 20 K/h, held for 0.5 h and water quenched. The same specimen was then reheated to 550°C in a salt bath, held for 0.5 h and water quenched. Optical metallography revealed no intergranular cracks following the initial slow heating treatment, nor were any intergranular cracks found after the subsequent salt bath solution treatment.

S2: A specimen was heated to 550°C at 20 K/h, held for 0.5 h, then cooled to room temperature at 10 K/h. The same specimen was then reheated to 550°C in a salt bath, held for 0.5 h and water quenched. Optical metallography revealed no intergranular cracks following the initial slow heating treatment, but intergranular cracks were present after the subsequent salt bath solution treatment.

3.3 Tensile Properties

Tensile tests were performed to determine whether the intergranular cracks found after salt bath solution treatment at 550°C affected longitudinal tensile properties. Figure 5 shows results of these tests, which reveal that presence or absence of intergranular cracks prior to testing does not influence the elongation to failure of the Al-Li-Cu-Mg alloy when the tensile

axis is parallel to the rolling direction. Tensile properties were also measured as a function of aging time at 170°C after solution treatment in a salt bath at 550°C. Figure 6 shows the results of these tests. Both alloys achieve peak strength for an aging time near 200 hours at 170°C.

3.4 Fracture Surface Characterization

Figure 7 shows the general fracture surface appearance found for tensile specimens of both the Al-Li-Cu-Mg alloy and the Al-Li-Cu alloy for nearly all aging conditions. Intergranular fracture is manifested by secondary cracks on the surface of the longitudinal tensile specimens, with transgranular fracture found between the secondary cracks. The only exception to this fracture surface topology was found for as-quenched specimens of the Al-Li-Cu alloy. In this case, the secondary cracks did not appear, indicating that intergranular fracture had not occurred during tensile deformation.

To explore further the nature of the intergranular cracking behavior in the alloys under investigation, failed tensile specimens were sectioned parallel to the LS plane after straining to failure. Metallographic examination of the microstructure below the fracture surface was then conducted. An example of one such specimen is shown in Figure 8. These observations confirmed that secondary cracks on the fracture surface represent intergranular fracture in both alloys.

The propensity for intergranular fracture during longitudinal tensile straining was quantitatively assessed by determining the fraction of cracked grain boundaries (f_C) across the fracture surface of a tensile specimen. Referring to Figure 8, f_C was found by dividing the number of fractured grain boundaries by the total number of grain boundaries intersecting the fracture surface. Grain boundaries that produced either a secondary crack or a fracture plane parallel to the loading axis were counted as fractured boundaries. Results of these measurements are shown in Figures 9 and 10 where the fraction of grain boundaries producing an intergranular crack during tensile deformation is shown as a function of solution treatment temperature (Fig. 9), and as a function of aging time after solution treatment at 550°C (Fig. 10).

4. DISCUSSION

4.1 Intergranular Cracking in Solution Treated and Quenched Specimens

Ashton and coworkers³⁵ reported that the yield strength of alloys conforming to the AA2090 and AA8091 specifications increases continuously as the solution treatment temperature is raised to 543°C. Consequently, there is an incentive to increase the solution treatment temperature at least to 543°C. However, the present investigation shows that heating an Al-Li-Cu-Mg alloy to a solution treatment temperature of 545°C or above at a rate of 100 K/h or faster can cause intergranular cracking, without application of an external stress. Solution treatment of the

same alloy at 540°C or below did not produce intergranular cracks, irrespective of the heating rate. Moreover, intergranular cracks after quenching were observed only in conjunction with a grain boundary phase having the same crystal structure and lattice parameter as the aluminum matrix.

The observations described above can be interpreted in terms of nonequilibrium eutectic melting occurring when the Al-Li-Cu-Mg alloy is heated above 545°C at a critical heating rate, which is between 50 and 100 K/h for the present Al-Li-Cu-Mg alloy. For slower heating rates, soluble particles initially present at grain boundaries dissolve normally during solution treatment because the heating rate is insufficient to produce large departure from equilibrium. For heating rates above the critical rate, grain boundary particles are not dissolved before the temperature exceeds the eutectic temperature, causing melting in the matrix adjacent to the particle.

If the solid-liquid interfacial energy for liquid of the eutectic composition (Γ_{ls}) is lower than half of the grain boundary energy (Γ_{gb}), the liquid spreads out as a thin layer along the grain boundary.³⁷ As solution treatment continues, the excess solute present in the liquid diffuses into the adjoining aluminum grains, causing the liquid to solidify as a thin grain of aluminum interposed between the original grains. This accounts for the presence of narrow grains with the fcc crystal structure interposed between grains of normal thickness after rapid heating.

As noted above, the intergranular film morphology of the liquid phase requires $\Gamma_{gb} > 2\Gamma_{ls}$. Published values for Γ_{gb} and Γ_{ls} for Al-Li-base alloys could not be found, precluding direct verification of the above inequality for this case. Surface tension measurements (liquid-vapor interfacial energy, Γ_{lv}) have been reported for several binary aluminum alloys, including Al-Li alloys.^{37,38} All reported results indicate that Li additions strongly lower Γ_{lv} . Mg has also been reported to lower Γ_{lv} of aluminum.³⁸⁻⁴⁰ While these results do not indicate whether Li and Mg affect the ratio $\Gamma_{gb}:\Gamma_{ls}$, they do show that Li and Mg can strongly decrease one type of interfacial energy of aluminum alloys. Thus, it is not unreasonable to propose that Li, Mg or Li and Mg in combination decrease Γ_{ls} enough to satisfy the requirement for grain boundary film formation.

The phase responsible for nonequilibrium eutectic melting is a fully-soluble, precipitate phase which can be dissolved and reprecipitated, as demonstrated by experiments S1 and S2. From S1, we observe that heating the alloy to 550°C at a slow rate and quenching suppresses intergranular cracking during a subsequent rapid heating treatment. This is consistent with the nonequilibrium eutectic melting mechanism because slow heating allowed coarse grain boundary particles to dissolve without producing a liquid phase, and quenching prevented reprecipitation of coarse particles prior to the rapid heating step. In S2, the alloy was slowly cooled from the initial 550°C solution treatment, providing the grain boundary particles an opportunity

to reprecipitate. In this case, subsequent rapid heating produced nonequilibrium eutectic melting as described previously. Thus, the nonequilibrium eutectic melting phenomenon observed in the Al-Li-Cu-Mg alloy is associated with a fully-soluble, precipitate phase, not with a nonequilibrium phase resulting from solidification.

Both equilibrium and nonequilibrium eutectic melting have been observed in many precipitation-strengthened aluminum alloys; these effects are commonly termed "overheating".⁴¹⁻⁴³ The classic paper on this topic was published by Crowther⁴¹ who investigated Al-Cu-Mg-Si alloys. He described the various morphologies of liquid phase that may form as a result of eutectic melting: globular pools, networks penetrating along grain edges, and grain boundary films. Crowther's experiments further showed that intergranular cracks are caused by quenching stresses at grain boundaries where liquid phase had penetrated at high temperature.

The only significant departure from Crowther's observations found in the present investigation is the composition of the intergranular film. Crowther suggested that the intergranular film solidified as "a more or less continuous band of intermetallic compound", whose brittle nature resulted in formation of intergranular cracks upon quenching. He proposed that a protracted solution treatment would be required to dissolve the intermetallic particles produced by overheating. In the present investigation, we have found that a narrow

intergranular liquid film transforms to a grain of aluminum alloy during a 0.5 h solution treatment, or during subsequent cooling. The cause of cracking is not as clear in the present case as it is when a continuous film of intermetallic phase forms at the grain boundary.

An effort was made to establish which phase caused nonequilibrium eutectic melting in the Al-Li-Cu-Mg alloy by locating a grain boundary particle in conjunction with the grain boundary phase in a TEM specimen solution treated for 30 seconds at 550°C. Longer solution treatment times allow the intermetallic particles to dissolve completely, precluding their observation. One such occurrence was observed, as described previously. However, since the liquid phase often penetrates along a grain boundary over a length of more than 1 mm, it was not possible to conclude that the particular particle under observation was responsible for formation of the liquid phase. We were unable to identify the phase responsible for nonequilibrium eutectic melting.

Shamray and Fridlyander⁴⁴ reported equilibrium eutectic melting in Al-Li-Cu-Mg alloys. For alloy compositions falling within the Al - Al₂CuMg - Al₂CuLi phase field, the eutectic temperature was reported to be 505°C. Other phase fields were reported to have higher eutectic melting temperatures. Our inability to establish the composition of the particles responsible for formation of the liquid phase prevented detailed analysis of the results of the present investigation using the

observations of Shamray and Fridlyander. However, their results do show that eutectic temperatures for equilibrium phases in Al-Li-Cu-Mg alloys can be as low as 505°C.

Webster^{12,22,30,31} and others²⁹ have suggested that the low toughness of Al-Li-base alloys of various types is attributable to liquid phases formed by Na and K impurities at aging temperatures near 170°C. However, according to Webster, the Na and K responsible for formation of the liquid phases are in solid solution at the solution treatment temperature. Therefore, the intergranular phase observed in the present case in quenched specimens could not be the same as that proposed by Webster.

Having established an association between nonequilibrium eutectic melting and intergranular cracking in one Al-Li-Cu-Mg alloy, it is of value to consider under what conditions this same phenomenon could occur in other Al-Li-Cu-Mg alloys. As described above, the phase(s) responsible for melting in the Al-Li-Cu-Mg alloy are completely soluble. This indicates that the elements incorporated into these phase(s) were in solution during the homogenization treatment, and precipitated on grain boundaries during subsequent hot rolling, or during cooling from the hot rolling treatment. As a consequence, the critical heating rate to 545°C is expected to depend on processing conditions during cooling from homogenization, and during hot rolling and subsequent cooling to ambient temperature. Since the processing conditions during and after hot rolling may be loosely-controlled in commercial production, the critical heating rate could be

expected to vary for different plates with identical compositions.

4.2 Intergranular Fracture During Tensile Deformation.

The eutectic melting phenomenon described in the previous section cannot be responsible for intergranular fracture during tensile deformation of the Al-Li-Cu-Mg alloy when solution treatment temperatures of 540°C and below are employed. Nor can eutectic melting account for intergranular fracture of the Al-Li-Cu alloy during tensile deformation. Thus, at least one additional mechanism of intergranular fracture must be invoked by longitudinal tensile deformation.

The Na and K concentration in the Al-Li-Cu-(Mg) alloys can be converted into grain boundary concentrations by assuming that all of the Na and K is segregated to the grain boundaries. This calculation yields an upper bound for the grain boundary concentration of Na and K in each alloy, denoted $(GBC)_{Na}$ and $(GBC)_K$. Values for these parameters for the present investigation and for two previous investigations are included in Table 2. It can be seen that the upper-bound grain boundary concentrations of Na and K in the present alloys are substantially lower than the concentrations in alloys studied by Vasudevan, Miller and Kersker⁷ and by Wert and Lumsden.¹³ In particular, $(GBC)_{Na}$ in both alloys is more than an order of magnitude lower than the value of $(GBC)_{Na}$ found by Vasudevan and coworkers to produce exclusively intergranular fracture in as-

quenched Al-Li-Mn-(Na) alloys. Thus, it appears unlikely that grain boundary fracture is caused by these impurity elements in the present investigation.

The remaining mechanisms proposed to explain intergranular fracture during deformation of Al-Li alloys are: fracture initiated at grain boundary particles, strain localization in PFZs and stress concentrations due to planar slip. The microstructural characteristics associated with each of these intergranular fracture mechanisms evolve during aging. Comparing the results shown in Figures 6 and 10, it is seen that the fraction of cracked grain boundaries increases by 10 to 15 % prior to reaching the peak strength condition, then remains approximately constant. This observation does not strongly support or reject any of the individual grain boundary fracture mechanisms described above.

5. SUMMARY

This investigation has examined intergranular fracture during heat treatment and deformation of an Al-Li-Cu-Mg alloy and an Al-Li-Cu alloy. When solution treatment of the Al-Li-Cu-Mg alloy is carried out by rapidly heating the alloy to a temperature of 545°C or above, nonequilibrium eutectic melting of a soluble phase occurs in this alloy. The liquid spreads along grain boundaries as a thin film, which solidifies by diffusion of solute into the adjoining grains. Upon quenching, intergranular cracks are found at grain boundaries where a liquid film had

penetrated during solution treatment. At solution treatment temperatures of 540°C and below, nonequilibrium eutectic melting did not occur and no intergranular cracks were found in as-quenched specimens, irrespective of heating rate. No evidence of nonequilibrium eutectic melting was found in the Al-Li-Cu alloy. During tensile testing of as-quenched and quenched-and-aged specimens, intergranular fracture occurred irrespective of whether or not nonequilibrium eutectic melting had taken place during solution treatment. The concentrations of K and Na in the alloys are below levels found to cause intergranular fracture in prior investigations. However, the present results are not able to distinguish between the other mechanisms proposed to account for intergranular fracture of Al-Li alloys during tensile deformation.

6. ACKNOWLEDGMENTS

The authors wish to thank the Air Force Office of Scientific Research (Contract Number 83-0061-C), ALCOA and Cegedur Pechiney for financial support.

7. REFERENCES

1. T.H. Sanders Jr, E.A. Ludwiczak and R.R. Sawtell: Mat. Sci. Engr., 1980, 43, 247-260.
2. K. Dinsdale, S.J. Harris and B. Noble: in 'Aluminum-Lithium Alloys', (eds T.H. Sanders Jr and E.A. Starke Jr), 101-118; 1981, Warrendale, The Metallurgical Society of AIME.
3. F.W. Gayle: in 'Aluminum-Lithium Alloys', (eds T.H. Sanders Jr and E.A. Starke Jr), 119-139; 1981, Warrendale, The Metallurgical Society of AIME.
4. A. Gysler, R. Crooks and E.A. Starke Jr: in 'Aluminum-Lithium Alloys', (eds T.H. Sanders Jr and E.A. Starke Jr), 119-139; 1981, Warrendale, The Metallurgical Society of AIME.
5. B. Noble, S.J. Harris and K. Dinsdale: Metal Science, 1982, 16, 425-430.
6. E.A. Starke Jr, T.H. Sanders Jr and I.G. Palmer: J. Metals, 1981, 33, (8), 24-33.
7. A.K. Vasudevan, A.C. Miller and M.M. Kersker: in 'Aluminum-Lithium Alloys II', (eds E.A. Starke Jr and T.H. Sanders Jr), 181-199; 1984, Warrendale, The Metallurgical Society of AIME.
8. S.J. Harris, B. Noble and K. Dinsdale: in 'Aluminum-Lithium Alloys II', (eds E.A. Starke Jr and T.H. Sanders Jr), 181-199; 1984, Warrendale, The Metallurgical Society of AIME.
.pa
9. T.H. Sanders Jr and E.A. Starke Jr: Acta Met., 1982, 30, 927-939.
10. F.S. Lin, S.B. Chakraborty and E.A. Starke Jr: Met. Trans., 1982, 13A, 401-410.
11. E.A. Starke Jr and F.S. Lin: Met. Trans., 1982, 13A, 2259-2269.
12. D. Webster: Metal Progress, 1984, (4), 33-37.
13. J.A. Wert and J.B. Lumsden: Scripta Met., 1985, 19, 205-209.
14. A.K. Vasudevan, E.A. Ludwiczak, S. Baumann, R.D. Doherty and M.M. Kersker: Mat. Sci. Eng., 1985, 72, L25-L30.
15. P.J. Gregson and H.M. Flower: Acta Met., 1985, 33, 527-537.
16. E.P. Butler, N.J. Owen and D.J. Field: Mat. Sci. Tech., 1985, 1, 531-536.

17. O. Jensrud: in 'Aluminium-Lithium Alloys III', (eds C. Baker, P.J. Gregson, S.J. Harris and C.J. Peel), 411-419; 1986, London, The Institute of Metals.
18. J. White, W.S. Miller, I.G. Palmer, R. Davis and T.S. Saini: in 'Aluminium-Lithium Alloys III', (eds C. Baker, P.J. Gregson, S.J. Harris and C.J. Peel), 530-538; 1986, London, The Institute of Metals.
19. N.J. Owen, D.J. Field and E.P. Butler: in 'Aluminium-Lithium Alloys III', (eds C. Baker, P.J. Gregson, S.J. Harris and C.J. Peel), 576-583; 1986, London, The Institute of Metals.
20. W.S. Miller, M.P. Thomas, D.J. Lloyd and D. Creber: in 'Aluminium-Lithium Alloys III', (eds C. Baker, P.J. Gregson, S.J. Harris and C.J. Peel), 584-594; 1986, London, The Institute of Metals.
21. S. Suresh and A.K. Vasudevan: in 'Aluminium-Lithium Alloys III', (eds C. Baker, P.J. Gregson, S.J. Harris and C.J. Peel), 595-601; 1986, London, The Institute of Metals.
22. D. Webster: in 'Aluminium-Lithium Alloys III', (eds C. Baker, P.J. Gregson, S.J. Harris and C.J. Peel), 602-609; 1986, London, The Institute of Metals.
23. R.C. Dorward: Mat. Sci. Eng., 1986, 84, 89-95.
24. A.K. Vasudevan, E.A. Ludwiczak, S. Baumann, P.R. Howell, R.D. Doherty and M.M. Kersker: Mat. Sci. Tech., 1986, 2, 1205-1209.
25. W.S. Miller, M.P. Thomas, D.J. Lloyd and D. Creber: Mat. Sci. Tech., 1986, 2, 1210-1216.
26. S. Suresh, A.K. Vasudevan, M. Tosten and P.R. Howell: Acta Met., 1987, 35, 25-46.
27. A.K. Vasudevan and R.D. Doherty: Acta Met., 1987, 35, 1193-1219.
28. P. Meyer, Y. Cans, D. Ferton and M. Reboul, J. de Physique Colloque C3, 1987, 48, 131-138.
29. M. Niinomi, K. Degawa and T. Kobayashi, J. de Physique Colloque C3, 1987, 48, 653-658.
30. D. Webster, J. de Physique Colloque C3, 1987, 48, 685-691.
31. D. Webster, Met. Trans., 1987, 18A, 2181-2193.
32. P.L. Makin and W.M. Stobbs: in 'Aluminium-Lithium Alloys III', (eds C. Baker, P.J. Gregson, S.J. Harris and C.J. Peel), 392-401; 1986, London, The Institute of Metals.

33. M.J. Bull and D.J. Lloyd: in 'Aluminium-Lithium Alloys III', (eds C. Baker, P.J. Gregson, S.J. Harris and C.J. Peel), 402-410; 1986, London, The Institute of Metals.
34. C.C. Bampton, J.A. Wert and M.W. Mahoney, Met. Trans., (1982), 13A, 193-198.
35. R.F. Ashton, D.S. Thompson, E.A. Starke Jr, and F.S. Lin: in 'Aluminium-Lithium Alloys III', (eds C. Baker, P.J. Gregson, S.J. Harris and C.J. Peel), 66-77; 1986, London, The Institute of Metals.
36. C.S. Smith: J. Inst. Metals, 1949, 76, 726-728.
37. N. Eustathopoulos, J.C. Joud and P. Desre: J. Mat. Sci., 1974, 9, 1233-1242.
38. G. Lang: Aluminium, 1974, 50, 731-734.
39. V.V. Tekuchev and v.I. Stremousov: Russian J. Physical Chemistry, 1979, 53, 1502-1503.
40. C. Garcia-Cordovilla, E. Louis and A. Pamies: J. Mat Sci., 1986, 21, 2787-2792.
41. J. Crowther: J. Inst. Metals, 1949, 76, 201-236.
42. A.J. Bryant: Aluminium, 1974, 50, 638-640.
43. J.E. Hatch (ed): 'Aluminum: Properties and Physical Metallurgy', 150-155; 1984, Metals Park, Ohio, American Society for Metals.
44. Shamray and Fridlyander: Russian Met., 1969, (5), 113-117.

TABLE 1
Composition of Alloys (wt. %)

Element	Al-Li-Cu	Al-Li-Cu-Mg
Li	2.45	2.46
Cu	2.43	2.04
Mg	0.003	0.96
Zr	0.18	0.14
Fe	0.098	0.11
Si	0.089	0.047
Na	0.0014	0.0006
K	0.0005	0.0005
Ca	<0.0005	<0.0005
Al	balance	balance

TABLE 2
Grain Structure Characteristics

Alloy	Grain Intercept Length ⁺ μm	S_V m^{-1}	$(\text{GBC})_{\text{Na}}$ mol m^{-2}	$(\text{GBC})_{\text{K}}$ mol m^{-2}
Al-Li-Cu	18	5.6×10^4	2.8×10^{-5}	5.9×10^{-6}
Al-Li-Cu-Mg	40	2.5×10^4	2.7×10^{-5}	1.3×10^{-5}
Al-Li-Cu-Mg [13]	--	2.5×10^4	1.4×10^{-4}	2.9×10^{-4}
Al-Li [7]	--	7.6×10^3	5.2×10^{-5}	5.2×10^{-5}
Al-Li [7]	--	7.6×10^3	7.0×10^{-4}	5.2×10^{-5}
Al-Li [7]	--	7.6×10^3	7.4×10^{-3}	5.2×10^{-5}

⁺ Short transverse direction.

FIGURE CAPTIONS

- Fig. 1 Grain structures after solution treatment at 530°C.
a) Al-Li-Cu-Mg. b) Al-Li-Cu.
- Fig. 2 Intergranular crack in the Al-Li-Cu-Mg alloy after salt bath solution treatment at 550°C.
- Fig. 3 TEM observations in the vicinity of an intergranular crack in the Al-Li-Cu-Mg alloy after salt bath solution treatment at 550°C. a) Schematic diagram. b) Bright field TEM micrograph. c) Dark field TEM micrograph showing intergranular phase.
- Fig. 4 Temperature and heating rate combinations producing intergranular cracks in the Al-Li-Cu-Mg alloy.
- Fig. 5 Tensile properties of as-quenched specimens, as a function of solution treatment temperature.
- Fig. 6 Tensile properties as a function of aging time at 170°C for specimens solution treated at 550°C.
- Fig. 7 Fracture surface of Al-Li-Cu-Mg alloy tensile specimen strained to failure. (Solution treated at 550°C and aged 48 h at 170°C.)
- Fig. 8 Cross section of the tensile specimen shown in Figure 7. (Solution treated at 550°C and aged 48 h at 170°C.)
- Fig. 9 Fraction of fractured grain boundaries across the fracture surface of tensile specimens as a function of solution treatment temperature.
- Fig. 10 Fraction of fractured grain boundaries across the fracture surface of tensile specimens as a function of aging time at 170°C after salt bath solution treatment at 550°C.

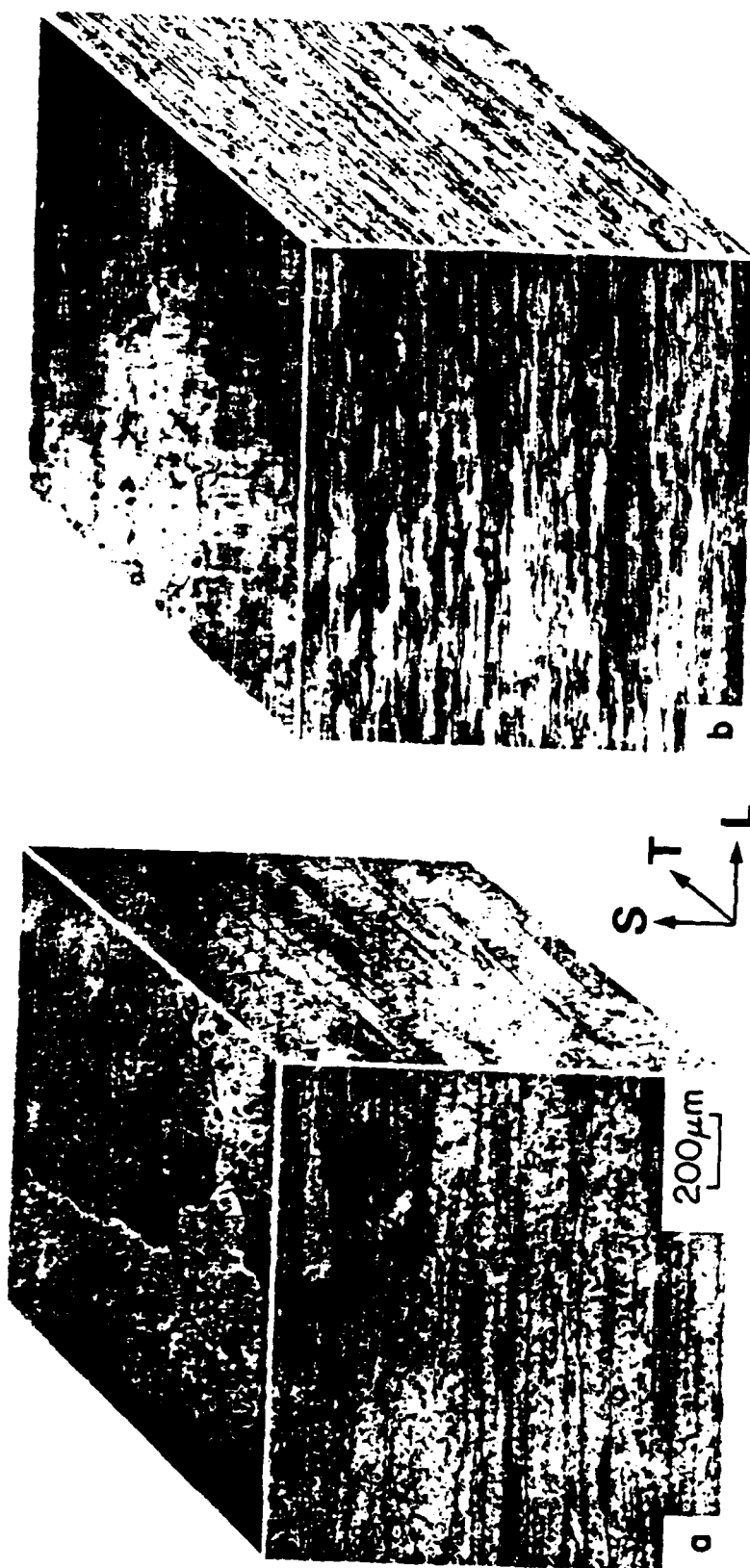


Fig. 1 Grain structures after solution treatment at 530°C.
a) Al-Li-Cu-Mg. b) Al-Li-Cu.

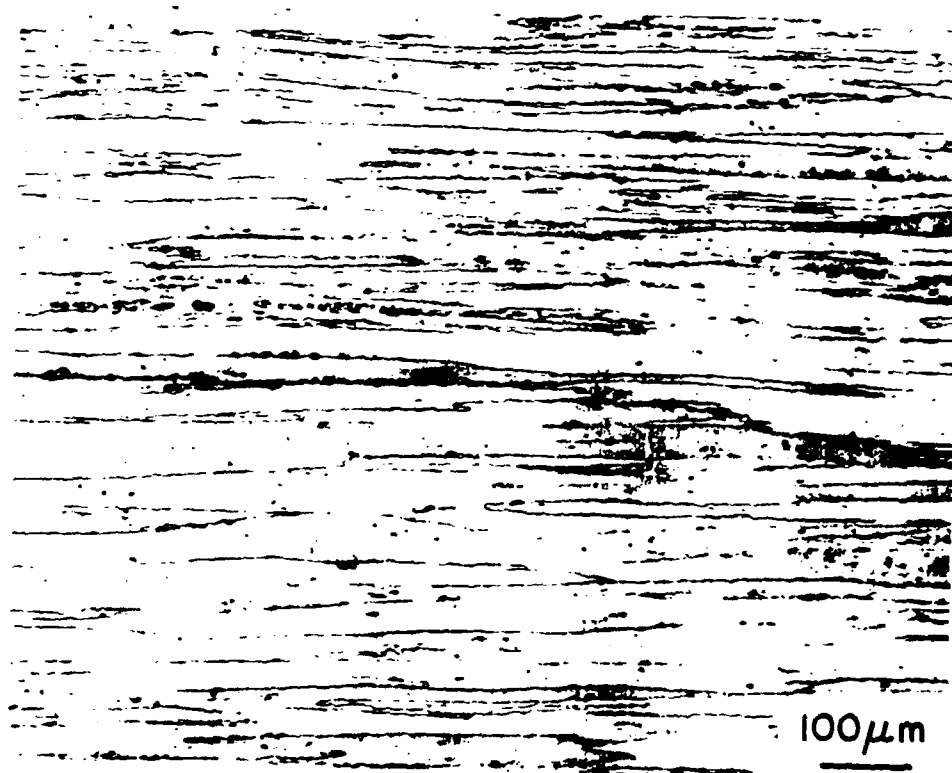


Fig. 2 Intergranular crack in the Al-Li-Cu-Mg alloy after salt bath solution treatment at 550°C.

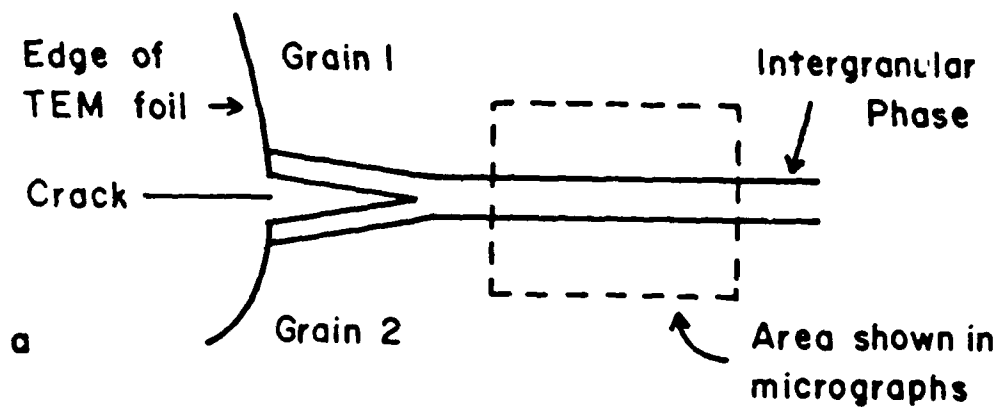


Fig. 3 TEM observations in the vicinity of an intergranular crack in the Al-Li-Cu-Mg alloy after salt bath solution treatment at 550°C. a) Schematic diagram. b) Bright field TEM micrograph. c) Dark field TEM micrograph.

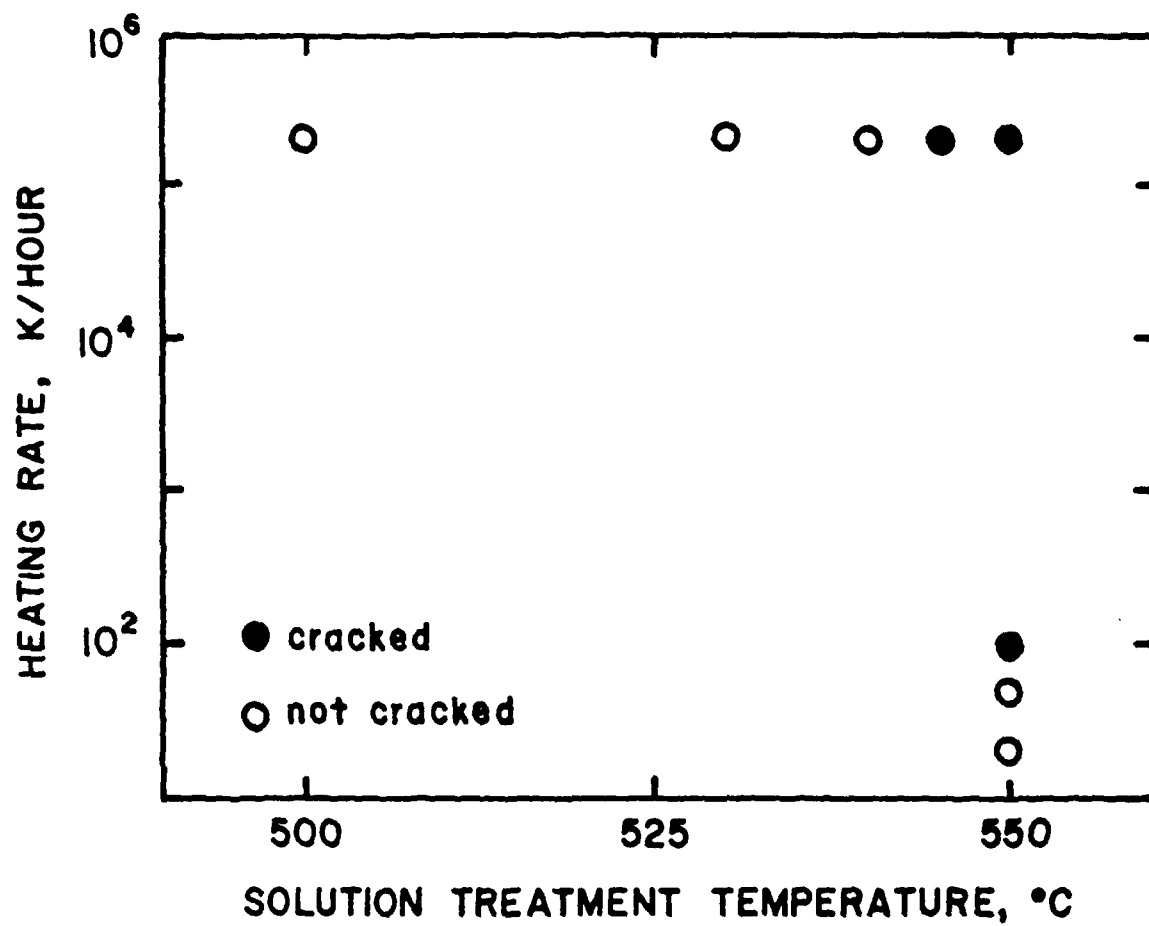


Fig. 4 Temperature and heating rate combinations producing intergranular cracks in the Al-Li-Cu-Mg alloy.

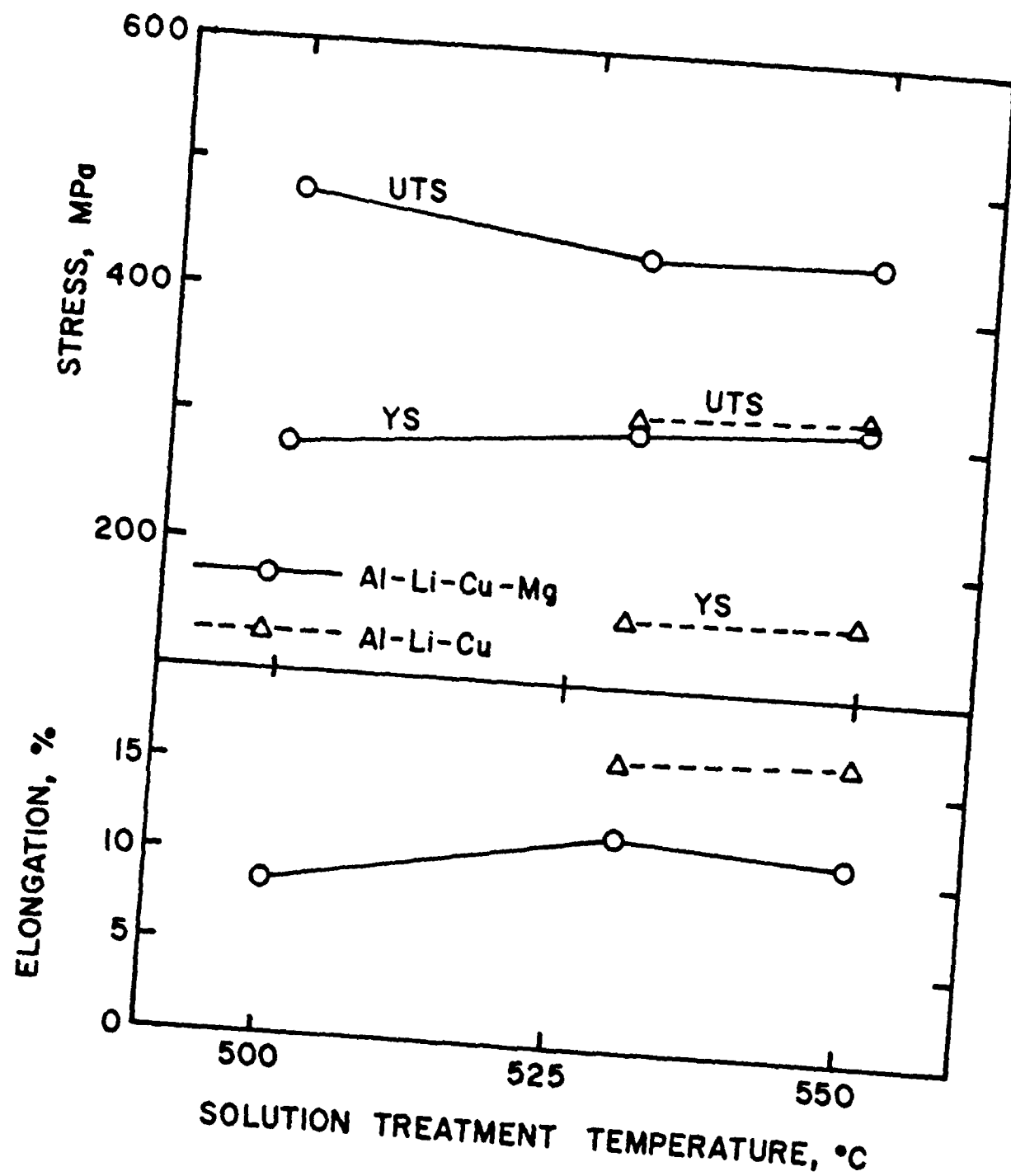


Fig. 5 Tensile properties of as-quenched specimens, as a function of solution treatment temperature.

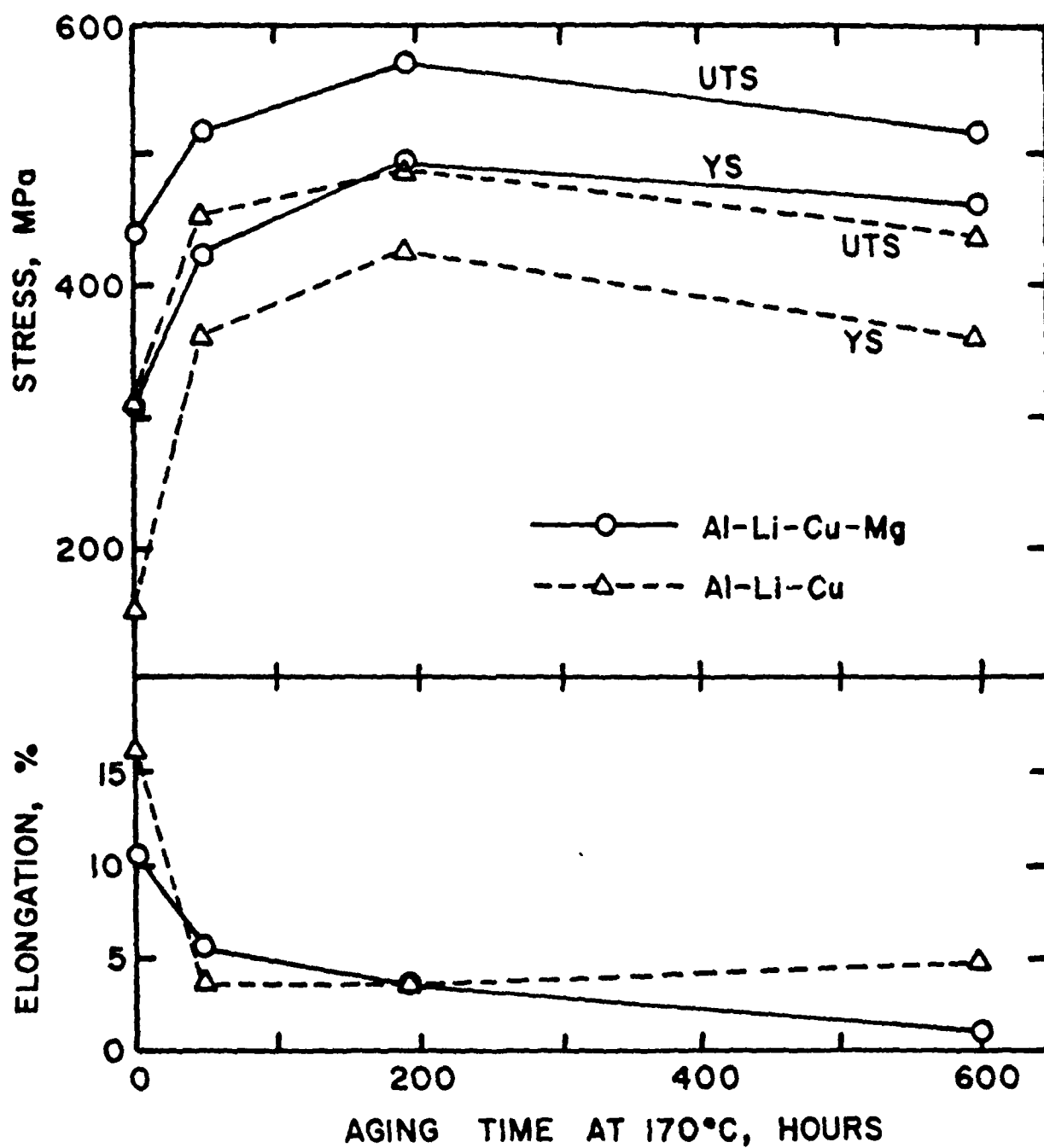


Fig. 6 Tensile properties as a function of aging time at 170°C for specimens solution treated at 550°C.

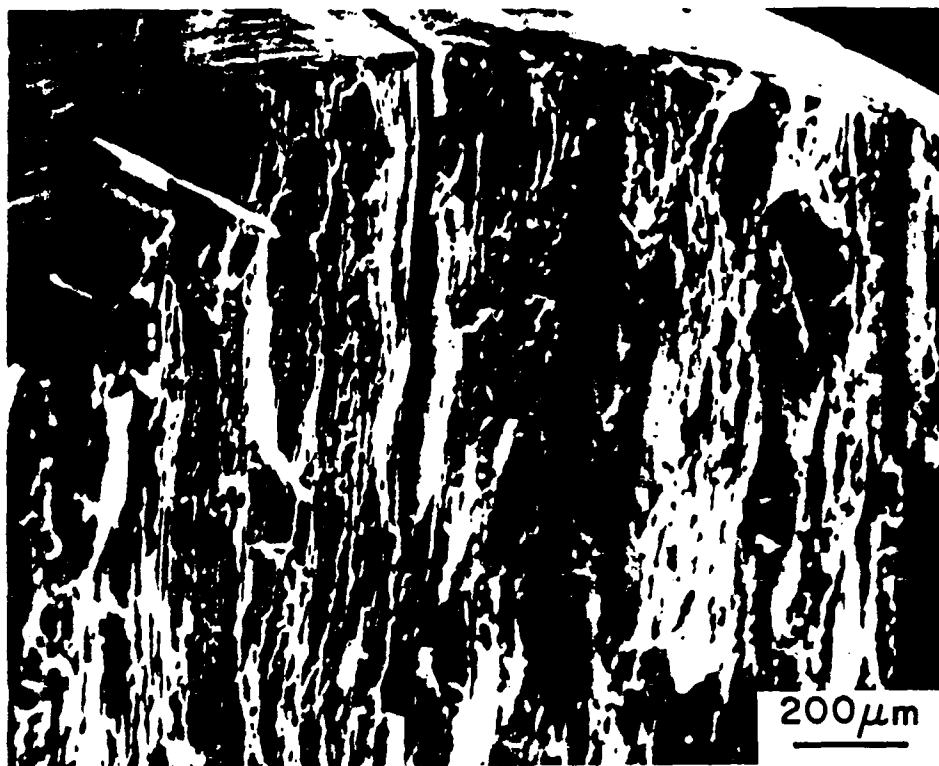


Fig. 7 Fracture surface of Al-Li-Cu-Mg alloy tensile specimen strained to failure. (Solution treated at 550°C and aged 48 h at 170°C.)

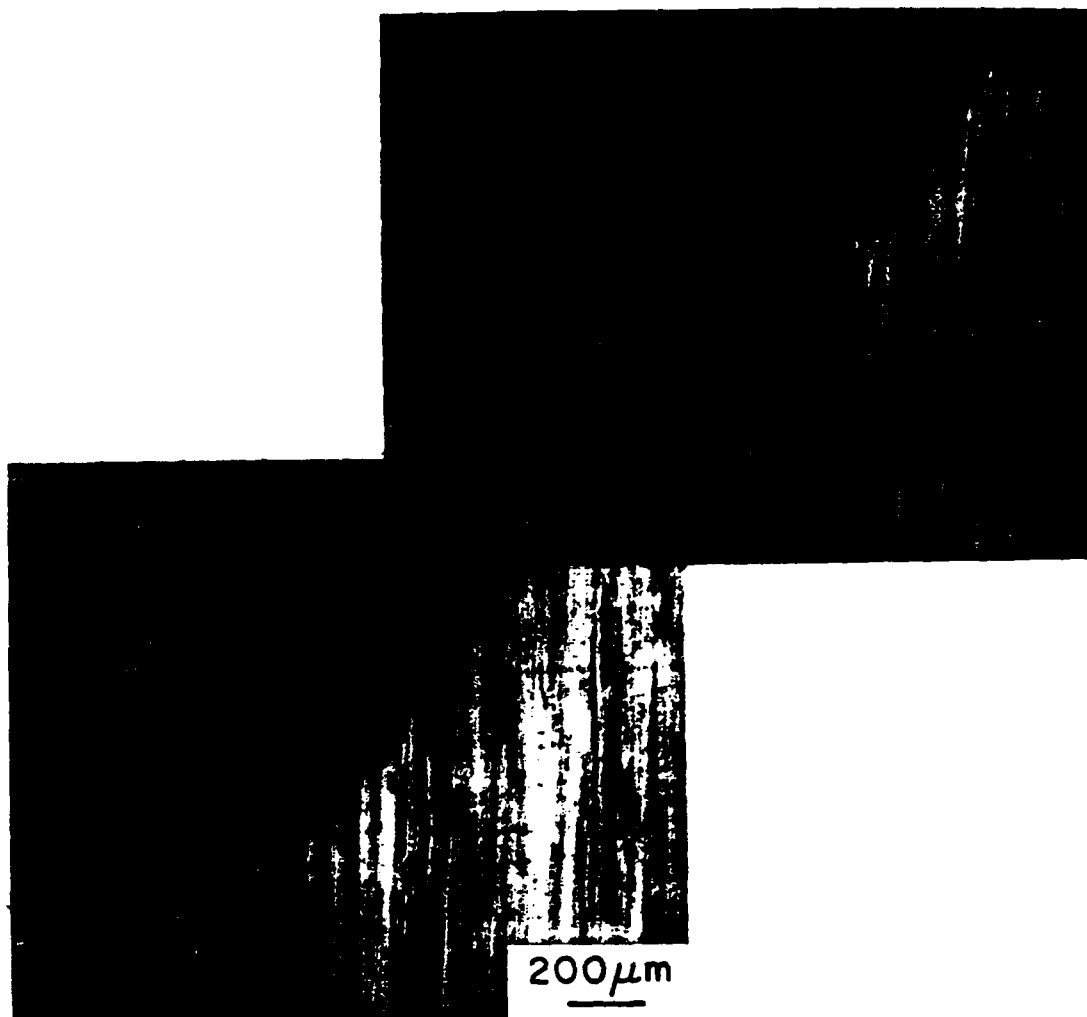


Fig. 8 Cross section of the tensile specimen shown in Figure 7.
(Solution treated at 550°C and aged 48 h at 170°C.)

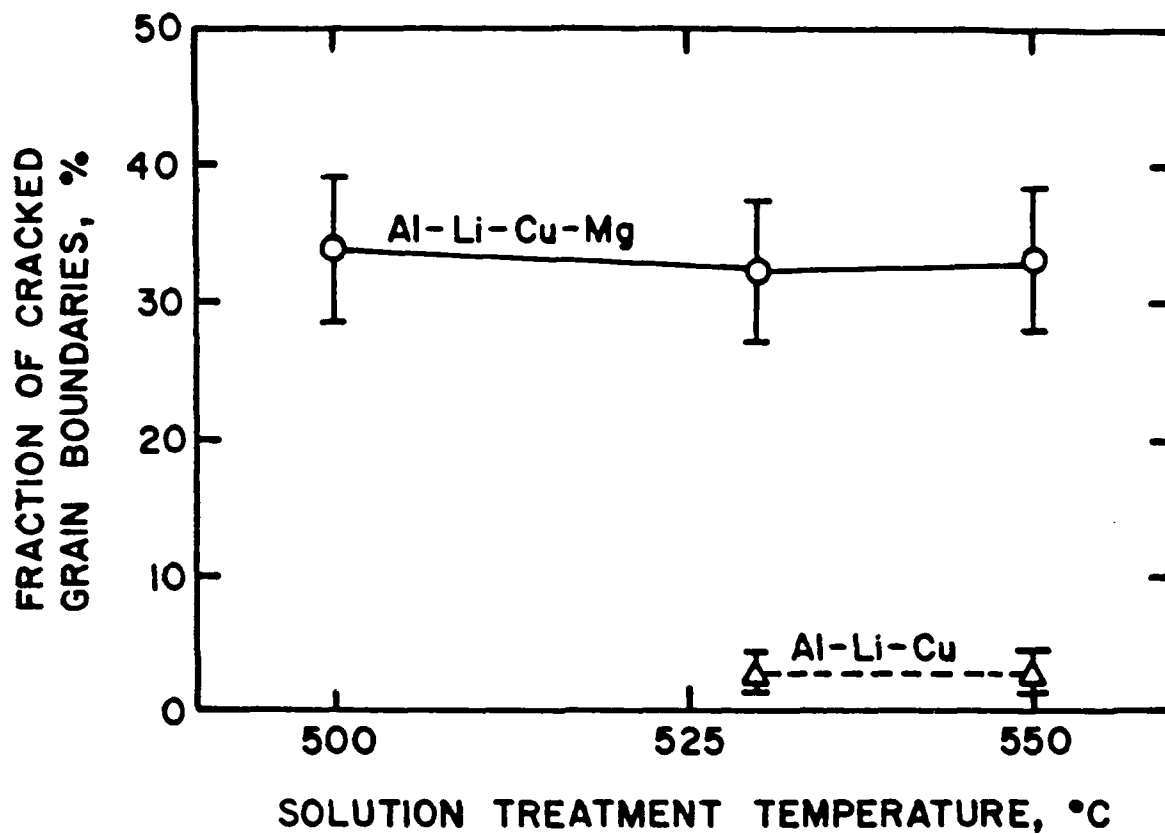


Fig. 9 Fraction of fractured grain boundaries across the fracture surface of tensile specimens as a function of solution treatment temperature.

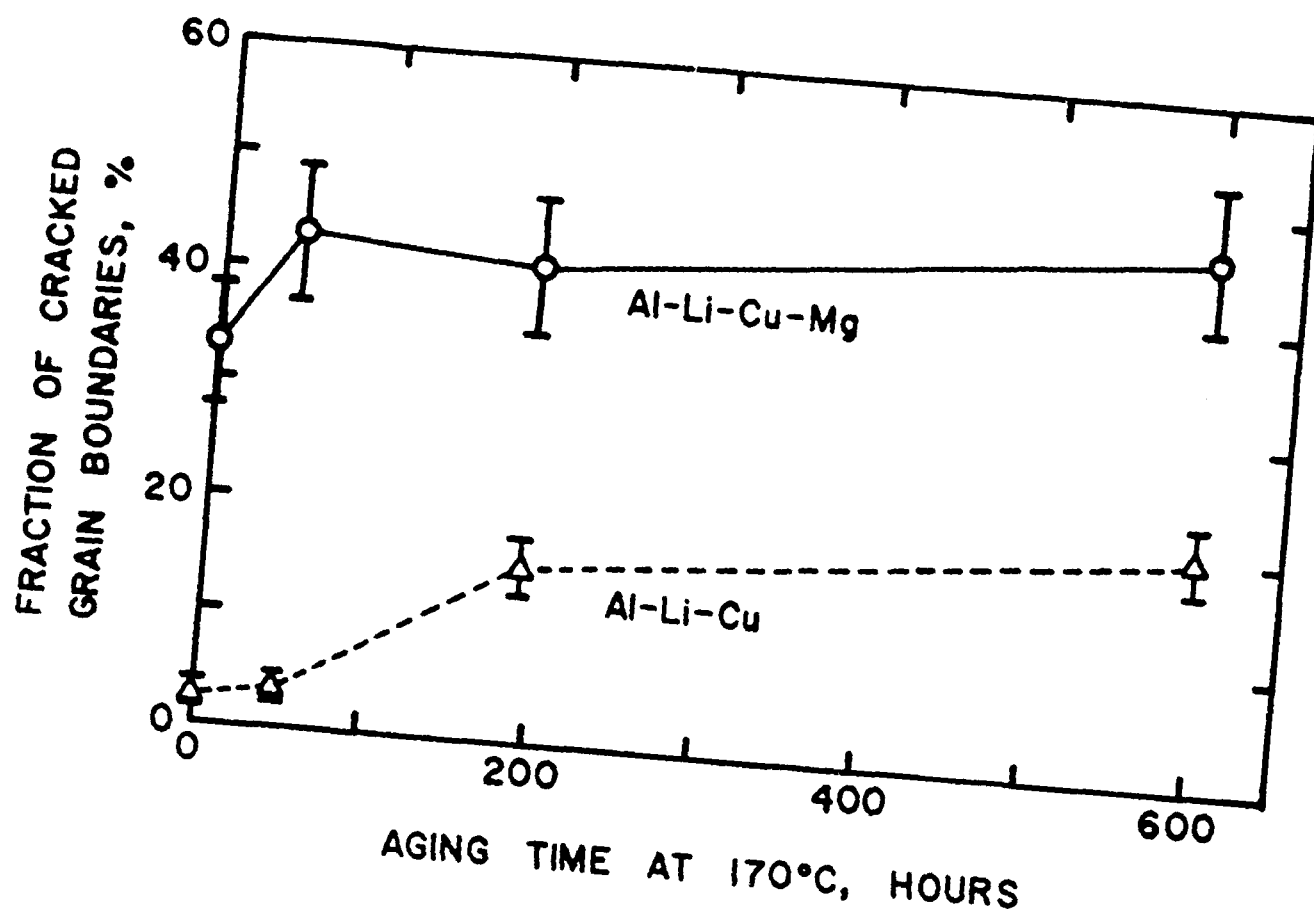


Fig. 10 Fraction of fractured grain boundaries across the fracture surface of tensile specimens as a function of aging time at 170°C after salt bath solution treatment at 550°C.

Submitted to Fatigue and Fracture of Engineering
Materials and Structures
THE FATIGUE CRACK GROWTH BEHAVIOR OF THE Al-Cu-Li ALLOY
WELDALITE 049

C.P. Blankenship, Jr. and E.A. Starke, Jr.
Department of Materials Science
University of Virginia
Charlottesville, VA 22901

ABSTRACT

The microstructure, deformation behavior, and crack growth relationships have been examined for an Al-5Cu-1.3Li-0.4Mg-0.4Ag-0.1Zr alloy. TEM of deformed samples revealed that the T3 temper deformed via highly localized planar slip due to the presence of small, coherent precipitates (GP zones and δ'), while the T8 temper deformed homogeneously with T_1 as the strengthening phase. Both constant K_{max} and constant R (0.1) fatigue curves were generated for the T3 and T8 tempers in both the T-L and L-T orientations. The T3 temper exhibited high closure levels and an apparent intrinsic threshold of 2 MPa $m^{1/2}$. The T8 temper did not exhibit high closure levels, and the intrinsic threshold was determined to be 1.3 MPa $m^{1/2}$. Weldalite-T3 has a strength comparable to 2024-T3 but has a higher resistance to fatigue crack growth, whereas Weldalite-T8 has a much higher strength and a comparable fatigue crack growth resistance to 2024-T8.

INTRODUCTION

A high strength, weldable Al-Cu-Li alloy, Weldalite 049, has recently been developed for use in aerospace launch vehicles and cryogenic tankage [1]. Economic considerations suggest that future launch vehicles must be reusable, and this requires that

materials used for structural components have adequate damage tolerance. Studies to date indicate that, in general, Al-Li-X alloys exhibit superior fatigue resistance when compared with other age-hardenable, high-strength aluminum alloys used in aerospace systems [2], suggesting that Weldalite may offer some advantage over those currently used for cryogenic tanks.

The superior fatigue resistance of Al-Li-X alloys may be associated with one or more of the following: a higher elastic modulus due to the lithium addition, a higher slip reversibility associated with intense planar slip, and a higher degree of crack deflection and roughness-induced closure [3], when compared with conventional aluminum alloys. Lithium additions to aluminum may increase the elastic modulus by approximately six percent for every weight percent added [4]. However, the moduli of Al-Li-X alloys are sensitive to the phases that are present and, therefore, to the alloy composition and heat treatment. The elastic moduli of Al_3Li , δ' , and Al_2CuLi , T_1 , have been reported to be 97 GPa and 350 GPa, respectively, compared to 70 GPa for pure aluminum [5].

Gayle and coworkers [6] have shown that in the naturally-aged temper the strengthening phases of Weldalite are δ' and GP zones, and, in the artificially aged T6 and T8 tempers, the strengthening phase is T_1 . Unlike other commercially available Al-Li-X alloys, there is little or no δ' present in the T6 and T8 tempers. The δ' and GP zones are known to be coherent and shearable [7], however, there is some controversy concerning the shearability of T_1 [8,9,10]. Shearable precipitates enhance slip reversibility [11] and strain localization which contributes to crack deflection and

roughness-induced closure [12,13,14]. Both effects are potentially beneficial to fatigue crack growth resistance.

This paper describes the monotonic properties and fatigue crack propagation behavior of two tempers of Weldalite: the stretched and naturally-aged T3 temper, and the stretched and artificially-aged T8 temper.

EXPERIMENTAL PROCEDURES

The material used in this study was obtained from Martin Marietta Laboratories in the form of an extruded bar with a 9.5 mm x 102 mm cross section. The composition is given in Table 1. The bar was supplied in the T3 temper with an unrecrystallized microstructure. The T8 temper was attained by heat treating at 433K for 24 hours. Transmission electron microscopy was used to characterize the precipitate structure and deformation behavior of both tempers. Texture studies showed that the Weldalite extrusion had a strong deformation texture containing copper, brass and S components, Figure 1, similar to that which develops in other unrecrystallized Al-Li-X extrusions and rolled plate [15,16].

Tensile tests were performed on a screw driven Instron and a servohydraulic MTS machine. The specimens were machined according to ASTM E8. Samples were taken parallel, transverse and at 45 degrees to the extrusion direction. An initial strain rate of 1.7×10^{-3} /sec was used. Fatigue tests were performed on compact tension specimens, ASTM E647 (W=38 mm, B = 9 mm), using the MTS machine. Samples were tested from the T-L and L-T orientations.

Load shedding was accomplished via computer control, and crack length was monitored using the compliance technique. Intrinsic crack propagation was studied using a decreasing ΔK at constant $K_{max} = 9.5 \text{ MPa m}^{1/2}$ mode of operation [17]. Closure effects were studied using a decreasing ΔK constant load ratio, $R = 0.1$. Optical microscopy was used to characterize crack tortuosity and scanning electron microscopy was used to characterize the fracture surfaces.

RESULTS AND DISCUSSION

Microstructure

The T3 temper is characterized by fine GP zones and δ' particles. These precipitates are extremely small and not easily imaged. Evidence for GP zones includes faint streaks in $\langle 100 \rangle$ reciprocal space directions of selected area diffraction (SAD) patterns. The streaks are continuous, therefore the zones are thought to be GP I. A faint superlattice reflection is also present, which serves as evidence for the existence of δ' in the T3 microstructure.

The T8 microstructure is more complicated. According to Langan and Pickens [18], T_1 is the only strengthening phase present after 24-48 hours at 433K in this family of compositions. In our study, T_1 was the only precipitate that could be imaged, but evidence for the existence of other phases was present in some of the SAD patterns. Specifically, discontinuous streaks were also seen in $\langle 100 \rangle$ reciprocal lattice directions of the (001) pattern indicating the presence of θ' plates. The precipitate structure

of the T8 temper is shown in the bright field TEM of Figure 2.

Monotonic Properties

The tensile properties of the two tempers are shown in Table 2 along with typical values for alloy 2024. Although the properties in the naturally-aged, T3 temper are similar, Weldalite shows a considerable advantage in strength, with comparable elongation, in the T8 temper. No significant difference was observed in the elastic modulus of the T3 and the T8 tempers. The modulus of weldalite was determined to be 79 GPa using the ultrasonic technique [19], compared to 74.6 GPa for 2024. The anisotropy of strength on the extruded Weldalite bar is illustrated in Figure 3. Przystupa et al. [20] demonstrated that for the deformation texture of this alloy, the maximum strength should occur in the longitudinal direction, and the minimum strength should occur between 45 and 60 degrees from the extrusion axis. Our experimental results are consistent with their analysis.

The naturally-aged material deformed by intense localized planar slip, Figure 4a, which occurs in most aluminum alloys that contain shearable precipitates [21], e.g. δ' and GP zones. When aged to the T8 temper, deformation was more homogeneous, Figure 4b. It is unclear from this study whether or not T_1 is sheared; however, slip is fairly homogeneous which indicates that there is no significant loss in strength on the slip plane during deformation.

Jata and Starke [8] showed that intense strain localization occurred in a 2090 alloy, which contains both T_1 and δ'

strengthening precipitates, even after aging for 22 hours at 433K. Their dark field electron micrographs indicated that the T_1 precipitates were sheared in the 2090 alloy. Howe et al. [10] used high resolution electron microscopy to study the structure and deformation behavior of T_1 plates in an Al-2Li-1Cu alloy and showed conclusively that T_1 plates are cut by dislocations during deformation and that such cutting leads to a disruption of nearest-neighbor bonding in the plates. This result differs from the analyses of Sainfort and Guyot [9] which suggest that T_1 plates are not sheared and are bypassed by dislocations. We believe that the shearability of T_1 depends on the presence or absence of other shearable phases, e.g. δ' , and are currently attempting to determine this relationship.

In the T8 temper, fracture appeared to initiate at 40 micron size primary Al_2Cu particles, Figure 5, and propagate along subgrain boundaries. These particles did not appear to play a significant role in the fracture process of the naturally-aged material which was transgranular.

Cyclic Properties

Intrinsic fatigue crack growth rates are shown in Figures 6a and 6b, along with crack growth rates at $R = 0.1$. The T3 and T8 tempers showed intrinsic thresholds of $\Delta K = 2.0 \text{ MPa } m^{1/2}$ ($R = 0.79$), and $\Delta K = 1.3 \text{ MPa } m^{1/2}$ ($R = 0.86$), respectively. In both tempers, there was virtually no difference between the data generated for the T-L and L-T orientations. The T8 temper has an intrinsic

fatigue resistance similar to the 2XXX series alloys and slightly superior to the conventionally processed 7XXX alloys. The T3 temper has a higher intrinsic fatigue resistance than conventionally processed aluminum alloys. The curves generated in this study can be compared to those for commercial alloys presented in Figure 7.

In order to explain these results, the mechanism of damage accumulation must be investigated. Plastic strain is accumulated by slip ahead of the crack tip. The T3 temper contains shearable coherent precipitates that allow for eased slip reversibility as discussed by Hornbogen and Zum Gahr [11]. The dislocations can glide in both directions on the slip plane with ease due to decreased resistance from sheared precipitates and the fact that precipitate shearing enhances planar slip. Planar slip often leads to crack branching and crack deflection [12,13], and a significant amount of branching and deflection was observed for the T3 temper. These avenues for energy release reduce the driving force for crack propagation, which partially explains the unusually high intrinsic threshold measured for the T3 temper. The T8 condition contains a fine dispersion of T_1 plates and deforms in a predominately homogeneous manner. Dislocation looping mechanisms, tangles, and cross slip associated with near-homogeneous deformation hinders slip reversibility. This situation leads to a higher accumulation of plastic strain in the T8 temper for the same number of cycles [22]. Therefore, the T8 material should exhibit faster crack growth than the T3 material at any given ΔK , which is observed

experimentally. Although the effect of environment on the fatigue crack propagation behavior was not evaluated in this study, it is well-known that strain localization increases environmental sensitivity in age hardenable aluminum alloys [23]. This effect is normally associated with a hydrogen embrittlement mechanism for corrosion fatigue which relates the degree of susceptibility to slip planarity [24-26]. However, the surface oxide film which forms in air also hinders slip reversibility [22]. In either case, one would expect that the T3 temper would be more environmentally sensitive than the T8 temper and that the T3 temper would show an even larger crack growth resistance, compared with the T8 temper, in vacuum.

In addition to contributing to intrinsic crack growth rates, the deformation mode determines the amount of extrinsic shielding mechanisms such as roughness-induced closure. The planar slip microstructure of the T3 temper makes a significant contribution to extrinsic effects by causing crack branching, crack deflection, and fracture surface roughness. Fracture occurred along slip bands, and an optical micrograph of the tortuous crack path is shown in Figure 8a. SEM analysis indicated that branching and deflection occurred throughout the specimen thickness. All of these effects reduce the ΔK experienced at the crack tip and thus reduce the driving force for crack propagation. The role of crack deflection as an extrinsic shielding mechanism was investigated using equations developed by Suresh [13]. The ΔK at the deflected crack tip was found to be 2% lower than the nominal value, and the

fatigue crack growth rate was found to be 4% lower than for an undeflected crack. These results suggest that crack deflection does not significantly affect the crack propagation rate. Therefore, the high intrinsic threshold measured for the T3 temper must be attributed to either slip reversibility, closure (even at high R), or crack branching. Since the T3 temper has a high level of roughness-induced closure, some permanent mode II displacement must occur, i.e., complete slip reversibility does not take place during unloading. As shown in Figure 8a, the T3 specimens exhibited tortuous crack paths. In the presence of Mode II displacements, crack tip openings are not large enough to assure closure-free testing even at high R, e.g. 0.8. Consequently, the high threshold is most likely associated with crack branching and closure. Although these are considered extrinsic shielding mechanisms, they are caused by the deformation mode of the alloy which is controlled by the microstructure.

Closure effects in the T8 temper are small, as would be expected from its deformation behavior. Figure 8b shows the straight crack profile associated with the T8 temper. Fracture was predominately intersubgranular, and there were no mechanisms for energy release other than the extension of the crack perpendicular to the loading direction. Fatigue crack profiles shown in Figure 8 are representative of both constant K_{max} and $R = 0.1$ test conditions.

Figure 9 is a direct comparison of near threshold fatigue crack growth rates for Weldalite-T3 and 2024-T3 [17]. The enhanced crack growth resistance of Weldalite under constant K_{max} and $R =$

0.1 conditions cannot be attributed to the 6% improvement in elastic modulus and is most likely associated with extrinsic effects such as crack branching. Weldalite may have a higher propensity for planar slip and slip reversibility due to the presence of δ' ; however, it seems logical to credit branching and closure effects for most of the improvement in resistance to fatigue crack growth compared to 2024-T3.

CONCLUSIONS

- Weldalite deforms by intense, localized, planar slip in the T3 temper. Deformation is much more homogeneous in the T8 temper indicating that the T₁ precipitates may be difficult to shear in the absence of shearable precipitates such as δ' .
- The strength of Weldalite-T3 is comparable to 2024-T3 but Weldalite-T8 is much stronger than 2024-T8, having a yield strength of 700 MPa. The anisotropy in tensile properties is due to the presence of an intense deformation texture similar to other unrecrystallized Al-Li-X alloys.
- The fatigue crack growth resistance of Weldalite-T3 is higher than that of 2024-T3. The improvement is most likely associated with a larger degree of crack branching and closure. The fatigue crack growth resistance of Weldalite-T8 is similar to conventionally processed 2024-T8.

ACKNOWLEDGEMENTS

This work was sponsored by the U.S. Air Force Office of Scientific Research under contract no. 87-0082-B, Dr. Alan B.

Rosenstein, Program Monitor. The authors would like to thank Martin Marietta Laboratories, especially Drs. Joseph Pickens and Frank Heubaum, for supplying the materials. Mr. Gary Bray and Dr. Richard Gangloff are also gratefully acknowledged for helpful discussions and assistance during fatigue testing.

REFERENCES

1. J.R. Pickens, F.H. Heubaum, T.J. Langan and L.S. Kramer (1989) Al-(4.5-6.3)Cu-1.3Li-0.4Ag-0.4Mg-0.14Zr Alloy Weldalite™ 049. *Aluminum-Lithium Alloys V* (edited by T.H. Sanders, Jr. and E.A. Starke, Jr.), Vol. III, 1397-1414. MCE Publications Ltd., Birmingham, UK.
2. K.T.V. Rao, R.S. Piascik, R.P. Gangloff and R.O. Ritchie (1989) Fatigue Crack Propagation in Aluminum-Lithium Alloys. *Aluminum-Lithium Alloys V* (edited by T.H. Sanders, Jr. and E.A. Starke, Jr.), Vol. II, 955-971. MCE Publications Ltd., Birmingham, UK.
3. E.J. Coyne, T.H. Sanders, Jr. and E.A. Starke, Jr. (1981) The Effect of Microstructure and Moisture on the Low Cycle Fatigue and Fatigue Crack Propagation of Two Al-Li-X Alloys. *Aluminum-Lithium Alloys* (edited by T.H. Sanders, Jr. and E.A. Starke, Jr.), 293-305. AIME, Warrendale, PA.
4. K.K. Sankaran and N.J. Grant (1981) Structure and Properties of Splat Quenched 2024-Aluminum Alloy Containing Lithium Additions. *Aluminum-Lithium Alloys* (edited by T.H. Sanders, Jr. and E.A. Starke, Jr.), 205-227. AIME, Warrendale, PA.

5. M.E. O'Dowd, W. Ruch and E.A. Starke, Jr. (1987) Dependence of Elastic Modulus on Microstructure in 2090-Type Alloys. *4th International Aluminum-Lithium Conference* (edited by G. Champier, B. Dubost, D. Miannay, L. Sabetay), C3-565-C3-576. Les Editions de Physique, Les Ulis, France.
6. F.W. Gayle, F.H. Heubaum and J.R. Pickens (1989) Natural Aging and Reversion Behavior of Al-Cu-Li-Ag-Mg Alloy WeldaliteTM 049. *Aluminum-Lithium V* (edited by T.H. Sanders, Jr. and E.A. Starke, Jr.), Vol. II, 701-710. MCE Publications Ltd., Birmingham, UK.
7. T.H. Sanders, Jr. and E.A. Starke, Jr. (1982) The Effect of Slip Distribution on the Monotonic and Cyclic Ductility of Al-Li Binary Alloys. *Acta Metall.* **30**, 927-939.
8. K.V. Jata and E.A. Starke, Jr. (1986) Fatigue Crack Growth and Fracture Toughness Behavior of an Al-Li-Cu Alloy. *Metall. Trans. A* **17A**, 1011-1026.
9. P. Sainfort and P. Guyot (1986) Fundamental Aspects of Hardening in Al-Li and Al-Li-Cu Alloys. *Aluminum-Lithium Alloys III* (edited by C. Baker, P.J. Gregson, S.J. Harris and C.J. Peel), 420-426. The Institute of Metals, London.
10. J.M. Howe, J. Lee and A.K. Vasudevan (1988) Structure and Deformation Behavior of T₁ Precipitate Plates in an Al-2Li-1Cu Alloy. *Metall. Trans. A* **19A**, 2911-2920.
11. E. Hornbogen and K.H. Zum Gahr (1976) Microstructure and Fatigue Crack Growth in a γ -Fe-Ni-Al Alloy. *Acta Metall.* **24**, 581-592.

12. F.S. Lin and E.A. Starke, Jr. (1980) The Effect of Copper Content and Degree of Recrystallization on the Fatigue Resistance of 7XXX-Type Aluminum Alloys - Part II. Fatigue Crack Propagation. *Mater. Sci. and Engng.* **43**, 65-76.
13. S. Suresh (1983) Crack Deflection: Implications for the Growth of Long and Short Fatigue Cracks. *Metall. Trans. A* **14A**, 2375-2385.
14. S. Suresh (1985) Fatigue Crack Deflection and Fracture Surface Contact: Micromechanical Models. *Metall. Trans. A* **16A**, 249-260.
15. A.K. Vasudevan, W.G. Fricke, Jr., R.C. Malcolm, R.J. Bucci, M.A. Przystupa and F. Barlat (1988) On Through Thickness Crystallographic Texture Gradient in Al-Li-Cu-Zr Alloy. *Metall. Trans. A* **19A**, 731-732.
16. M.J. Bull and D.J. Lloyd (1986) Textures Developed in Al-Li-Cu-Mg Alloy. *Aluminum-Lithium Alloys III* (edited by C. Baker, P.J. Gregson, S.J. Harris, C.J. Peel), 402-410. The Institute of Metals, London.
17. W.A. Herman, R.W. Hertzberg, and R. Jaccard (1988) A Simplified Laboratory Approach for the Prediction of Short Crack Behavior in Engineering Structures. *Fatigue Fract. Engng. Mater. Struct.* **11**, No. 4, 303-320.
18. T.J. Langan and J.R. Pickens (1989) Identification of Strengthening Phases in Al-Cu-Li Alloy Weldalite™ 049. *Aluminum-Lithium V* (edited by T.H. Sanders, Jr. and E.A. Starke, Jr.), Vol. II, 691-700. MCE Publications Ltd., Birmingham, UK.

19. Frank Heubaum (1989) Martin Marietta Laboratories, Baltimore, MD, private communication.
20. M.A. Przystupa, A.K. Vasudevan and W.G. Fricke, Jr. (1988) Application of the Relaxed Constraints Model to the Prediction of Plastic Anisotropy. *Eighth International Conference on Textures of Metals* (edited by J.S. Kallend and G. Gottstein), 1051-1057.
21. J.M. Duva, M.A. Daeubler, E.A. Starke, Jr. and G. Luetjering (1988) Large Shearable Particles Lead to Coarse Slip in Particle Reinforced Alloys. *Acta Metall.* **36**, 585-589.
22. E.A. Starke, Jr. and J.C. Williams (1989) Microstructure and the Fracture Mechanics of Fatigue Crack Propagation. *Fracture Mechanics: Perspectives and Directions, ASTM STP 1020* (edited by R.P. Wei and R.P. Gangloff), 184-205. ASTM, Philadelphia, PA.
23. F.S. Lin and E.A. Starke, Jr. (1980) Mechanisms of Corrosion Fatigue Crack Propagation of 7XXX Aluminum Alloys in Aqueous Environments. *Hydrogen Effects in Metals* (edited by I.M. Bernstein and A.W. Thompson), 485-492. AIME, Warrendale, PA.
24. J.A. Donovan (1976) Accelerated Evolution of Hydrogen from Metals During Plastic Deformation. *Metall. Trans.* **7A**, 1677-1683.
25. M.R. Louthan, Jr., G.R. Caskey, Jr., J.A. Donovan, and D.E. Rawl, Jr. (1972) Hydrogen Embrittlement of Metals. *Mater. Sci. and Engng.* **10**, 357-368.
26. R.P. Wei (1987) Environmentally Assisted Fatigue Crack Growth. *Fatigue '87* (edited by R.O. Ritchie and E.A. Starke, Jr.), Vol. 3, 1541-1560. EMAS, West Midlands, United Kingdom.

TABLE 1. ALLOY COMPOSITION (wt%)

Cu	Li	Mg	Ag	Zr
5.0	1.3	0.4	0.4	0.1

TABLE 2. TENSILE PROPERTIES

	YS (MPa)	UTS (MPa)	EL(%)
T3	379	496	15
T8	683	703	5
2024-T3*	350	490	18
2024-T8*	420	455	6

*From Aluminum, Standards and Data, the Aluminum Association, 1984.

LIST OF FIGURES

Figure 1. (111) pole figure of Weldalite extrusion. Copper, brass, and S texture components are present.

Figure 2. Bright field TEM micrograph of Weldalite in T8 condition. T₁ plates are present in matrix and along subgrain boundaries; Zone Axis [112].

Figure 3. Yield and tensile strengths of Weldalite T3 (a) and T8 (b) at 0, 45, and 90 degrees to the extrusion direction.

Figure 4. TEM micrograph of T3 (a) and T8 (b) after 2% plastic strain in tension.

Figure 5. SEM micrograph of T8 tensile test fracture surface. Large constituents are primary particles from casting.

Figure 6. Fatigue crack growth rates for T3 (a) and T8 (b) tempers, constant K_{max} and $R = 0.1$.

Figure 7. Fatigue crack growth rates for Al-Li-X and commercial alloys under high R conditions (Rao et al., ref. 2).

Figure 8. Fatigue crack profiles for T3 (a) and T8 (b) tempers, constant K_{max} . Taken from regions of low ΔK .

Figure 9. Near threshold fatigue crack growth rates of Weldalite T3 compared to 2024-T3 (after W.A. Herman et al., ref. 17), constant K_{max} and $R = 0.1$.

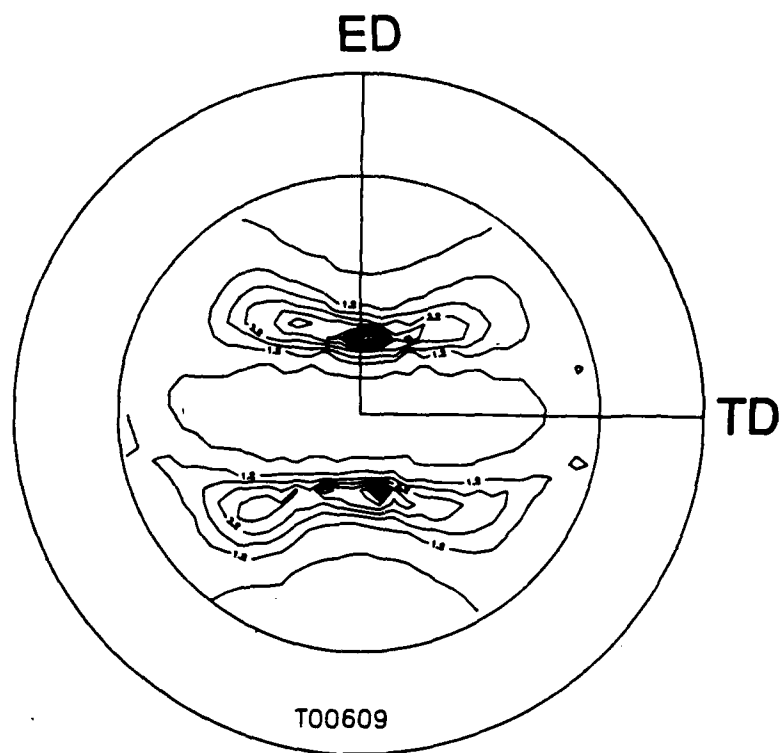


Figure 1. (111) pole figure of Weldalite extrusion. Copper, brass, and S texture components are present.

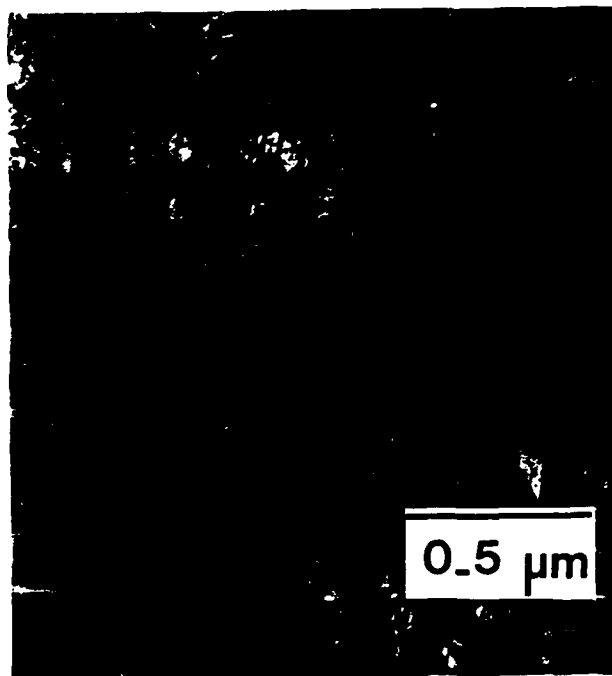


Figure 2. Bright field TEM micrograph of Weldalite in T8 condition. T_1 plates are present in matrix and along subgrain boundaries; Zone Axis $[112]$.

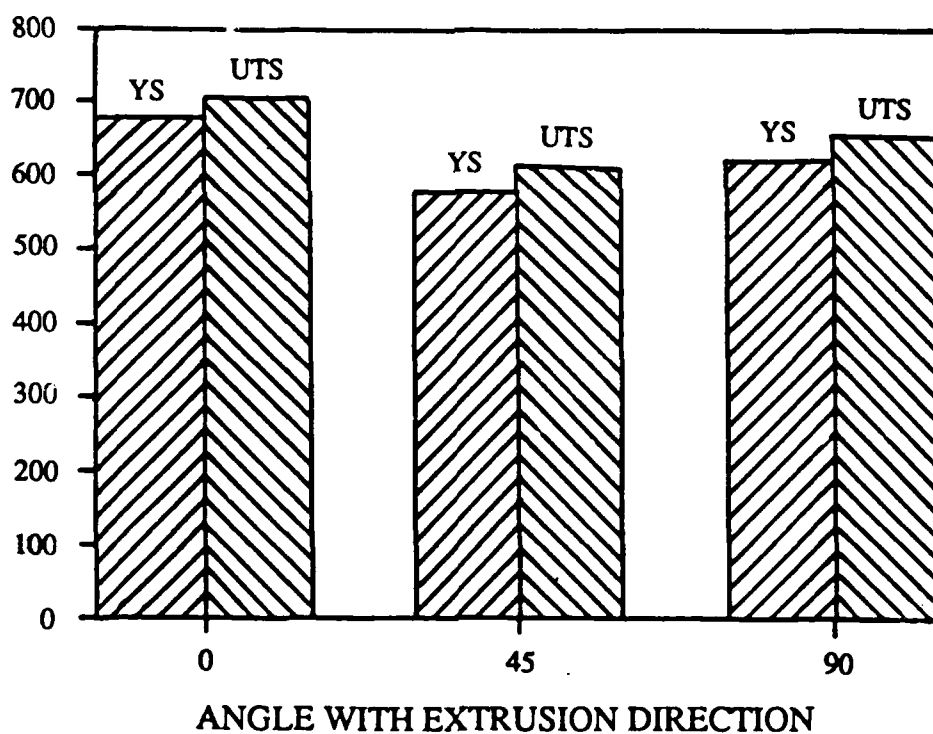
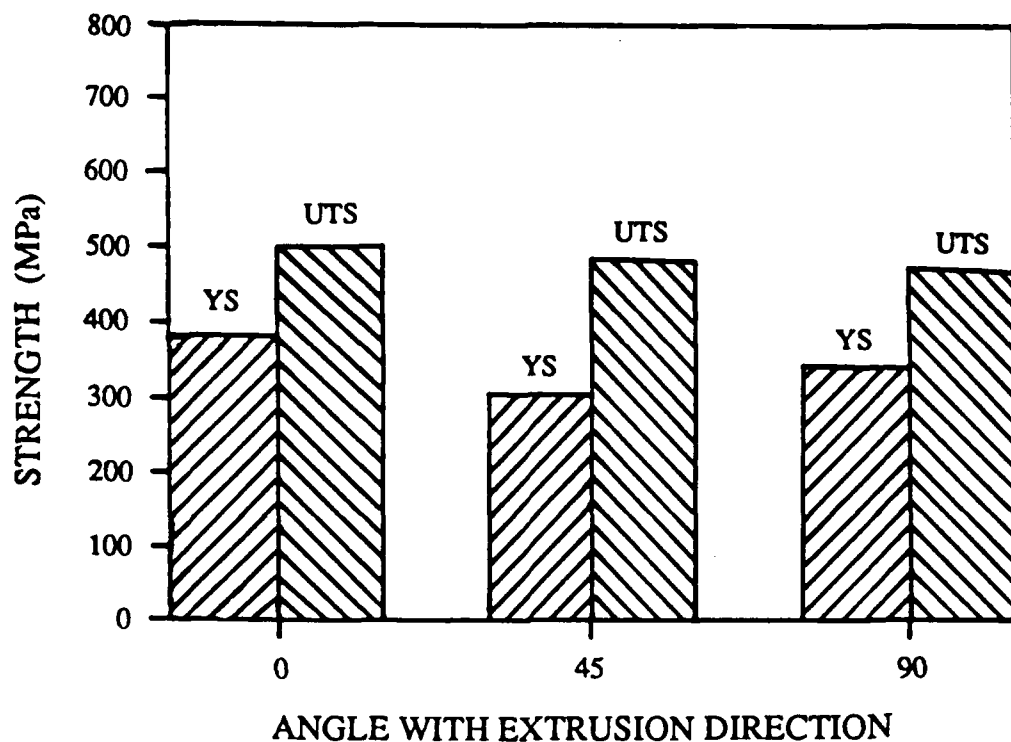


Figure 3. Yield and tensile strengths of Weldalite T3 (a) and T8 (b) at 0, 45, and 90 degrees to the extrusion direction.



Figure 4. TEM micrograph of T3 (a) and T8 (b) after 2% plastic strain in tension.

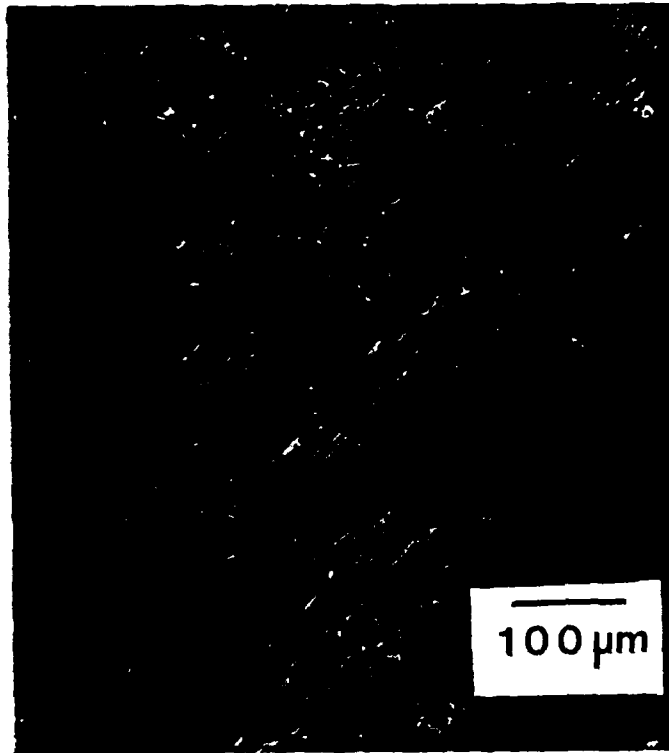


Figure 5. SEM micrograph of T8 tensile test fracture surface.
Large constituents are primary particles from casting.

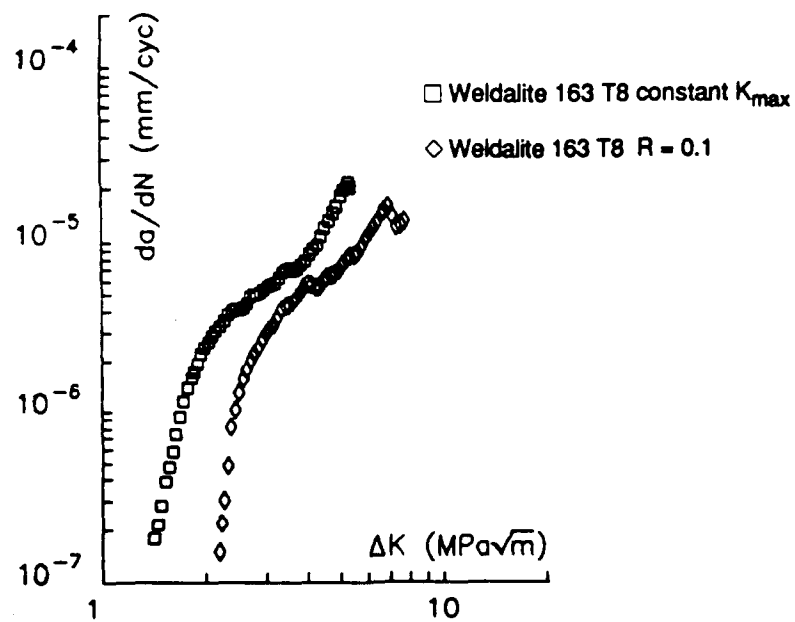
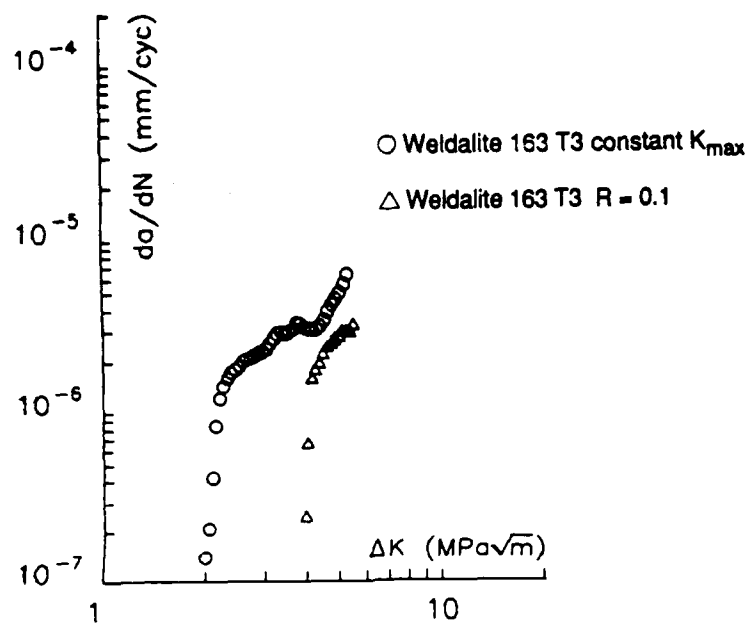


Figure 6. Fatigue crack growth rates for T3 (a) and T8 (b) tempers, constant K_{max} and $R = 0.1$.

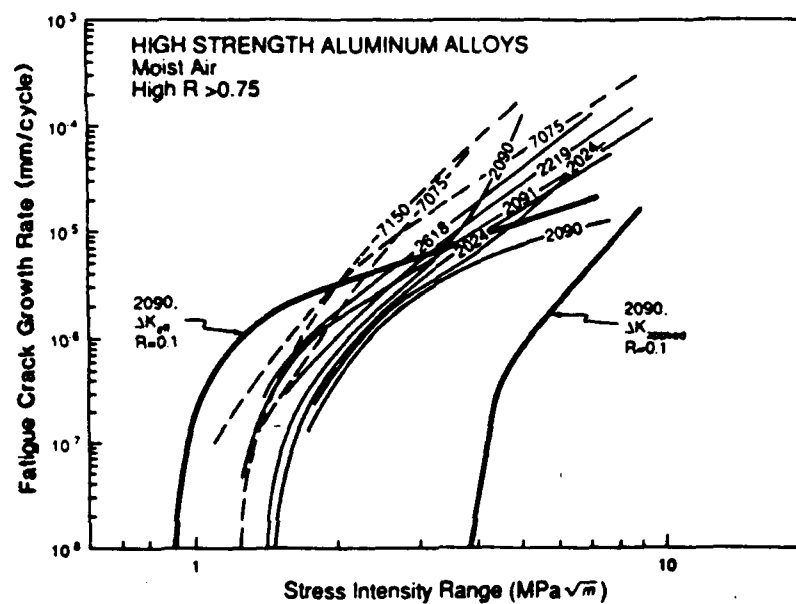
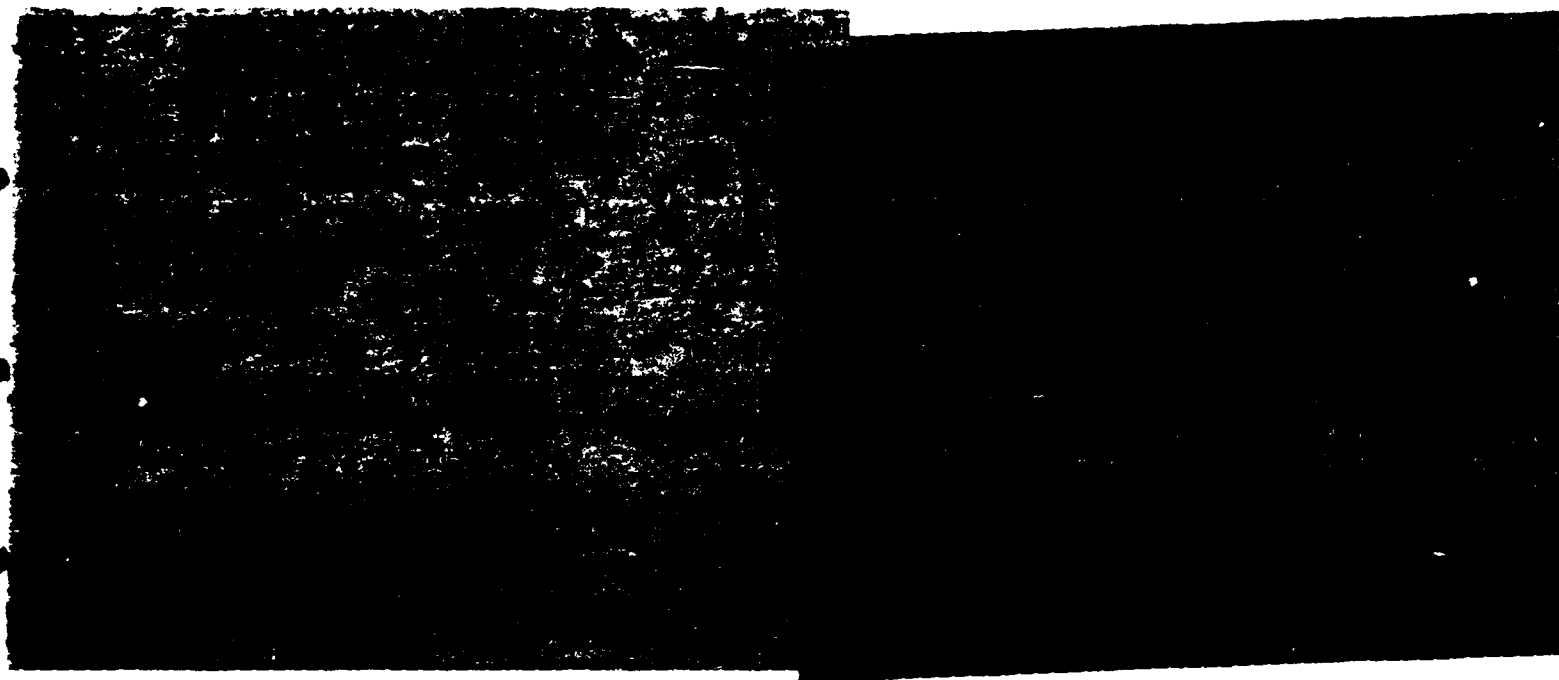


Figure 7. Fatigue crack growth rates for Al-Li-X and commercial alloys under high R conditions (Rao et al., ref. 7).



(a)

Figure 8. Fatigue crack profiles for T3 (a) and T8 (b) tempers, constant K_{max} . Taken from regions of low ΔK .



(b)

Figure 8. Fatigue crack profiles for T3 (a) and T8 (b) tempers, constant K_{max} . Taken from regions of low ΔK .

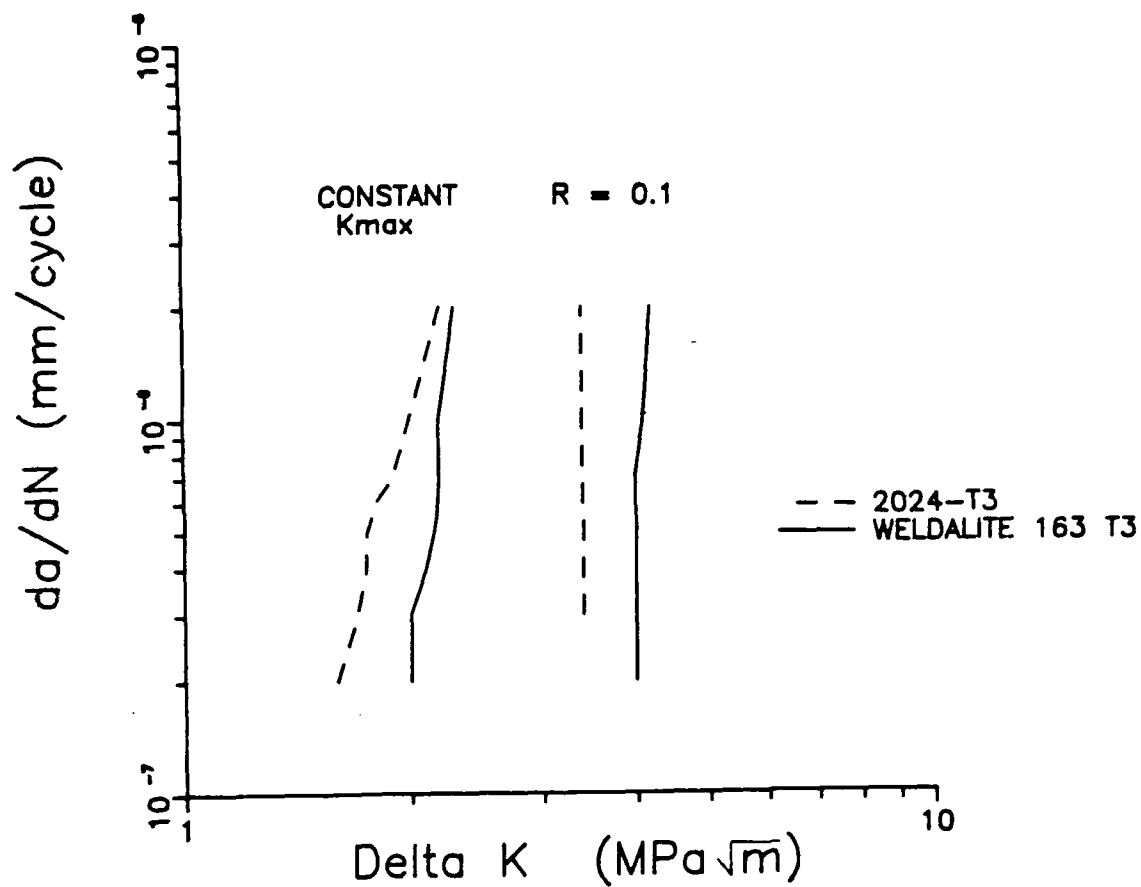


Figure 9. Near threshold fatigue crack growth rates of WELDALITE T3 compared to 2024-T3 (after W.A. Herman et al., ref. 17), constant K_{max} and $R = 0.1$.

Mechanisms of Continuous Recrystallization in an Al-Zr-Si Alloy

Halldor Gudmundsson⁺, Douglas Brooks, and John A. Wert

Department of Materials Science
University of Virginia
Charlottesville, VA 22901

⁺ Present address:
Technological Institute of Iceland
IS-112 Keldnaholt
Iceland

ABSTRACT

Microstructural evolution in an Al-Zr-Si alloy has been investigated with the goal of elucidating the mechanisms responsible for formation of high-angle grain boundaries by continuous, recovery-type processes during concurrent straining and annealing. The primary method of investigation was TEM characterization of the microstructure and microtexture after cold rolling, after annealing, and after concurrent straining and annealing. The cold-rolled microstructure consists of layers parallel to the rolling plane; only low-angle boundaries are present within each layer while adjacent layers are separated by high-angle boundaries. During annealing, the subgrain size increases but the subgrain boundary misorientations are not significantly changed and the high-angle boundaries are relatively immobile. In contrast, concurrent straining and annealing of the cold-rolled material causes a gradual increase in the misorientation of some of the original low-angle boundaries, implying subgrain rotation. Ultimately, high-angle boundaries evolve by subgrain rotation from the subgrain boundaries originally present within each layer. The observations are interpreted in terms of several mechanisms previously proposed for microstructural evolution during concurrent straining and annealing.

1. INTRODUCTION

Microstructures composed predominately of grains separated by high-angle boundaries have been reported to form by continuous processes during annealing of cold- or warm-rolled, particle-bearing aluminum alloys [1-17]. The major deformation texture components are not sharply altered by this relaxation process; rather, they become gradually more diffuse as relaxation progresses [1,5,8,15]. The continuous relaxation process is evidently not conventional discontinuous recrystallization which proceeds via migration of high-angle boundaries; however, the resulting microstructure has the characteristics of a recrystallized microstructure. The terms "in situ recrystallization" and "continuous recrystallization" [1] have been used for the relaxation mechanisms that produce predominately high-angle boundaries by continuous, recovery-type processes. The majority of observations of continuous recrystallization have been made in cases where an alloy is initially rolled at cold- or warm-working temperatures to introduce a deformation substructure, and is subsequently subjected to concurrent annealing and slow strain rate deformation at a higher temperature [2-17].

Although several commercial superplastic aluminum alloys rely on continuous recrystallization to provide the fine grain size that confers superplastic characteristics [18-21], the mechanisms of microstructural evolution during continuous recrystallization are incompletely understood. Gaining a basic understanding of continuous recrystallization appears to hinge on several fundamental issues including identifying the mechanism that allows development of predominately high-angle boundaries by continuous, recovery-type processes and establishing whether straining concurrently with annealing is essential to continuous recrystallization.

Alborn, Hornbogen and Koster [1] observed microstructures they termed continuously recrystallized in cold rolled and annealed Al-Cu alloys. However, evidence for the presence of high-angle boundaries after annealing was limited to TEM observations of fringe contrast from boundaries. It is now well-recognized that boundaries with misorientations greater than about 1° normally exhibit fringe contrast unless special diffracting conditions are used to image the strain fields associated with individual dislocations that compose the boundary [22]. Thus, it is likely that the boundaries observed by Alborn et al. were predominately subgrain boundaries rather than grain boundaries. This is the only report of continuous recrystallization during annealing without concurrent strain.

Bricknell and Edington [4,5] investigated microstructure evolution during annealing and during concurrent straining and annealing in a commercial superplastic Al-Cu-Zr alloy using TEM and x-ray methods. Texture results provided firm evidence that the mechanism responsible for formation of high-angle boundaries during concurrent straining and annealing was not discontinuous recrystallization. These investigators proposed that processes such as subgrain boundary dissociation and coalescence could lead to formation of high-angle boundaries, which would then allow grain rotation during subsequent superplastic deformation.

Nes [6-8] reported on continuous recrystallization during concurrent straining and annealing of a commercial superplastic Al-Cu-Zr alloy and an Al-Mn-Zr alloy. He proposed that high-angle boundaries appear as a consequence of rapid subgrain growth during concurrent annealing and straining. The misorientation of a boundary was considered to accumulate linearly with

boundary migration distance. Thus, a high-angle boundary could evolve from a subgrain boundary, provided the subgrain boundary migrated a sufficient distance. In this view, the role of straining is acceleration of subgrain boundary migration, which allows high-angle boundaries to form in cases where subgrain growth during static annealing would be too slow to produce sufficient subgrain boundary migration to develop high-angle boundaries.

McNelly and coworkers [9-15] have published a series of papers describing observations of continuous recrystallization in Al-Mg alloys. Measurements of boundary misorientations have led these investigators to conclude that continuous recrystallization requires that at least part of the strain be accommodated by grain boundary sliding, even though the observed boundary misorientations at the start of concurrent straining and annealing are lower than those found to slide extensively in bicrystal experiments [23-26]. McNelly et al. assert that boundaries with initial misorientations in range 5° - 7° may be able to slide sufficiently to cause gradual grain rotation which would increase the average boundary misorientation.

Recently, Watson and Bennetch [17] reported that superplastic deformation of Al-Li-Cu-Zr and Al-Li-Cu-Mg-Zr alloys caused a large increase in average boundary misorientation as well as an increase in subgrain size. They proposed links between the boundary misorientations in the initial subgrain structure and solute drag from Li atoms in solid solution, and between continuous recrystallization and dynamic precipitation of Al_6Li_3Cu particles. These aspects of continuous recrystallization have not been noted by previous investigators for other alloy systems. While it is possible that the presence of Li in aluminum alloys introduces new microstructural

interactions, the salient aspects of continuous recrystallization in Al-Li-Cu-(Mg)-Zr alloys appear similar to those observed in other alloys, leaving many open questions about the interactions described by Watson and Bennetch.

With the exception of Bricknell and Edington [4,5], all previous investigators derived their conclusions about the mechanism of continuous recrystallization from TEM observations of foils oriented parallel to the rolling plane of the sheet. (Foil orientation is not explicitly stated in many of the publications but private communication with the authors has confirmed the rolling-plane foil orientations.) Bricknell and Edington used samples with the foil normals equally inclined to the longitudinal, long transverse and short transverse directions (L, T, and S directions, respectively). However, recent investigations have shown that some elements of deformation and annealing microstructures are not readily characterized using foils oriented parallel to the rolling plane [28-34]. This suggests that examination of continuous recrystallization using TEM foils oriented normal to the T direction could provide new insights into the basic mechanisms of the continuous recrystallization process.

The present investigation was undertaken to examine microstructural evolution in an Al-Zr-Si alloy during annealing and concurrent straining and annealing. TEM has been used for microstructure and microtexture characterization, and the microtexture results have been compared with bulk x-ray texture measurements. All TEM observations were performed using foils oriented normal to the T direction. The alloy composition was chosen to incorporate Al_3Zr dispersoid particles which provide boundary drag pressure that suppresses discontinuous recrystallization at intermediate annealing

temperatures [6-8,35-37]. The absence of precipitation-hardening alloy additions avoids complications associated with precipitation of these particles during cooling from the annealing temperature.

2. EXPERIMENTAL METHODS

The alloy investigated in this study was an Al-Zr-Si alloy with composition: 0.24 wt% Zr, 0.1 wt% Si, 0.01 wt% Fe. The Al-Zr-Si alloy was direct chill cast by Reynolds Metals Co. as an ingot with 200 x 73 mm cross-section. Previous investigations have shown that small additions of Si to Al-Zr alloys promote formation of a more uniform dispersion of Al_3Zr particles [35-37]; thus, Si is an intentional alloying addition.

Very few primary Al_3Zr particles were observed near the edges of the casting; considerably more were present in the center. Specimens with 11 x 15 mm cross-section and approximately 60 mm in length were cut from the edge of the ingot to avoid regions where primary Al_3Zr particles had formed. The specimens were heated at a rate of 50 K/h to 723 K where they were held for 8 h to precipitate Al_3Zr . Following heat treatment, the Al-Zr-Si specimens were cold rolled in increments of 10% of the original thickness to a total reduction of thickness of 90% (effective strain, $\epsilon_{\text{eff}} = 2.6$). To inhibit recovery, the specimens were cooled with water after each rolling pass and were stored in a freezer while awaiting observation.

Annealing was performed in an air furnace; specimens were inserted into the furnace at the desired temperature. Concurrent straining and annealing was carried-out using tensile specimens machined from the cold-rolled sheet

with the tensile axis parallel to the L direction of the rolled sheet. The tensile specimens were strained at constant crosshead velocity using an Instron machine equipped with a three-zone furnace. The specimens reached the testing temperature in about 1 hour and were stabilized at that temperature for 0.33 hour prior to testing. The tensile testing apparatus allowed quick removal and water quenching of the tensile specimens after straining. Some tensile specimens were strained to failure while other tests were interrupted to provide samples for microstructural analyses at intermediate strains.

Microstructure characterization was performed for homogenized, cold-rolled, annealed, and concurrently strained and annealed conditions. TEM foils oriented normal to the T direction were removed from treated samples and were electropolished in a 1:3 nitric acid - methyl alcohol solution at 248 K. Grain orientation measurements were accomplished in the TEM using the following technique. The specimen was inserted into the holder with the L direction parallel to the holder axis and the specimen was not tilted while in the microscope. The microscope was operated in a convergent beam mode to produce strong Kikuchi patterns, which were recorded from many adjacent grains. For each grain, a computer program was used to digitize the Kikuchi pattern and to calculate a rotation matrix describing the relationship between the crystal axes and the diffraction pattern [38,39]. Matrix methods were then used to find the orientations of the 111 poles for each grain, allowing a micro-pole figure to be plotted for groups of grains. The rotation matrix methods also allowed misorientation axis-angle pairs to be determined for adjoining grains [40-42].

X-ray texture measurements were performed using the Schultz reflection

method [43,44] with defocusing correction factors calculated using the method of Gale and Griffiths [45]. Texture specimens were ground and polished to a 600-grit surface finish prior to electropolishing (15 V, 120 s) in a 1:3 nitric acid - methyl alcohol solution at 248 K.

3. RESULTS

3.1 Microstructure Before Rolling

TEM observation of heat treated samples revealed the presence of spherical, coherent Al_3Zr particles. The projected particle diameter was measured for 300 particles, giving an average diameter of 4.7 (± 0.5) nm. TEM observations showed the Al_3Zr particle distribution to be nonuniform, an effect that may be associated with segregation of Zr and/or Si during solidification.

3.2 Microstructure and Texture After Cold Rolling

Optical metallography of the cold-rolled Al-Zr-Si alloy revealed an inhomogeneous microstructure, an example of which is shown in Figure 1. (The L direction is parallel to the scale marker and the T direction is normal to the plane of all micrographs presented in this paper.) A few regions near the center of the micrograph have suffered less deformation than the surrounding material, and the adjacent material appears to have flowed around these "hard" regions during rolling.

The nonuniform character of the deformation microstructure is also apparent from TEM observations. In most regions, a well-defined, blocky microstructure formed during rolling, as shown in the lower right portion of

Figure 2a and in greater detail in Figure 2b. Previous investigators have used the term "subgrain structure" in reference to this microstructure [32,46], which they observed to replace the microband structure present at lower rolling strains. The subgrain-type of deformation microstructure is commonly observed in aluminum alloys cold rolled to strains greater than 2.

In contrast, other regions of the cold-rolled alloy exhibit a more uniform deformation microstructure. For example, in the upper left portion of Figure 2a, the dislocations introduced during rolling have not formed a subgrain structure. The density of Al_3Zr particles was observed to be higher in regions where the dislocations are uniformly distributed than in the regions where subgrains have formed. The morphology and size of the regions of uniform dislocation distribution observed in the TEM samples suggest that they correspond to the "hard" regions observed by optical metallography. The volume fraction of material containing a uniform distribution of dislocations is lower than that containing subgrains. The regions containing a uniform dislocation distribution will not be considered further in the present paper.

Since some of the boundaries between subgrains may eventually evolve into grain boundaries during continuous recrystallization, characterization of the lattice orientation within subgrains and the subgrain boundary misorientations provides a basis for understanding microstructure evolution during subsequent annealing. Figure 3 is a boundary misorientation map; i.e., a montage of bright-field TEM micrographs with boundary misorientations indicated in degrees. (On all grain boundary misorientation maps, 6° misorientations are underlined while 9° misorientations are not underlined.) This figure shows that the majority of boundaries are low-angle boundaries,

but that some boundaries in the deformation microstructure have high misorientation angles. In the present paper, boundaries with less than 10^0 misorientation are termed "low-angle" or "subgrain" boundaries and boundaries with greater than 10^0 misorientation are termed "high-angle" or "grain" boundaries. Choice of the critical value is arbitrary to some extent, but 10^0 is convenient because boundary sliding experiments with bicrystals have shown that significant boundary sliding is possible for misorientations greater than 10^0 [23-27]. All of the high-angle boundaries in Figure 3 are oriented parallel to the rolling plane, whereas all of the transverse boundaries (i.e., boundaries parallel to the S direction) are of low-angle character.

The boundary misorientation map in Figure 3 and similar maps from 2 other regions in the cold-rolled alloy show that the subgrain structure may be considered as a layered structure with the layers oriented parallel to the rolling plane. Only low-angle boundaries are present within each layer, but the layers are separated by high-angle boundaries. The subgrain boundaries within a layer may have any orientation, but a majority are oriented either parallel or normal to the rolling plane. The average subgrain dimension is approximately $0.3\ \mu\text{m}$ in the S direction and $1\ \mu\text{m}$ in the L direction. The range of subgrain sizes observed throughout the specimen is not appreciably greater than the range displayed in Figure 3.

The layers are separated by high-angle boundaries. TEM results indicate that the spacing of high-angle boundaries in the deformation microstructure of this Al-Zr-Si alloy is highly variable. In the region shown in Figure 3, the spacing of high-angle boundaries along the S direction is on the order of $2\ \mu\text{m}$, whereas similar analyses in other regions reveal a high-angle boundary

spacing greater than 10 μm . No obvious differences in the appearance of the subgrain microstructure in bright field micrographs were noted between regions of widely varying high-angle boundary spacing.

Figure 4a shows a partial 111 pole figure representing the bulk texture at the mid-thickness location in the rolled sample. The bulk texture is a characteristic cold-rolling texture for pure Al which contains superposed $\{112\}\langle 11\bar{1}\rangle$, $\{123\}\langle 41\bar{2}\rangle$ and $\{110\}\langle 1\bar{1}2\rangle$ texture components [44].

The 111 poles associated with crystal orientations in the subgrains can be plotted on a micro-pole figure. Figure 4b shows such a micro-pole figure which represents the subgrain orientations from Figure 3. Interactive comparison of subgrain orientation and subgrain location reveals that subgrains within each layer have very similar orientations, consistent with the low boundary misorientation angles, and that each group of subgrain orientations in the micro-pole figure represents a layer which is separated from adjoining layers by high-angle boundaries. Figure 4c shows subgrain orientations in a different region of the cold-rolled sample. Strong differences between the micro-pole figures from two regions that have essentially identical microstructures show that inhomogeneity of the deformation microstructure extends beyond characteristics such as subgrain size and dislocation density. Furthermore, comparison of the micro-pole figures with the bulk pole figure for the cold-rolled alloy shows that some subgrain orientations in the regions used to obtain the micro-pole figures are representative of the bulk texture, whereas other subgrain orientations are not. These texture differences could arise as a result of differences in initial grain orientation, or other factors associated with the inhomogeneous

microstructure of the rolled material. However, irrespective of subgrain orientation relative to the axes of the bulk sample, the grouping of subgrain orientations into layers parallel to the rolling plane is a consistent feature of all regions in which subgrain orientations were analyzed.

3.2 Microstructure and Texture After Annealing

The cold-rolled alloy was annealed at 623, 648, and 673 K for periods up to 72 h. In accord with results from previous investigators [35-37], the Al_3Zr dispersoid particles substantially increase resistance to discontinuous recrystallization compared to high-purity and commercial-purity aluminum. However, after annealing for 8 h at 673 K, some discontinuously recrystallized grains were observed by optical metallography.

Figure 5 shows boundary misorientation maps for three annealing conditions. After 8 h at 623 K, the dislocation density within the subgrains is reduced and the boundary appearance is sharper, suggesting that statistically-stored dislocations have been eliminated. In addition, the subgrain size is larger in some regions than the largest subgrains observed in the cold-rolled material, indicating that some subgrain growth occurred during this annealing treatment. Figure 5b shows that increasing the annealing time at 623 K to 72 h allows additional microstructural evolution. Subgrain growth has produced nearly equiaxed subgrains near the center of the micrograph, while the elongated subgrain morphology characteristic of the cold-rolled microstructure is evident in other locations.

The boundary misorientations indicated on Figure 5b show that microstructural evolution during the 623 K/72 h annealing treatment does not

significantly alter the general boundary misorientation characteristics observed for the cold-rolled material. Thus, despite the nonuniform nature of the subgrain structure found for both annealing treatments at 623 K, the boundary misorientation measurements give no indication that microstructural evolution at 623 K involves discontinuous recrystallization. Microstructural evolution occurs continuously, but is more-or-less rapid depending on local variations of boundary driving pressure and Zener drag pressure.

Figure 5c shows that annealing at 648 K for 48 h allows substantially greater microstructural evolution, compared to the annealing treatments at 623 K. The 648 K/48 h treatment permits the subgrain structure present in the cold-rolled alloy to transform into a coarser subgrain structure with sharp boundaries in all regions, resulting in a more uniform microstructure than that observed for the 623 K annealing treatments. Despite the substantial subgrain growth required to transform the cold-rolled microstructure into that shown in Figure 5c, the boundary misorientations marked in Figure 5c indicate that the essential character of the cold-rolled microstructure remains. The largest transverse boundary misorientation in Figure 5c is 9° , whereas many of the boundaries oriented parallel to the rolling plane have misorientations greater than 15° .

Figures 6a-6d show 111 micro-pole figures for annealing treatments at 623, 648, and 673 K, and Figures 6e-6g are partial 111 pole figures representing the bulk textures for the same annealed samples. Discontinuous recrystallization in portions of the sample annealed at 673 K precludes measurement of a bulk pole figure that can be properly compared with the micro-pole figure which represents only orientations from recovered regions.

The bulk textures are essentially unchanged from that measured for the cold-rolled condition, indicating that microstructural evolution during the annealing treatments at 623 and 648 K does not involve substantial changes of crystallographic orientation. For the 2 annealing treatments at 623 K, the micro-pole figures are similar to the bulk pole figures, indicating that the locations in the microstructure selected for local crystal orientation analysis represent the dominant $\{112\}\langle 11\bar{1} \rangle$ texture component. In the case of the 648 K annealing treatment, a variety of orientations are present, some are near $\{112\}\langle 11\bar{1} \rangle$ but others are not. However, the micro-pole figure for the 673 K annealing treatment more closely resembles those from the 623 K treatments, suggesting that the wider variety of orientations found for the 648 K treatment is simply due to the region examined and is not a general effect associated with higher annealing temperatures. Irrespective of whether the micro-pole figures are similar to the bulk pole figures, or exhibit some differences, the grouping of subgrain orientations into layers parallel to the rolling plane is a consistent microstructural characteristic.

3.3. Microstructure and Texture After Concurrent Straining and Annealing at 673 K

Tensile specimens cut from the cold-rolled sheet were heated to 673 K using the procedure described in Section 2, and were strained at an initial rate of $6.5 \times 10^{-4} \text{ s}^{-1}$. Figure 7 shows the true stress - true strain curve obtained for a specimen tested to failure. (In Fig. 7 and throughout sections 3.3 and 4.3 of the present paper, strain values refer to deformation imposed during concurrent straining and annealing of previously cold-rolled specimens.) The total elongation did not exceed 100%, indicating that the Al-Zr-Si alloy is not superplastic for this set of processing and testing parameters. The arrows on Figure 7 indicate strain levels at which other

tensile tests were interrupted to provide samples for microstructure characterization.

Figure 8 shows optical micrographs of the gauge and grip sections of several tensile test specimens. For all strain levels, both the gauge and grip sections contain a few discontinuously recrystallized grains. These can be identified by their large size, lack of internal structure, and rounded interface morphology. The nonuniform distribution of discontinuously-recrystallized grains evidences a nonuniform distribution and low density of viable nucleation sites, and the elongated morphology of the discontinuously-recrystallized grains reflects an anisotropic growth rate [47].

In regions not swept by a discontinuous recrystallization interface, microstructure evolution occurs by continuous relaxation mechanisms ultimately producing a continuously-recrystallized microstructure. At a strain of 0.22, the salient features of the deformation microstructure are recognizable at the optical microscopy scale. For strains of 0.46 and higher, the salient characteristics of the deformation microstructure have been eradicated and evolution by continuous processes has led to formation of a grain structure. Comparison of the microstructure in the gauge section to that observed in the grip section shows that the rate of microstructure evolution is greater for concurrent straining and annealing than for annealing alone, as observed by many previous investigators [2-17].

Figure 9 shows boundary misorientation maps for specimens deformed to strains of 0.22 and 0.46, and for the undeformed grip region of the specimen deformed to a strain of 0.22. The total annealing times (including the 1200 s

temperature-stabilizing period prior to the start of straining) at 673 K for the strained specimens are 1500 s and 1900 s to attain strains of 0.22 and 0.46, respectively. Recovery of the subgrain structure in the undeformed grip section of the specimen strained to 0.22 is slight; individual dislocations have been eliminated from subgrain interiors, the boundaries appear sharp, and subgrain growth may have occurred in some regions. Only a limited number of boundary misorientation measurements were made for the grip section of the tensile specimen; these are indicated on Figure 9c. In contrast, microstructural evolution proceeds much more rapidly in the gauge sections of the tensile specimens. For a strain of 0.22, subgrain growth has occurred uniformly throughout the original deformation microstructure. However, the boundary misorientation angles are still correlated with boundary orientation: most of the boundaries parallel to the rolling plane had misorientations exceeding 10° while the majority of transverse boundaries had misorientations below 10° .

Figure 9b suggests that further straining causes additional evolution of the subgrain size and boundary misorientations. The majority of boundaries now have misorientations exceeding 10° , independent of boundary orientation. At this point, the microstructure is properly termed "recrystallized" since most boundaries are of high-angle character. Transformation of the subgrain boundary network to a grain boundary network in the strain interval from 0.22 to 0.46 is not accompanied by a marked increase in grain size.

Figs. 10a-c are 111 micro-pole figures corresponding to the two strain levels represented in Figure 9 and to the grip region of the tensile sample strained to 0.22. X-ray pole figures could not be prepared for the deformed

specimens because of the limited size of the uniformly-strained portions of the tensile specimens. Interactive comparison of subgrain orientation and subgrain location reveals that the characteristic layered structure of the cold-rolled and cold-rolled plus annealed materials breaks down during concurrent straining and annealing. (This may not be strongly apparent from the micro-pole figures alone, because the correlation of subgrain location with orientation is lost.) Thus, while annealing preserves the fundamental layered character of the cold-rolled state, concurrent straining and annealing develops diverse grain orientations from the clustered subgrain orientations present in the original layered microstructure.

4. DISCUSSION

The mechanisms that contribute to recovery and to continuous recrystallization reflect the local microstructural environment. Consequently, gaining an understanding of these mechanisms requires observations of a local nature, such as micro-pole figures and boundary misorientation maps. Such microstructural observations provide very detailed information about small volumes of material, but these small volumes may not always represent the "average" behavior of the material. This is particularly true for deformation and annealing microstructures which are, by nature, inhomogeneous. We have attempted to correlate the local observations with bulk observations where possible, but we also acknowledge that many of our conclusions are based on observations of limited volumes of material and may have been influenced by the inhomogeneous nature of the microstructure.

4.1 Microstructure and Texture after Rolling

The results of the present investigation are in accord with prior observations of the microstructure and the bulk texture of cold-rolled aluminum (c.f. [32-34,48-53]). In addition, several prior investigations of microtexture and subgrain orientations in heavily cold-rolled aluminum alloys have been reported [8,14,33,34,51,53,]. In general, investigators who prepared TEM foils parallel to the rolling plane reported finding predominately low-angle boundaries [8,14] while those who have prepared foils normal to the rolling plane have reported finding a mixture of low-angle and high-angle boundaries [33,34,51,53]. The reason for this difference is clearly the orientation of the high-angle boundaries. Since shear bands were not observed in TEM samples in the present investigation, the high-angle boundaries in the deformation microstructure are either prior grain boundaries or are associated with a transition band [54-57].

Ørsund et al. [34] investigated cold-worked commercially-pure aluminum and found that the spacing of high-angle boundaries along the S direction was on the order of 1 to 2 μm within a transition band, but the spacing of transition bands or grain boundaries was not reported. For the Al-Zr-Si alloy used in the present investigation, high-angle boundary spacings were found to range from 2 μm to more than 10 μm . Since the spacing of high-angle boundaries along the S direction depends on the spacing of grain boundaries prior to the start of cold work and on the type and density of transition bands introduced during cold working, the observed spacing is likely to be a function of initial grain size, alloy composition and cold-working conditions. Thus, it is not surprising that different investigators have found significant differences in the high-angle boundary spacing in the S direction.

4.2 Microstructure Evolution During Annealing

The present observations of continuous evolution of microstructure during annealing are in broad agreement with previously-reported observations as described in recent reviews [58,59]. Recovery processes allow removal of statistically-stored dislocations and subgrain growth. Subgrain growth may involve subgrain boundary migration or subgrain coalescence [57,60-62], neither of which is expected to significantly influence the bulk texture. However, the boundary misorientation maps reveal that high-angle boundaries are relatively immobile during the annealing treatments which permit substantial subgrain growth. This can be inferred by observing that the high-angle boundaries remain approximately parallel to the rolling plane during annealing, and that the subgrain sizes on opposite sides of the high-angle boundaries are similar. The high-angle boundary spacing results are consistent with this view, but they cannot be used to reach this conclusion independently because of their large variability.

The observations described above conflict with prior observations which show that the mobility of high-angle boundaries is greater than the mobility of low-angle boundaries [58]. There are several possible explanations for the apparent immobility of high-angle boundaries in the present case, including:

- i. The Zener drag from Al_3Zr particles is greater for high-angle boundaries than for low-angle boundaries [47,63].
- ii. If the activation enthalpy for high-angle boundary migration is larger than for low-angle boundary migration [23], the relative boundary mobilities may reverse at some temperature.
- iii. The driving pressure for high-angle boundary migration is less than for low-angle boundary migration, possibly due to geometrical effects.

iv. Both types of boundaries are immobile and subgrain growth is entirely due to subgrain coalescence.

Results from the present investigation cannot identify which of these potential mechanisms is operative, but the consequence of high-angle boundary immobility during the annealing treatments is that high-angle boundaries introduced during deformation remain in the microstructure during annealing. Thus, the layered character of the deformation microstructure in the cold-rolled alloy persists for all of the annealing treatments investigated in the present study. Consequently, from geometrical considerations alone, high-angle boundaries comprise an increasing proportion of the total boundary area as recovery proceeds.

One of the salient characteristics of continuous recrystallization described by many previous investigators is an increase in the proportion of high-angle boundaries during concurrent straining and annealing [1-17]. One possible explanation for this observation is simply the gradual disappearance of low-angle boundaries through subgrain growth mechanisms, while the high-angle boundaries are retained. If this were the only mechanism responsible for increasing the proportion of high-angle boundaries during continuous recrystallization, accelerated subgrain growth by concurrent straining would be sufficient to fully explain continuous recrystallization. In the next section, it is shown that this mechanism cannot account for all of the characteristics of continuous recrystallization.

4.3 Microstructure Evolution During Concurrent Straining and Annealing

Comparison of the microstructures from the undeformed grip and from the deformed gauge sections of the tensile specimen strained to 0.22 shows that

concurrent straining substantially accelerates subgrain growth, in accord with previously-reported results [2-17]. Figures 9a and 9b illustrate the evolution of boundary character with concurrent straining and annealing. For the specimen deformed to a strain of 0.22, the boundary misorientations resemble those found in annealed samples. Most of the boundaries parallel to the rolling plane are of high-angle character whereas most of the transverse boundaries are low-angle boundaries. However, the low-angle boundaries in Figure 9a have a higher average misorientation than those found in microstructures which have been annealed to produce a similar subgrain size; i.e., Fig. 5c. Figure 9b shows that increasing the concurrent strain at the annealing temperature causes a further increase in the average misorientation of transverse boundaries, as well as an additional increase in subgrain size.

The microstructure at the start of concurrent straining and annealing is a layered structure with the layers lying parallel to the rolling plane. Within each layer the subgrains are similarly-oriented, as shown by the clustering of poles on the micro-pole figures and the low boundary misorientation angles. Concurrent straining and annealing increases the boundary misorientations gradually, suggesting that the orientations of the subgrains within each layer must be diverging. The micro-pole figures are consistent with this view; the tightly-clustered poles found for the annealed samples have been replaced by much more loosely-defined groups.

A salient aspect of the present experimental observations is the divergence of subgrain orientations within each of the original layers during concurrent straining and annealing, which does not occur during annealing. Previous investigators have attributed this to accumulation of misorientation

by low-angle boundary migration [7,8], or alternatively to subgrain rotation resulting from grain boundary sliding [11,15]. The present observations provide strong evidence for the subgrain rotation mechanism. Comparison of Figs. 9a and 5c shows that the average misorientation angle of transverse boundaries in the concurrently strained and annealed sample is appreciably higher than in the annealed sample, for equivalent subgrain size. If the increase in boundary misorientation resulted from accumulation of misorientation during boundary migration, the observed misorientations should be similar in samples of similar subgrain size. This is clearly not the case. A second observation supporting the subgrain rotation mechanism is the divergence of orientations shown in the micro-pole figures. Subgrain growth would cause the number of poles in each cluster to diminish as subgrains are eliminated, but the remaining poles would be closely grouped.

Rotation of subgrains during concurrent straining and annealing has been previously proposed by McNelley et al. to account for observations of continuous recrystallization in Al-Mg alloys [11,15]. They further proposed that boundary sliding along subgrain boundaries is the mechanism of subgrain rotation. However, McNelley's observations of TEM foils prepared parallel to the rolling plane revealed subgrains bounded on all sides by low-angle boundaries at the start of concurrent straining and annealing. Sliding of low-angle boundaries is contrary to observations of boundary sliding in bicrystals which show that sliding occurs at very low rates for boundary misorientations below 10° [23-27]. To avoid this dilemma, McNelley et al. suggested that boundaries with initially moderate misorientations in the range 5° to 7° could slide sufficiently to allow gradual evolution toward higher misorientation angles.

The present results permit more graceful interpretation of subgrain rotation during concurrent straining and annealing. At the start of concurrent straining and annealing, a significant fraction of the boundary area consists of high-angle boundaries. Sliding along these preexisting high-angle boundaries is entirely consistent with the bicrystal sliding observations, and can lead to an increase in the misorientation of the remaining low-angle boundaries through subgrain rotation. In this view, the preexisting high-angle boundaries play a key role in microstructural evolution during concurrent straining and annealing. At the start of straining, they are the only boundaries capable of sliding. Sliding along the preexisting high-angle boundaries causes rotation of the adjoining subgrains, thereby introducing additional high-angle boundaries which are also able to slide. Repetition of this process rapidly transforms low-angle boundaries into high-angle boundaries throughout the microstructure. Subgrain growth takes place simultaneously but plays no direct role in the transformation of low-angle boundaries into high-angle boundaries.

In the introduction, two incompletely understood aspects of continuous recrystallization were identified. The present investigation has clarified both issues. The mechanism that promotes development of high-angle boundaries by continuous processes is subgrain rotation. The mechanism of subgrain rotation is probably sliding of preexisting high-angle boundaries during concurrent straining and annealing. The only known driving force for boundary sliding is a stress differential across the boundary. Since significant stress differentials do not exist during static annealing, transverse subgrain boundary misorientations cannot increase into the high-angle range without imposition of a stress during annealing. Thus, we conclude that straining

concurrently with annealing is required to obtain continuous recrystallization.

5. CONCLUSIONS

Based on observations described in the present paper, the following conclusions may be formulated.

1. Cold rolling of the Al-Zr-Si alloy to an effective strain of 2.6 produces a microstructure that consists of layers parallel to the rolling plane; only low-angle boundaries are present within each layer and adjacent layers are separated by high-angle boundaries. The layer thickness ranges from 2 to more than 10 μm . Subgrain boundaries divide each layer into subgrains which have similar lattice orientations.
2. Annealing of the cold-rolled alloy at 623, 648 and 673 K causes subgrain growth but the high-angle boundaries initially present in the cold-rolled alloy are relatively immobile during these annealing treatments. Within each layer, the subgrain boundary misorientation does not increase significantly during annealing.
3. Concurrent straining and annealing of the rolled alloy at 673 K causes a rapid increase in subgrain size and a divergence of subgrain orientations within the layered microstructure. The divergence of subgrain orientations is accompanied by an increase in subgrain boundary misorientation. The divergence of subgrain orientations is a manifestation of subgrain rotation during concurrent straining and annealing. After a strain of 0.46, most of

the transverse boundaries are of high-angle character, indicating that the subgrain structure continuously transformed into a grain structure.

4. Accumulation of misorientation during subgrain boundary migration has been previously proposed as a mechanism for the increase in subgrain boundary misorientation during concurrent straining and annealing. The present results are inconsistent with this mechanism.

5. Boundary sliding has been previously proposed as the mechanism of subgrain rotation during concurrent straining and annealing, but previous investigators encountered difficulty reconciling this mechanism with independent observations indicating low sliding rates for low-angle boundaries. In the present investigation, TEM foils normal to the T direction revealed a significant fraction of high-angle boundaries in the microstructure at the start of continuous recrystallization. Sliding along preexisting high-angle boundaries leading to an increase in subgrain boundary misorientation through subgrain rotation is consistent with the present results and with those of prior investigators.

6. ACKNOWLEDGEMENTS

We are grateful to Reynolds Metals Co. for providing the Al-Zr-Si alloy used in this investigation and to Dr. W.O. Powers and Mr. M. Kumar for invaluable experimental assistance. This research was sponsored by the Air Force Office of Scientific Research under contract number AFOSR-87-0082-A; the contract monitor was Dr. A. Rosenstein.

7. REFERENCES

1. H. Alborn, E. Hornbogen and U. Koster, J. Mat. Sci., 4 (1969) 944.
2. R.A. Benedek and R.D. Doherty, Scripta Met., 8 (1974) 675.
3. B.M. Watts, M.J. Stowell, B.L. Bakie and D.G.E. Owen, Metals Science, 10 (1976) 189; 10 (1976) 198.
4. R.H. Brinknell and J.W. Edington, Met. Trans. A, 10A (1979) 1257.
5. R.H. Brinknell and J.W. Edington, Acta Met., 27 (1979) 1303.
6. E. Nes, J. Materials Science Letters, 13 (1978) 2052.
7. E. Nes, Metal Science, 13 (1979) 211.
8. E. Nes, in "Superplasticite/Superplasticity", B. Baudalet and M. Suery (eds.), Editions du CNRS, Paris, 1985, pp. 7.1-7.11.
9. T.R. McNelley, E.-W. Lee and M.E. Mills, Met. Trans. A, 17A (1986) 1035.
10. E.-W. Lee, T.R. McNelley, A.F. Stengel, Met. Trans. A, 17A (1986) 1043.
11. T.R. McNelley, E.-W. Lee and A. Garg, in "Aluminum Alloys - Physical and Mechanical Properties", E.A. Starke and T.H. Sanders (eds.), Engineering Materials Advisory Services Ltd., West Midlands, 1986, pp. 1269-1283.
12. E.-W. Lee and T.R. McNelley, Materials Science and Eng., 93 (1987) 45.
13. E.-W. Lee and T.R. McNelley, Materials Science and Eng., 96 (1987) 253.
14. S.J. Hales and T.R. McNelley, Acta Met., 36 (1988) 1229.
15. S.J. Hales and T.R. McNelley, in "Superplasticity in Aerospace", H.C. Heikkinen and T.R. McNelley (eds.), The Metallurgical Society, Warrendale, 1988, pp. 61-76.
16. R. Crooks, in "Superplasticity in Aerospace", H.C. Heikkinen and T.R. McNelley (eds.), The Metallurgical Society, Warrendale, 1988, pp. 51-60.
17. T.J. Watson and J.I. Bennetch, in "Superplasticity in Aerospace", H.C. Heikkinen and T.R. McNelley (eds.), The Metallurgical Society, Warrendale, 1988, pp. 261-295.
18. R. Grimes, M.J. Stowell and B.M. Watts, Metals Technology, 3 (1976) 154.
19. D.J. Lloyd and D.M. Moore, in "Superplastic Forming of Structural Alloys", N.E. Paton and C.H. Hamilton (eds.), The Metallurgical Society, Warrendale, 1982, pp. 147-172.
20. J. Wadsworth, in "Superplastic Forming", AMS, Metals Park, 1985, pp. 43-57.

21. W.S. Miller and J. White, in "Superplasticity in Aerospace", H.C. Heikkinen and T.R. McNelley (eds.), The Metallurgical Society, Warrendale, 1988, pp. 211-228.
22. I. Nordlander and A. Tholen, Journal of Microscopy, 90 (1973) 221.
23. S.K. Tung and R. Maddin, Trans AIME, 209 (1957) 905.
24. F. Weinberg, Trans AIME, 212 (1958) 808.
25. M. Biscondi and C. Goux, Mem. Sci. Revue de Metallurgie, 65 (1968) 167.
26. P. Lagarde and M. Biscondi, Canadian Metallurgical Quart., 13 (1974) 245.
27. T. Watanabe, N. Kuriyama and S. Karashima, in "Proc. Fourth Inter. Conf. Strength of Metals and Alloys", Nancy, France, 1976, vol. 1, pp. 383-387.
28. A.S. Malin and M. Hatherly, Metal Sci., 13 (1979) 463.
29. A.S. Malin, J. Huber and M. Hatherly, Z. Metallk., 72 (1980) 310.
30. A.A. Ridha and W.B. Hutchinson, Acta Met., 30 (1982) 1929.
31. M. Hatherly, in "Sixth International Conf. Strength of Metals and Alloys", R.C. Gifkins (ed.), Pergamon Press, Oxford, 1983, pp. 1181-1195.
32. E. Nes, W.B. Hutchinson and A.A. Ridha, in "Seventh International Conf. Strength of Metals and Alloys", H.J. McQueen, J.-P. Bilon, J.I. Dickson, J.J. Jonas and M.G. Akben (eds.), Pergamon Press, Oxford, 1986, pp. 57-62.
33. A.L. Dons and E. Nes, Materials Science and Tech., 2 (1986) 8.
34. R. Ørsund, J. Hjelen and E. Nes, Scripta Met., 23 (1989) 1193.
35. O. Reiso, H. Westengen and L. Auran, in "Seventh international Light Metals Congress", Aluminium-Verlag GmbH, Duesseldorf, 1981, pp. 186-188.
36. H. Westengen, O. Reiso and L. Auran, Aluminium, 56 (1980) 768.
37. H. Westengen, L., Auran and O. Reiso, Aluminium, 57 (1981) 797.
38. C.T. Young, J.H. Steele and J.L. Lytton, Met. Trans. A, 4 (1973) 2081.
39. R.A. Schwarzer and H. Weiland, Textures and Microstructures, 8 (1988) 551.
40. F.F. Lange, Acta Met., 15 (1967) 311.
41. H.K.D.H. Bhadeshia, "Worked Examples in the Geometry of Crystals", Chameleon Press Ltd., London, 1987, pp. 18-21.
42. V. Randle and B. Ralph, J. Materials Science, 21 (1986) 3823.
43. L.G. Schultz, J. Applied Physics, 20 (1949) 1030.

44. I.L. Dillamore and W.T. Roberts, Metallurgical Reviews, 10 (1965) 271.
45. B. Gale and D. Griffiths, British J. Applied Physics, 11 (1960) 96.
46. H.J. McQueen and J.E. Hockett, Met. Trans., 1 (1970) 2997.
47. E. Nes, N. Ryum and O. Hunderi, Acta Met., 33 (1985) 11.
48. K.R. Brown, in "Textures in Non-Ferrous Metals and Alloys", H.D. Merchant and J.G. Morris (eds), The Metallurgical Society, Warrendale, 1985, pp. 131-143.
49. B. Bay and N. Hansen, Met. Trans., 10A (1979) 279.
50. C.Y.J. Barlow, B. Bay and N. Hansen, Phil Mag. A, 51 (1985) 253.
51. B. Bay, N. Hansen and D. Kuhlmann-Wilsdorf, Materials Sci and Eng., A113 (1989) 385.
52. J. Hirsch, E. Nes and K. Lucke, Acta Met., 35 (1987) 427.
53. J. Hjelen, E. Nes and R. Hoier, in "Aluminum Alloys - Physical and Mechanical Properties", E.A. Starke and T.H. Sanders (eds.), Engineering Materials Advisory Services Ltd., West Midlands, 1986, pp. 471-483.
54. I.L. Dillamore, P.L. Morris, C.J.E. Smith and W.B. Hutchinson, Proc. Roy. Soc. London A, 329 (1972) 405.
55. S.P. Bellier and R.D. Doherty, Acta Met., 25 (1977) 521.
56. A. Kreisler and R.D. Doherty, Metal Science, 12 (1978) 551.
57. P. Faivre and R.D. Doherty, J. Materials Science, 14 (1979) 897.
58. H. Hu, in "Metallurgical Treatises", J.K. Tien and J.F. Elliott (eds), The Metallurgical Society, Warrendale, 1981, pp. 385-407.
59. A.R. Jones, in "Grain Boundary Structure and Kinetics", American Society for Metals, Metals Park, 1980, pp. 379-425.
60. H. Hu, in "Recovery and Recrystallization of Metals", L. Himmel (ed), Gordon and Breach, New York, 1963, pp. 311-362.
61. H. Fujita, J. Phys. Soc. Japan, 16 (1961) 397.
62. J.C.M. Li, J. Appl. Phys., 33 (1962) 2958.
63. C.J. Tweed, B. Ralph and N. Hansen, Acta Met., 32 (1984) 1407.

Fig. 1 Optical micrograph of Al-Zr-Si alloy cold rolled to an effective strain of 2.6. (Barkers etch)

Fig. 2 TEM micrographs of Al-Zr-Si alloy cold-rolled to $\epsilon_{\text{eff}} = 2.6$. a) Inhomogeneous character of the cold-worked microstructure. b) Detail of subgrains.

Fig. 3 Grain boundary misorientation map for Al-Zr-Si alloy cold-rolled to $\epsilon_{\text{eff}} = 2.6$.

Fig. 4 111 pole figures for Al-Zr-Si alloy cold-rolled to $\epsilon_{\text{eff}} = 2.6$. a) Partial bulk pole figure. b) Micro-pole figure from Fig. 3. c) Micro-pole figure from a different region of the cold-rolled alloy.

Fig. 5 Grain boundary misorientation map for Al-Zr-Si alloy cold-rolled to $\epsilon_{\text{eff}} = 2.6$ and annealed: a) 623 K for 8 h. b) 623 K for 72 h. c) 648 K for 48 h. (Barkers etch)

Fig. 6 111 pole figures for Al-Zr-Si alloy cold-rolled to $\epsilon_{\text{eff}} = 2.6$. a,e) Micro-pole figure and partial bulk pole figure for 623 K/8 h annealing treatment. b,f) Micro-pole figure and partial bulk pole figure for 623 K/72 h annealing treatment. c,g) Micro-pole figure and partial bulk pole figure for 648 K/48 h annealing treatment. d) Micro-pole figure for 673 K/8 h annealing treatment.

Fig. 7 Stress-strain curve for deformation of the cold-rolled Al-Zr-Si alloy at 673 K with an initial strain rate of $6.5 \times 10^{-4} \text{ s}^{-1}$.

Fig. 8 Optical micrographs of sections normal to the T direction of tensile specimens deformed at 673 K and $6.5 \times 10^{-4} \text{ s}^{-1}$. a) Strain = 0.22. b) Strain = 0.46. c) Unstrained grip section of specimen strained to 0.22. (Barkers etch)

Fig. 9 Grain boundary misorientation maps for Al-Zr-Si tensile specimens deformed at 673 K and $6.5 \times 10^{-4} \text{ s}^{-1}$. a) Strain = 0.22. b) Strain = 0.46. c) Unstrained grip section of specimen strained to 0.22.

Fig. 10 111 micro-pole figures for Al-Zr-Si tensile specimens deformed at 673 K and $6.5 \times 10^{-4} \text{ s}^{-1}$. a) Strain = 0.22. b) Strain = 0.46. c) Unstrained grip section of specimen strained to 0.22.

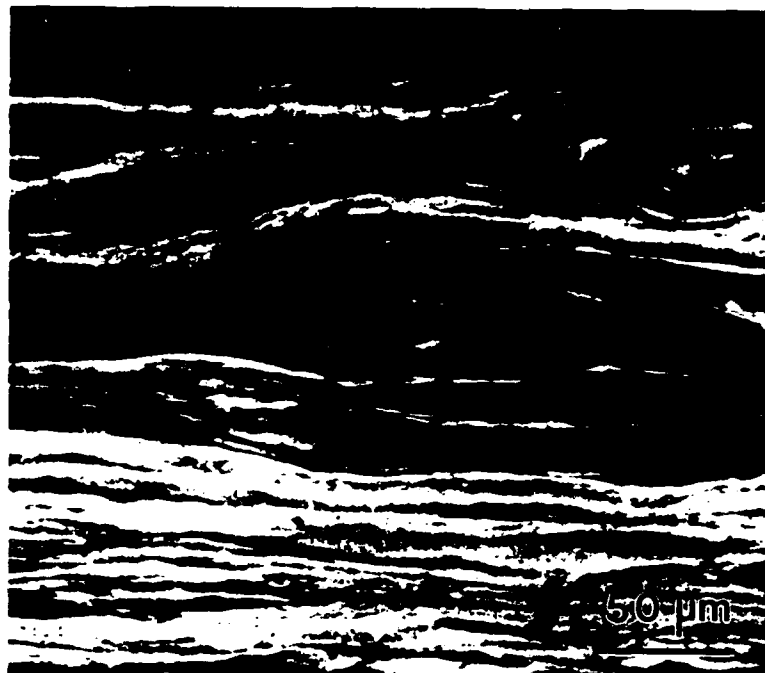


Fig. 1 Optical micrograph of Al-Zr-Si alloy cold rolled to an effective strain of 2.6. (Barkers etch)

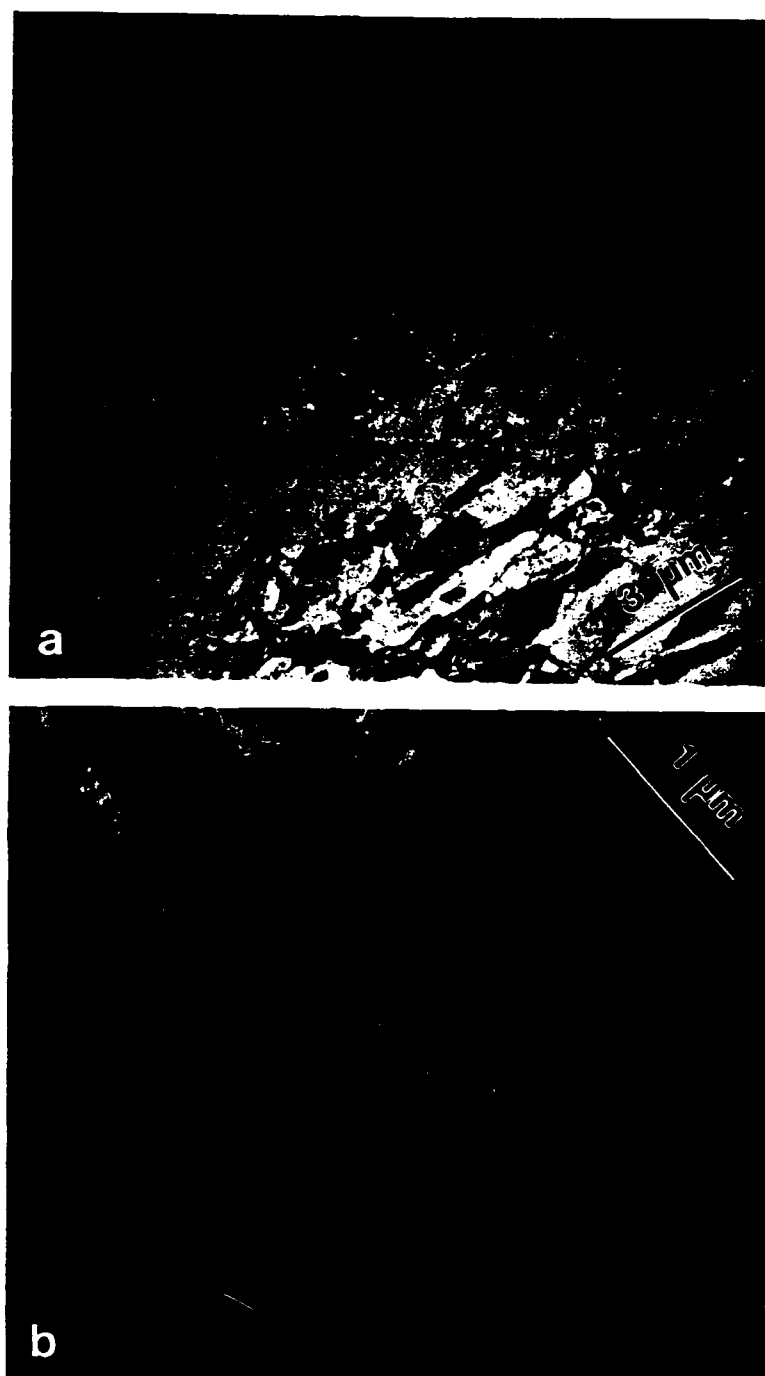


Fig. 2 TEM micrographs of Al-Zr-Si alloy cold-rolled to $\epsilon_{\text{eff}} = 2.6$.
a) Inhomogeneous character of the cold-worked microstructure. b) Detail of subgrains.

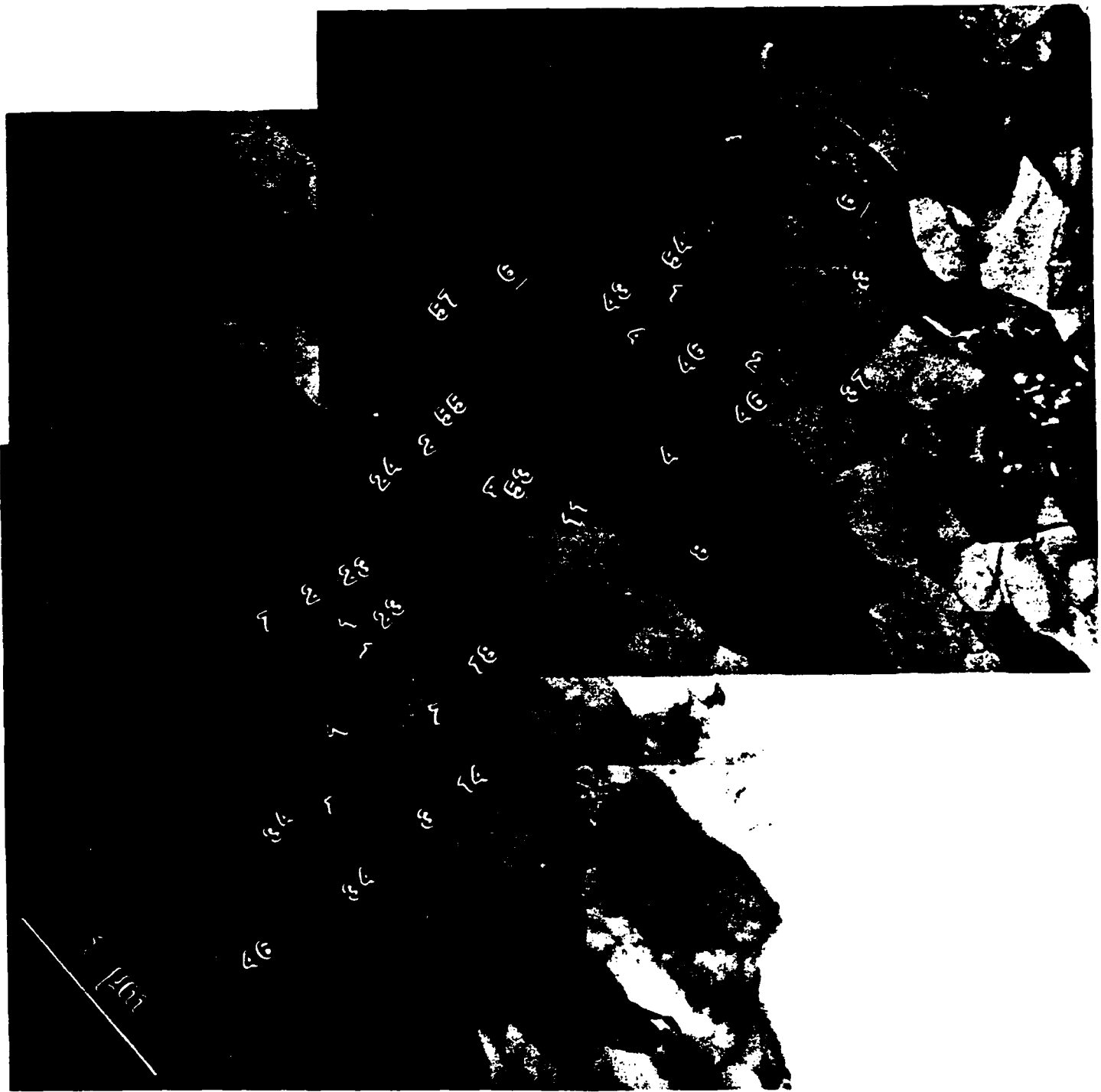


Fig. 3 Grain boundary misorientation map for Al-Zr-Si alloy cold-rolled to $\epsilon_{\text{eff}} = 2.6$.

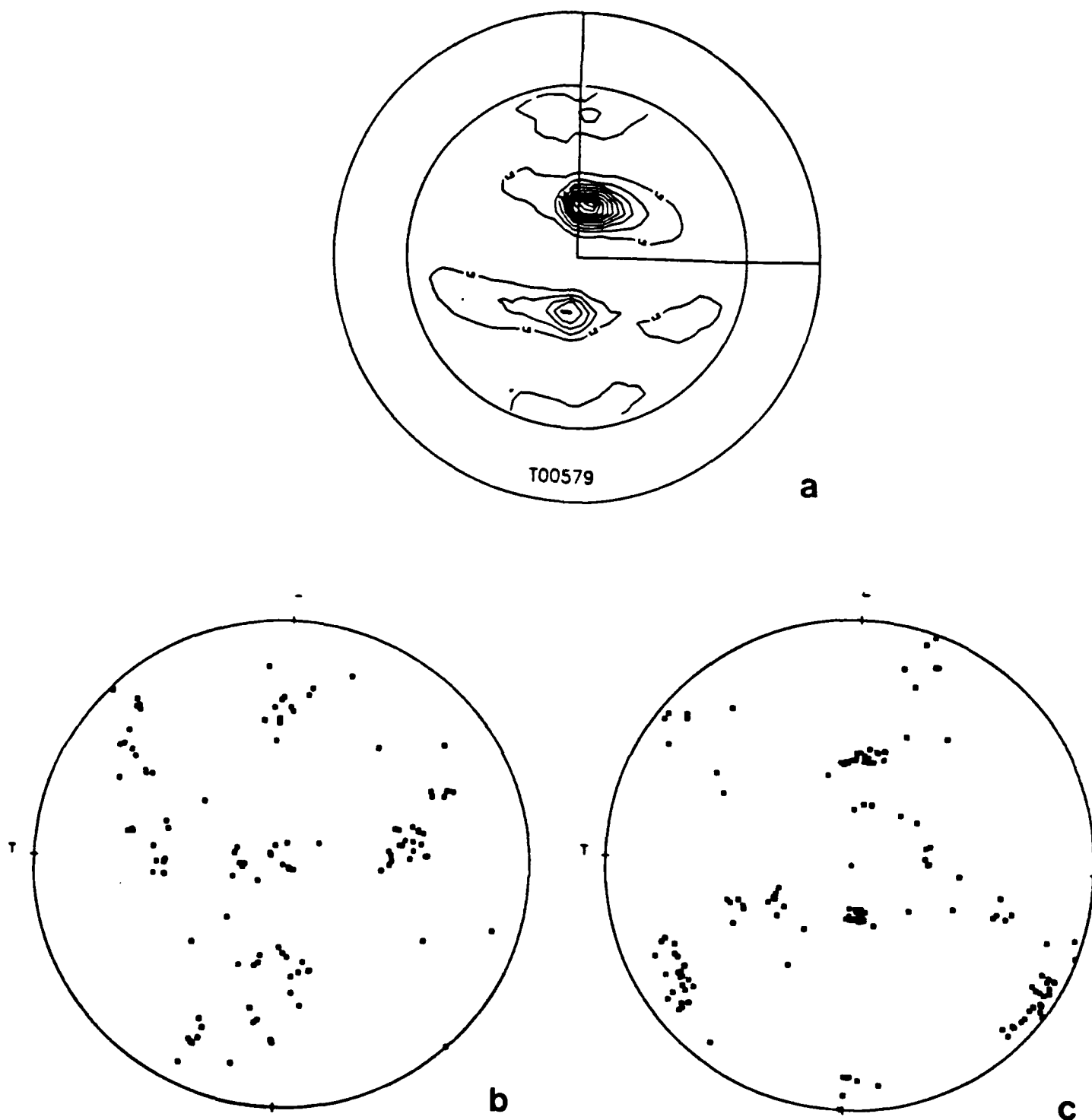


Fig. 4 111 pole figures for Al-Zr-Si alloy cold-rolled to $\epsilon_{eff} = 2.6$.
a) Partial bulk pole figure. b) Micro-pole figure from Fig. 3. c) Micro-pole figure from a different region of the cold-rolled alloy.



a

Fig. 5 Grain boundary misorientation map for Al-Zr-Si alloy cold-rolled to $\epsilon_{eff} = 2.6$ and annealed: a) 623 K for 8 h. b) 623 K for 72 h. c) 648 K for 48 h. (Barkers etch)



b



c

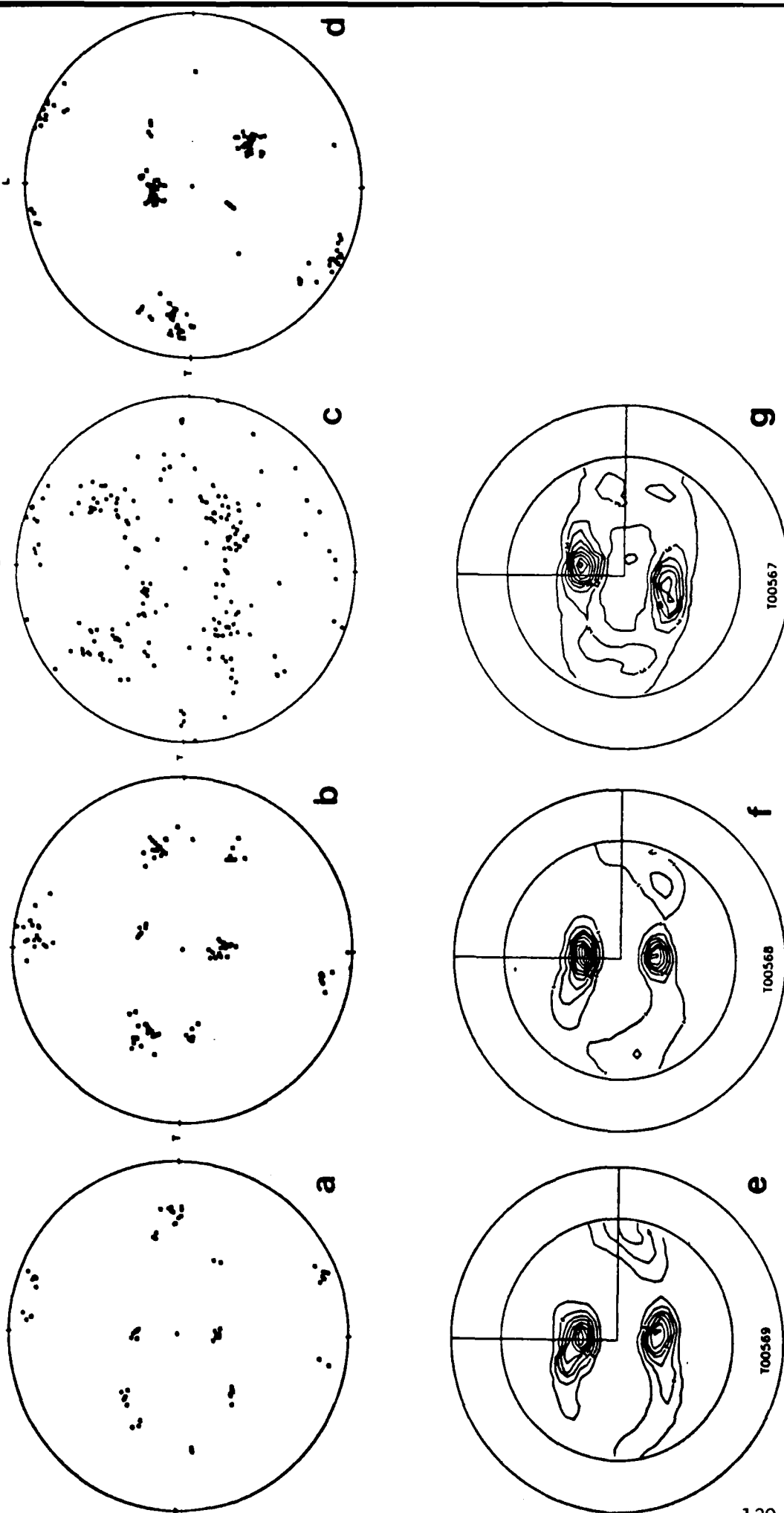


Fig. 6 111 pole figures for Al-Zr-Si alloy cold-rolled to $\epsilon_{eff} = 2.6$. a,e) Micro-pole figure and partial bulk pole figure for 623 K/8 h annealing treatment. b,f) Micro-pole figure and partial bulk pole figure for 623 K/72 h annealing treatment. c,g) Micro-pole figure and partial bulk pole figure for 648 K/48 h annealing treatment. d) Micro-pole figure for 673 K/8 h annealing treatment.

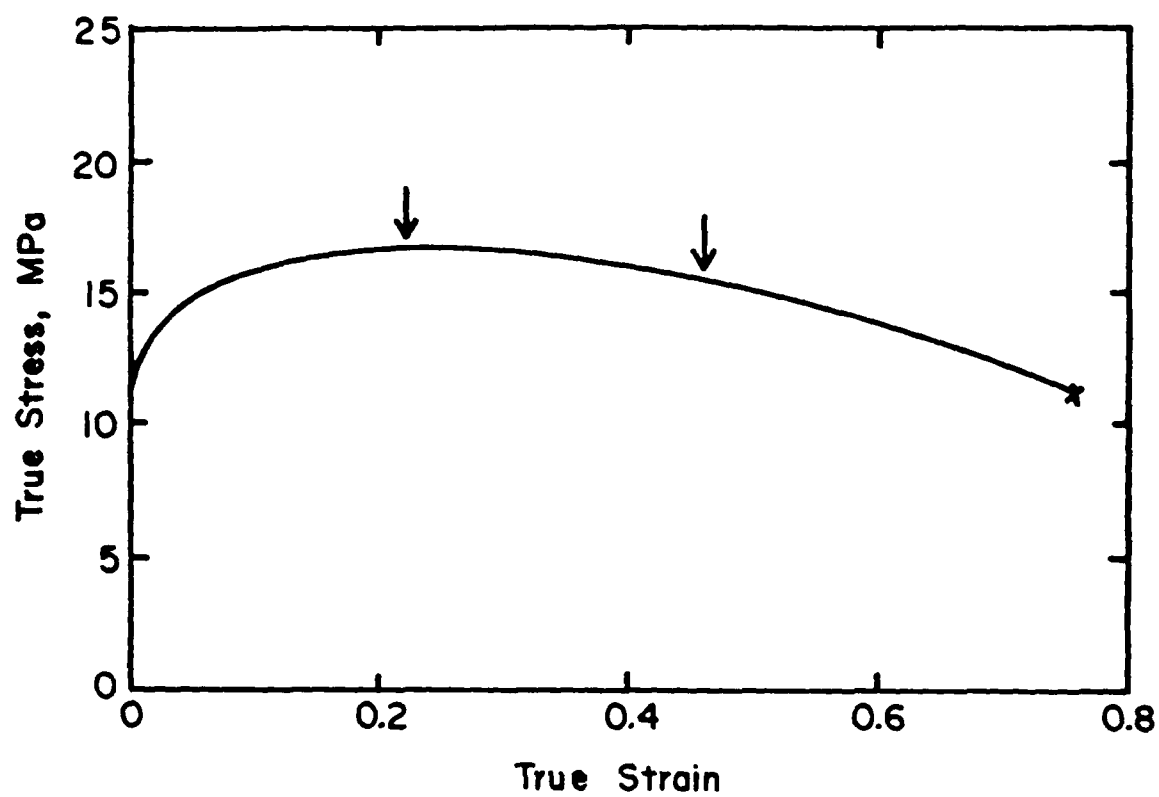
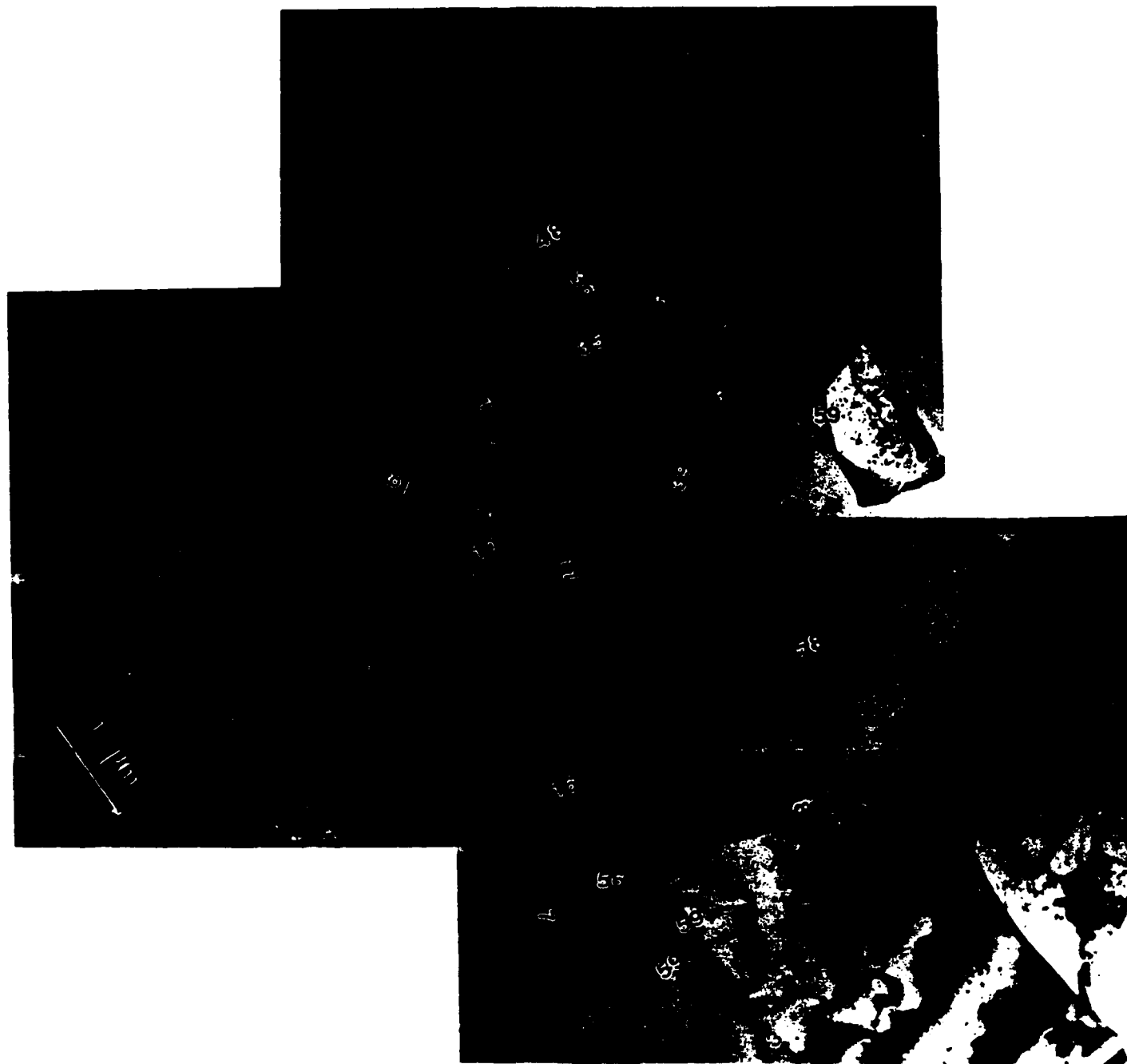


Fig. 7 Stress-strain curve for deformation of the cold-rolled Al-Zr-Si alloy at 673 K with an initial strain rate of $6.5 \times 10^{-4} \text{ s}^{-1}$.



Fig. 8 Optical micrographs of sections normal to the T direction of tensile specimens deformed at 673 K and $6.5 \times 10^{-4} \text{ s}^{-1}$. a) Strain = 0.22. b) Strain = 0.46. c) Unstrained grip section of specimen strained to 0.22. (Barkers etch)



a

Fig. 9 Grain boundary misorientation maps for Al-Zr-Si tensile specimens deformed at 673 K and $6.5 \times 10^{-4} \text{ s}^{-1}$. a) Strain = 0.22. b) Strain = 0.46. c) Unstrained grip section of specimen strained to 0.22.



b



c

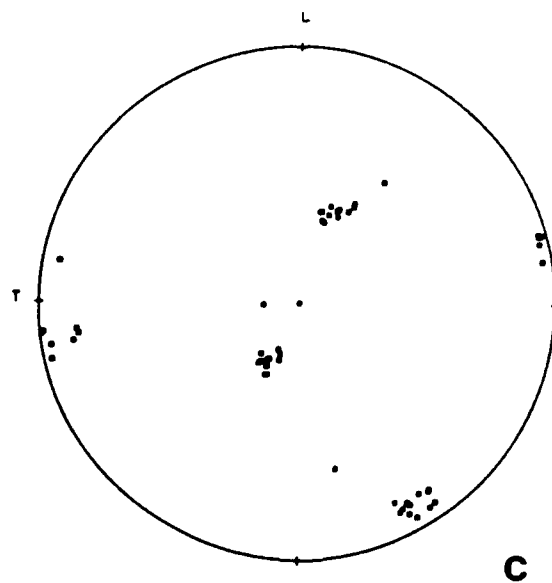
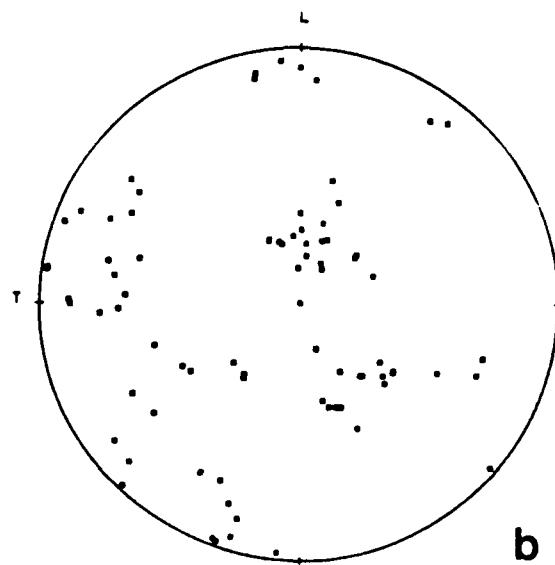
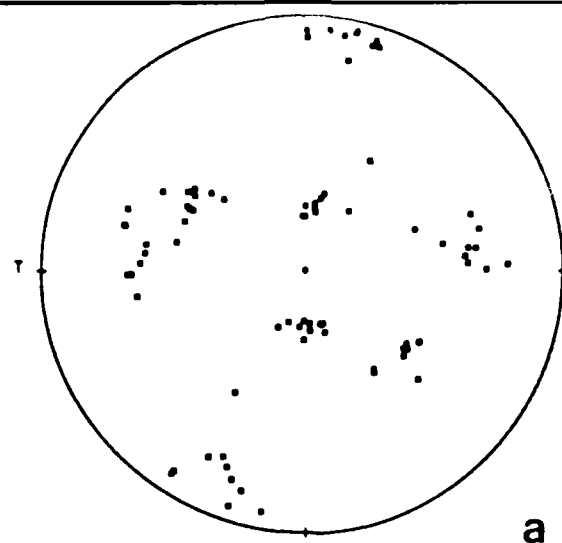


Fig. 10 111 micro-pole figures for Al-Zr-Si tensile specimens deformed at 673 K and $6.5 \times 10^{-4} \text{ s}^{-1}$. a) Strain = 0.22. b) Strain = 0.46. c) Unstrained grip section of specimen strained to 0.22.

DISTRIBUTION LIST

Copy No.

1 - 6	Air Force Office of Scientific Research/NE Building 410 Bolling Air Force Base Washington, DC 20332-6448 Attention: Dr. Alan H. Rosenstein
7 - 8	E. A. Starke, MS
9	J. A. Wert, MS
10	T. H. Courtney, MS
11 - 12	E. H. Pancake, Clark Hall
13	Pre-award Administration Files

JO#3039.jae